

論文 / 著書情報
Article / Book Information

題目(和文)	半導体量子ドットのエネルギー準位と多粒子間相関
Title(English)	Energy levels and many-particle correlations in semiconductor quantum dots
著者(和文)	山際正和
Author(English)	Masakazu Yamagiwa
出典(和文)	学位:博士(理学), 学位授与機関:東京工業大学, 報告番号:甲第5967号, 授与年月日:2005年3月26日, 学位の種別:課程博士, 審査員:
Citation(English)	Degree:Doctor of Science, Conferring organization: Tokyo Institute of Technology, Report number:甲第5967号, Conferred date:2005/3/26, Degree Type:Course doctor, Examiner:
学位種別(和文)	博士論文
Type(English)	Doctoral Thesis

Energy Levels and Many-Particle Correlations in Semiconductor Quantum Dots

Masakazu Yamagiwa

Department of Physics
Tokyo Institute of Technology
Tokyo, Japan

February 19, 2005

Abstract

The subject of this thesis is the study of the energy levels and many-particle correlations in semiconductor quantum dots (QDs). This subject is pursued from both the QD growth perspective, as well as the optical scattering and excitation experimental perspective.

In this study, GaAs/AlGaAs QDs are prepared by modified droplet epitaxy. QDs made by this method have no strain and wetting layer, whereas these characteristics are mostly unavoidable when making QDs by the conventional Stranski-Krastanov growth mode. GaAs/AlGaAs QD samples with ultra-low density are prepared to make possible for the first time single QD spectroscopy of GaAs/AlGaAs QDs made by modified droplet epitaxy. Two such low density samples with different barrier bandgaps are prepared. Of these two samples, one is found to have high structural asymmetry.

Resonant Raman spectroscopy is employed as a good method for studying exciton-phonon interactions in QDs. InGaAs/GaAs QDs made by heterogeneous droplet epitaxy are used, as this is a QD system with a barrier that is transparent to the QD photoluminescence line. Also, QDs made by heterogeneous droplet epitaxy have no wetting layer, and the QD/barrier interface is well defined. Thus, InGaAs/GaAs QDs made by heterogeneous droplet epitaxy are a practical choice for this investigation. The InGaAs/GaAs QD samples are annealed at different temperatures, and the effects of QD/barrier interface modification on the exciton-phonon coupling in QDs is observed by resonant Raman spectroscopy.

The QD photoluminescence (PL) pressure dependence is a powerful method for studying the band crossover, and thus the band-edge discontinuity, of the GaAs/AlGaAs QD heterojunction. This method utilizes the fact that the semiconductor bandgap changes due to a reduction in the lattice constant caused by pressure application. By measuring the pressure induced bandgap shift by PL, it is possible to reconstruct the heterojunction band structure. From these measurements, the relative band lineups at the heterojunction at ambient pressure are reconstructed. These results are used in effective mass calculations, in which the annealing-induced QD-barrier interface interdiffu-

sion is taken into consideration.

The low density GaAs/AlGaAs QD sample is used to study the energy levels and the multi-carrier correlations in a single dot. Initially, the feasibility of single QD micro-PL spectroscopy (a diffraction-limited microscopy-PL spectroscopy method) via a mask is evaluated by using a portable mask as a non diffraction-limited light source. The mask is made using standard micro-machining methods. Next, a mask is fabricated directly on the low density sample in order to achieve closer proximity between the nanohole and the sample surface, in the hopes of achieving better signal-to-noise ratio. The mask is made using the lift-off method. From masked-sample micro-PL spectroscopy, an idea of single QD PL spectra is obtained. Finally, micro-PL spectroscopy is used to obtain single QD spectra from low density QD samples with no mask, which have the same spectral characteristics of single QD spectroscopy via a mask and are expected to originate from a single QD. From the single GaAs/AlGaAs QD PL spectra of various single QDs, the discrete energy levels of QDs are determined, and are compared to the effective mass calculations. From the renormalized ground state emission, electron-electron, hole-hole, and electron-hole exchange interaction energies are also determined from a recombination model based on the combinations of various non-recombining “spectator” carriers with various spins. The electron-electron, hole-hole, and electron-hole exchange interaction energies’ relation to QD size is determined.

GaAs/AlGaAs QDs with highly anisotropic shapes are studied using micro-PL. Here, the shape of the QD under investigation departs from a pyramidal shape to that of a quantum wire (QWR)-like shape. The difference in shape gives a different confinement potential and different carrier correlation effects from those of the pyramidal QD. The shift of very sharp luminescence lines in GaAs/AlGaAs QWR-like QDs at increasing excitation density is seen. These sharp lines correspond to the recombination of one dimensional excitons localized in a highly anisotropic-shaped QD. The evolution of the fine-structured photoluminescence spectra with increasing exciton density is interpreted in terms of many-body effects which lead to an increase of the exciton self-energy and to the formation of excitonic complexes.

Acknowledgments

The studies in this thesis and the thesis itself is the culmination of much kind cooperation and patient instructions from many people. I would like to acknowledge their contributions here.

First, I would like to give my sincerest thanks to my supervisor, Professor Fujio Minami, who could see the fire through the smoke, and guided me patiently over the three short years I have spent in his laboratory.

Next, I would also like to deeply thank Dr. Nobuyuki Koguchi of the National Institute for Materials Science, for his kindness in allowing me to study crystal growth using the molecular beam epitaxy system of the Nanomaterials Laboratory, and for his guidance. Additional thanks go to all the members of the Nanodevice Group (Professor M. Kawabe, Dr. A. Ohtake, Dr. T. Noda, Dr. J. S. Kim, and Dr. T. Mano), who despite their busy research, always found the time to instruct me and give me precious advice. I am grateful for the kindness of Dr. T. Mano of the Nanodevice Group for providing the InGaAs QD samples used in this experiment.

I am grateful for Associate Professor M. Matsushita of the Department of Physics for his advice and support.

I am grateful for Professor I. Iguchi of the Department of Physics for allowing me the use of his gold sputtering system and FIB system for gold mask fabrication. Much insight into single QD spectroscopy was obtained by the use of the gold masks I was allowed to make.

I am also grateful for Associate Professor Y. Miyamoto and the Nanotechnology Support Project at the Tokyo Institute of Technology for the fabrication of many Ti masks. Much of the results in this thesis would not have been achieved without their support.

I would like to thank Professor S. Sanguinetti of the Dipartimento di Scienza dei Materiali Universita' degli Studi di Milano-Bicocca in Italy for allowing me to use his effective mass calculations code, and for the guidance and insight he gave to me concerning energy levels in QDs.

I would also like to thank Professor A. Baranov of the S. I. Vavilov Institute in Russia for his patience while introducing me to the methods of

Raman spectroscopy.

I would also like to thank Professor K. Sakoda of the National Institute for Materials Science for his guidance.

I would like to show my gratitude for Dr. T. Kuroda of the National Institute for Materials Science for his kind support.

I would also like to thank Dr. Y. Ogawa of the Physics Department, Dr. S. Fujiyoshi of the Physics Department, Dr. Y. Mitsumori of Tohoku University, Dr. A. Hasegawa of the National Institute of Information and Communications Technology, and Dr. M. Matsushita of Furukawa Electric Co. for their constant support and guidance.

I would also like to thank all my colleagues of Minami Laboratory who have worked with me throughout the three years at the laboratory.

Finally, I would like to thank the the Grant-in-Aid for Scientific Research by the Ministry of Education, Culture, Sports, Science and Technology of Japan, and the 21st Century Center of Excellence (COE) Program at Tokyo Tech “Nanometer-Scale Quantum Physics” by the Ministry of Education, Culture, Sports, Science and Technology of Japan for various financial support.

Contents

1	Introduction	8
1.1	Historic overview	8
1.1.1	Mixed crystals, heterojunctions and bandgap engineering	8
1.1.2	Device fabrication and nanoscale structuring	9
1.2	Semiconductor quantum dots	10
1.2.1	Confinement of carriers	10
1.2.2	Optical properties of QDs	14
1.3	Outline of this thesis	15
1.3.1	Quantum dot growth and sample evaluation	15
1.3.2	Resonant Raman spectroscopy of InGaAs QDs	16
1.3.3	Pressure dependence of GaAs QD PL	16
1.3.4	Single GaAs QD micro-PL spectroscopy	16
1.3.5	Quantum wire(QWR)-like GaAs QDs	16
2	QD growth and sample evaluation	20
2.1	Introduction	20
2.2	QD growth by MBE	21
2.2.1	MBE	21
2.2.2	RHEED and surface reconstruction	23
2.2.3	Mixed crystal growth	25
2.2.4	Interdiffusion	25
2.2.5	Epitaxial crystal growth modes	29
2.3	Droplet epitaxy	31
2.4	Modified droplet epitaxy	31
2.4.1	Growth of low density GaAs QDs by MDE	32
2.4.2	Growth of low density GaAs QDs	34
2.4.3	Low density GaAs QD sample evaluation	37
2.4.4	GaAs QDs samples with different AlGaAs compositions	41
2.5	Heterogeneous droplet epitaxy	43

3	Resonant Raman spectroscopy of InGaAs QDs	47
3.1	Introduction	47
3.2	Experimental setup	48
3.3	Results	50
3.3.1	PL	50
3.3.2	Resonant Raman spectra of samples with different annealing temperatures	52
3.3.3	Deformation potential interactions	53
3.3.4	Frölich interactions	54
3.4	Conclusions	56
4	Pressure dependence of GaAs QD PL	60
4.1	Introduction	60
4.2	Experimental setup	62
4.3	Results	65
4.4	Conclusions	68
4.4.1	Determination of the QD band lineup	68
4.4.2	Effective mass approximation calculations of the energy levels	70
5	Single GaAs QD micro-PL spectroscopy	78
5.1	Introduction	78
5.2	Experimental setup	80
5.2.1	micro-PL	80
5.2.2	Gold mask design and fabrication	81
5.2.3	Titanium mask design and fabrication	85
5.3	Results	85
5.3.1	Single QD spectroscopy using a gold mask	85
5.3.2	Single QD spectroscopy using a titanium mask	90
5.3.3	Single QD spectroscopy	96
5.4	Conclusions	106
5.4.1	Energy levels of the GaAs QD	106
5.4.2	Many-carrier correlations in a GaAs QD	112
6	QWR-like GaAs QDs	128
6.1	Introduction	128
6.2	Experimental setup	128
6.2.1	GaAs/Al _{0.405} Ga _{0.595} As sample	128
6.2.2	micro-PL	129
6.3	Results	129
6.3.1	Zeeman splitting	129

6.3.2	Excitation intensity dependence	129
6.3.3	PL polarization	132
6.4	Conclusions	135
7	Conclusion	137

Chapter 1

Introduction

1.1 Historic overview

Semiconductor device development finds its beginnings in the invention of the point-contact transistor by Bardeen and Brattain as an alternative to vacuum tubes in 1948[1, 2]. Since then, new and improved transistor designs have progressed hand-in-hand with the development of crystal growth technology and an increased understanding of the physics of semiconductors. With the advent of ultra-high vacuum technology in the last 30 years, semiconductor crystal quality has improved drastically. This played a critical role in achieving new methods of crystal growth, such as liquid phase epitaxy (LPE) and molecular beam epitaxy (MBE). Using these methods has made possible the growth of binary compound semiconductor crystals such as gallium arsenide (GaAs), for use in novel devices such as semiconductor lasers[3] and other opto-electronic devices. The heteroepitaxial growth of crystals has introduced versatile structures such as quantum wells, quantum wires, and quantum dots.

1.1.1 Mixed crystals, heterojunctions and bandgap engineering

The first transistors were made of germanium (Ge). Silicon (Si) became the base material for most semiconductor transistors and various other devices thereafter, and its electrical, chemical and mechanical properties made it a good candidate for use in large scale integrated circuits (LSIs). When designing opto-electronic devices, however, both materials were undesirable due to their indirect bandgap, wherein the conduction band edge and valence band edge are not both at $k = 0$ in the reciprocal lattice space, thus leading to

inefficient light emission by electron-hole recombination. In the development of devices such as laser diodes and light emitting diodes (LEDs), III-V binary compound semiconductor crystals such as GaAs became important materials due to their highly efficient emission, direct bandgap, high electron mobility, and ease of high-quality crystal growth.

To maximize these qualities to the fullest in such opto-electronic devices, the ability to control the bandgap by fabricating III-V group mixed crystals became favorable, because the bandgap directly determines the optical emission wavelength, and the bandgap can be tuned continuously by changing the mixed crystal composition. This was particularly important when considering the optical communications wavelength, which was defined by the wavelength-dependent transmission efficiency of optical fibers. For example, a mixed crystal such as $\text{In}_{1-x}\text{Ga}_x\text{As}_y\text{P}_{1-y}$ has a bandgap which depends on its composition (x and y), and was used in devices which emit light at optical communication wavelengths[4]. These III-V group mixed crystals, which are formed by a mixture of various III-V group compounds, have a given bandgap which can be continuously tuned in a variety of ranges.

The heteroepitaxial growth of two materials with different bandgaps but with nearly equivalent lattice-constants forms a heterojunction, in which the misalignment of the conduction and valence bands at the material interfaces occurs, forming a potential well. This forms the “band offset”, or the difference between the band edges of the two materials, which can be “tailored” to have a desired value. This, combined with mixed crystal growth, is known as bandgap engineering, and is the basis for the double heterojunction laser[5], in which its efficient injection of carriers due to its band offset results in its much lower threshold current density for lasing.

The understanding of the electronic properties of mixed crystals and heterojunctions has been considered a matter of great importance, and is still being pursued today.

1.1.2 Device fabrication and nanoscale structuring

Semiconductor devices have been ever increasing in structural complexity, integration, and miniaturization since its conception, driven by demands for higher performance of these devices, such as higher memory capacity in metal-oxide-semiconductor (MOS) dynamic random access memory (DRAMs). The ability to mass produce such devices depends heavily on the capabilities of well developed fabrication techniques, such as lithography and plasma dry etching. It has been forecast that the DRAM half-pitch will reach the 45nm-limit of optical lithography by 2010[6], and no alternative industrial solutions are known as of yet. Thus, novel technologies for fabrication in the

nanometer scale are currently being pursued.

There are two approaches to fabricating devices in the nanometer scale: top-down and bottom-up. The top-down approach utilizes conventional device fabrication techniques to achieve novel nanometric structures. The bottom-up approach utilizes the self-assembly and self-organization of nanometric structures by chemical techniques. Using these approaches, various novel nanometric structures such as quantum wells, superlattices, quantum wires, and quantum dots have been grown and studied.

These structures are seen not only as alternatives to current devices, but promise to have properties unseen in conventional devices. Quantum effects have been known to appear prominently as the dimensions of the devices enter the nanometer range[7], thus requiring a thorough reconsideration of both the basic physics and the design of such small devices. As the size reduction of semiconductor devices continues into the nanometric order, such novel nanometric structures will most likely play a central role not only in opto-electronics, but in the field of electronics as a whole.

1.2 Semiconductor quantum dots

1.2.1 Confinement of carriers

Nanometric structures such as quantum wells(QWs), quantum wires(QWRs), and quantum dots(QDs) are semiconductor crystals of reduced dimensionality, usually encased in a host bulk semiconductor crystal (barrier material) which has a higher bandgap than that of the nanometric structure. These heterostructures form band offsets, which results in the formation of a potential well and thus the confinement of injected carriers into the active material. In the case of QWs, the active material is reduced in thickness to the order of the Bohr radius of the exciton, resulting in the two-dimensional confinement of the carriers. In the case of QWRs, the confinement is one-dimensional, and in QDs, zero-dimensional. The confinement of the carriers results in a change in the carrier density of states, due to the reduction in the degrees of freedom of motion. Schematic representations of the bulk, QW, QWR, and QD structures are shown in figure 1.1, along with the corresponding density of states in figure 1.2.

In QDs, the carriers are confined as standing waves in three dimensions. Thus, the energy levels of a QD are discrete, much like those of an atom. The bandgap of the QD is determined by the bulk bandgap offset by

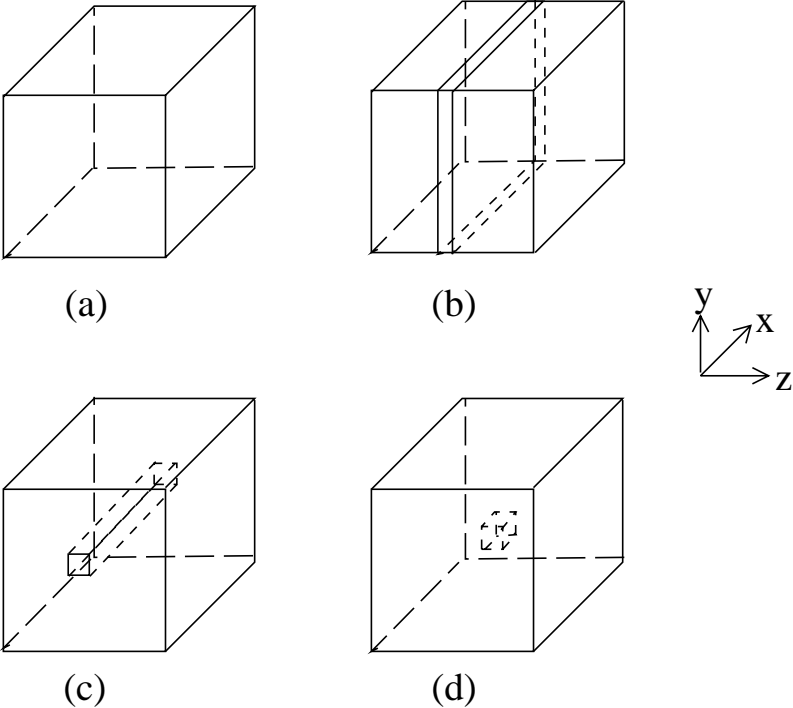


Figure 1.1: Schematic representations of (a) bulk (b) QW (c) QWR (d) QD structures

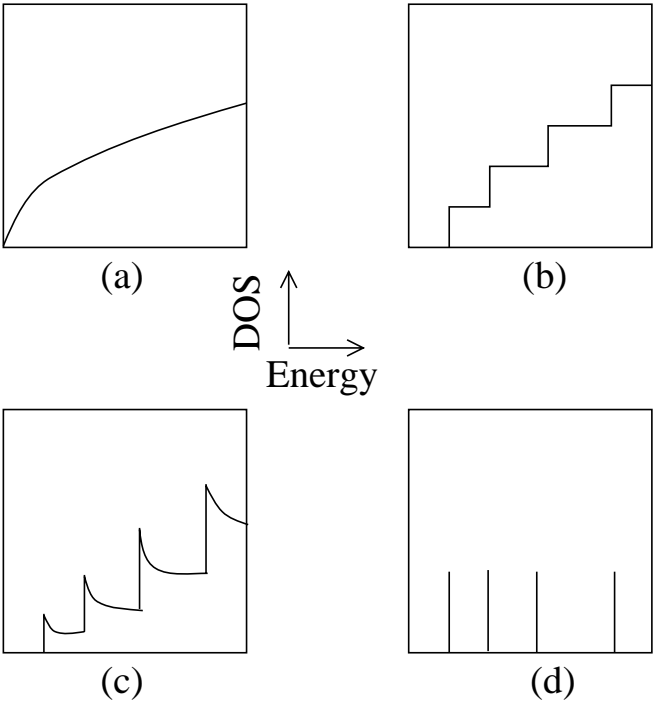


Figure 1.2: Density of states (DOS) of (a) bulk (b) QW (c) QWR (d) QD structures

$$\Delta E = \frac{\hbar^2}{2m^*} \left(\left(\frac{n_x \pi}{L_x} \right)^2 + \left(\frac{n_y \pi}{L_y} \right)^2 + \left(\frac{n_z \pi}{L_z} \right)^2 \right). \quad (1.1)$$

where \hbar is Planck's constant over 2π , m^* is the effective mass of a free carrier, $L_{x,y,z}$ are the distances in space of the confined carrier, and $n_{x,y,z}=1,2,3,\dots$. Here, infinite potential barriers are assumed. This is known as the confinement energy of the carrier in the QD. Thus, the bandgap can be tuned to a desired energy simply by changing the size of the QD. The shape, composition, barrier material, and lattice strain due to lattice mismatch between the QD and barrier material also affect the QD's energy levels, and thus its bandgap.

Conventional QD formation relies on the lattice mismatch between the QD and barrier material. Due to the QD lattice strain induced by the employment of such a method, as well as structural ambiguity, the modeling of QDs to correctly reconstruct the measured QD energy levels was difficult. Strain alone has been reported to form additional harmonic potential wells in a quantum well layer with highly localized strain[8]. Furthermore, the formation of a wetting layer cannot be avoided in conventional QD formation methods. The existence of the wetting layer has been shown, in some cases, to invalidate the near-zero dimensional assumption of the QD[9]. As a new approach to studying the energy levels of QDs, the use of a lattice-matched QD system such as GaAs/AlGaAs with a well-defined structure has been employed in this study. Such QDs can be made by modified droplet epitaxy, and will be discussed in detail in chapter 2.

The primary difference between using a bulk mixed crystal and a QD for optoelectronic devices, is that the density of states, which are delta-function like for QDs, give a much sharper optical emission spectrum. As can be seen from figure 1.2d, the density of states (DOS) of QDs are delta-function like due to the zero degree of freedom of motion, i.e. the complete confinement of carriers in all three dimensions. The DOS of a QD $D(E)$ is given as a series of delta functions summed over all possible states as

$$D(E) = 2N_D \sum_{n_x, n_y, n_z} \delta(E - E_{n_x} - E_{n_y} - E_{n_z}). \quad (1.2)$$

where N_D is the volume density of the QDs.

When determining the energy levels of a QD, conventional methods of QD energy level measurement studies an ensemble of QDs, resulting in the observation of an inhomogeneously broadened density of states. This makes it impossible to identify and characterize energy levels of a single QD, especially the fine structure splitting of such energy levels. Thus, it becomes necessary

to study each QD individually.

One of the most important aspect of semiconductor QDs is its role in studying the correlations between a countable numbers of confined elementary particles. The essential difference between a solid state material and an atom trapped in a magneto-optical trap, for example, is that in the solid state case, the interactions between electrons/holes and other electrons/holes, as well as the interactions between electron-hole pairs (excitons) and phonons are inherent phenomena. Such many-particle correlations are of great importance in understanding QD confinement energy levels, because the single confined exciton picture does not give the correct confinement energy levels; renormalizations due to many-particle effects must be taken into account. These energy level renormalizations are expected to be of the order of several meV to several hundred μeV , and thus can only be resolved in single QD energy level measurements, as argued above. Many particle correlations in QDs are also important as a problem in many-body physics.

1.2.2 Optical properties of QDs

Emission of radiation from QDs involves both luminescence and Raman scattering processes, as is the case for bulk semiconductors. The measurements of such emissions give information of the electron/hole-electron/hole and exciton-phonon interactions in the QD, respectively, because luminescence involves real excitation of electrons, while in light scattering typically virtual excitation of electrons occurs with the help of momentum conservation by phonon emission/absorption.

Resonant Raman spectroscopy of QDs involve the interband excitation of confined carriers, and their relaxation via interactions with phonons. Thus, studying resonant Raman spectra of QDs give important information concerning confined exciton-phonon interactions.

Photoluminescence (PL) spectroscopy of QDs involve the excitation of carriers in the barrier material, whereupon they eventually fall into the potential well of the QD. The confined carriers fall to the lowest confined state (ground state) of the QD, and due to Pauli's principle, fill each state with two opposite spin carriers. These confined carriers usually recombine from the ground state, but recombinations from higher states are also observable, when state filling occurs as the average number of optically injected carriers are increased. This gives information concerning the energy levels of the QD as well as the many-carrier correlations in the QD. Optical measurements are advantageous here, as experiments such as transport measurements fill only the ground states.

In most QD growth methods, many QDs are grown at once, and these

QDs have a size distribution, due mainly to the thermal fluctuations during QD crystal growth. Thus, an ensemble of QDs with a size distribution has a PL spectrum broadened by the overlap of very sharp PL lines which are slightly shifted in energy. Single QD PL is necessary in order to attribute the various PL lines in the PL spectrum to recombination emissions from confined carrier energy levels, as well as the confined carrier correlation energies. Thus, the ability to observe single QD PL spectra is highly important. The two most common methods of achieving single QD PL spectra are the reduction of the density of the QDs, and the reduction of the number of excited/observed QDs by the introduction of diffraction-limited microscopy. In this study, both methods are adopted, and the best trade-off between high spectral resolution-single QD PL spectroscopy and high signal-to-noise ratio is pursued by combining various methods of microscopy with ultra-low density QD samples. Broad-band single QD spectra are obtained in this way.

1.3 Outline of this thesis

This thesis is organized as follows.

1.3.1 Quantum dot growth and sample evaluation

In chapter 2, an introduction of QD growth by molecular beam epitaxy will be given. This will be followed by a short historical overview of droplet epitaxy[10]. QDs made by droplet epitaxy have no dislocations nor wetting layer, and are considered to be the ideal QD embedded in a crystal matrix. Due to the hierarchical growth method employed, it is possible to grow unique QD systems such as lattice-matched GaAs/AlGaAs QDs. Not only do these GaAs/AlGaAs QDs emit at the important 600nm range for plastic fibers, they also form pyramidal QDs without any strain, making the analysis of the QD energy levels much simpler.

Low density GaAs QD growth by modified droplet epitaxy[11] will be explained and the low density samples grown for this study will be evaluated. These low density samples will be used in later chapters to show that, for the first time, broadband PL spectra of single GaAs/AlGaAs QDs made by modified droplet epitaxy have been observed and analyzed.

InGaAs/GaAs QDs grown by heterogeneous droplet epitaxy will also be explained[12]. These QDs also have no wetting layer, and have a barrier that is transparent to the QD PL line, making these QDs an appropriate sample for resonant Raman spectroscopic studies.

1.3.2 Resonant Raman spectroscopy of InGaAs QDs

In chapter 3, InGaAs/GaAs QDs samples made by heterogeneous droplet epitaxy and annealed at different temperatures are studied by resonant Raman spectroscopy in order to study the effects of QD/barrier interface interdiffusion on the deformation potential interactions and Frölich interactions.

1.3.3 Pressure dependence of GaAs QD PL

In chapter 4, PL from high density GaAs/AlGaAs QDs samples made by modified droplet epitaxy are studied under high hydrostatic pressure to determine the band offset and, consequently, the QD/barrier band lineups. The results are compared to effective mass approximation calculations.

1.3.4 Single GaAs QD micro-PL spectroscopy

In chapter 5, single GaAs/AlGaAs QDs from ultra-low density samples are studied to determine what single QD emission lines have in relation to their energy levels as well as the carrier correlation energies.

Initially, a mask combined with diffraction-limited microscopy (micro-PL method) is used to verify the spectral characteristics of single QD spectra. These characteristics are compared to those of QD spectra taken using the micro-PL method without a mask. It is found from similarities of the characteristics of these two spectra that single QD spectra can be observed without a mask due to the ultra low density of the sample. Thus, no mask is used in order to obtain single QD spectra with high spectral resolution and high signal-to-noise ratio.

From the excitation intensity dependence of the single QD spectra, the energy levels of a GaAs QD are determined. Using the band offset determined in chapter 4, the same effective mass approximation calculations are computed to determine the correct energy level spacings of this sample, which can be attributed to the various spectral peak spacings in single QD spectra.

From the excitation intensity dependence of the single QD spectra, many-carrier correlations in a QD are also determined, and a clear QD size dependence in these correlations will be shown.

1.3.5 Quantum wire(QWR)-like GaAs QDs

Using the same micro-PL setup as used in chapter 5, highly anisotropically shaped QD are studied in chapter 6, and their many-carrier correlations are studied. The shape of the confinement potential is similar to that of a

quantum wire (QWR). The self-energy of localized one dimensional excitons is renormalized at increasing excitation density, and this is observed from the excitation intensity dependence of the single QWR-like QD's PL spectrum.

Bibliography

- [1] Bardeen, J., Brattain, W., *The transistor, a semi-conductor triode*, Phys. Rev. **74**, 230 (1948)
- [2] Koma, A., Yagi, K., Tsukada, M., Aono, M., *Introduction to Surface Science*, Maruzen Tokyo (1994)
- [3] Hall, R. N., Fenner, J. G. E., Kingsley, J. D., Soltys, T. J., Carlson, R. O., *Coherent Light Emission From GaAs Junctions*, Phys. Rev. Lett. **9**, 366 (1962)
- [4] Nagai, H., Adachi, S., Fukui, T., *III-V Mixed Crystals*, Corona Tokyo (1988)
- [5] Kroemer, H., *A proposed class of heterojunction injection lasers*, Proc. IEEE **51**, 1782 (1963)
- [6] *International Technology Roadmap for Semiconductors (2003 Edition) Lithography*, <http://public.itrs.net/>
- [7] Arakawa, Y., Sakaki, H., *Multidimensional quantum well laser and temperature dependence of its threshold current*, Appl. Phys. Lett. **40**, 939 (1982)
- [8] Nishibayashi, K., Okuno, T., Masumoto, Y., Ren, H.-W., *Luminescence quantum beats of strain-induced GaAs quantum dots*, Phys. Rev. B **68**, 035333 (2003)
- [9] Robinson, H. D., Goldberg, B. B., Merz, J. L., *Observation of excitation transfer among neighboring quantum dots*, Phys. Rev. B **64**, 075308 (2001)
- [10] Koguchi, N., *Growth of GaAs epitaxial microcrystals by Droplet Epitaxy*, Nihon Kinzoku Gakkai Kaiho **32**, 485 (1993)

- [11] Watanabe, K., Koguchi, N., Gotoh, Y., *Fabrication of GaAs quantum dots by Modified Droplet Epitaxy*, Jpn. J. Appl. Phys. **39**, L79 (2000)
- [12] Mano, T., Watanabe, K., Tsukamoto, S., Fujioka, H., Oshima M., Koguchi, N., *New self-organized growth method for InGaAs quantum dots on GaAs(001) using droplet epitaxy*, Jpn. J. Appl. Phys. **38**, L1009 (1999)

Chapter 2

QD growth and sample evaluation

2.1 Introduction

Among the many ways of epitaxially growing semiconductor crystals, molecular beam epitaxy (MBE) has been in the forefront of novel nanometric structures research due to MBE's high growth controllability. A variety of methods have been proposed for QD growth using MBE. Of these, modified droplet epitaxy and heterogeneous droplet epitaxy are two novel methods which overcome many of the issues facing conventional QD growth methods.

In this study, GaAs/AlGaAs QDs are prepared by modified droplet epitaxy. QDs made by this method have no strain and wetting layer, whereas these characteristics are mostly unavoidable when making QDs by the conventional Stranski-Krastanov growth mode. The details of these differences will be explained later. GaAs/AlGaAs QD samples with low density are prepared to make possible for the first time broadband single QD spectroscopy of GaAs/AlGaAs QDs made by modified droplet epitaxy. Two such low density samples with different barrier bandgaps are also prepared.

InGaAs/GaAs QDs prepared by heterogeneous droplet epitaxy[1, 2, 3, 4] are also used. QDs made by this method are strained, but have no wetting layer. The details of this growth method will be explained later in this chapter. InGaAs/GaAs QDs grown with different post-growth annealing temperatures are used.

2.2 QD growth by MBE

2.2.1 MBE

MBE is a vacuum evaporation method for epitaxial crystal growth, the most important characteristic being the high vacuum achieved inside the growth chamber of the MBE system. An ultra-high vacuum on the order of 10^{-10} Torr can be achieved using a combination of turbo molecular pumps, liquid nitrogen (LN_2) shrouds, and other ultra-high vacuum pumps. This allows the elemental sources, which are individually heated and evaporated inside a specialized heating oven known as a Knudsen cell (K-cell), to travel as atomic or molecular beams toward the growth substrate unperturbed. Another important characteristic of the MBE system is the ability to do in-situ monitoring of the growth surface by various methods which require a high vacuum, such as reflection high energy electron diffraction (RHEED). These characteristics make possible the epitaxial growth of high quality crystals by controlling the supplied amount and flux of the crystal's constituent elemental materials, as well as the growth substrate temperature. A schematic representation of the MBE system is shown in figure 2.1.

The MBE system used for sample growth is a Riber-32P MBE system with solid elemental sources and an EPI (Veeco)-valved As cracking source, which enables the rapid irradiation of a high As_4 flux.

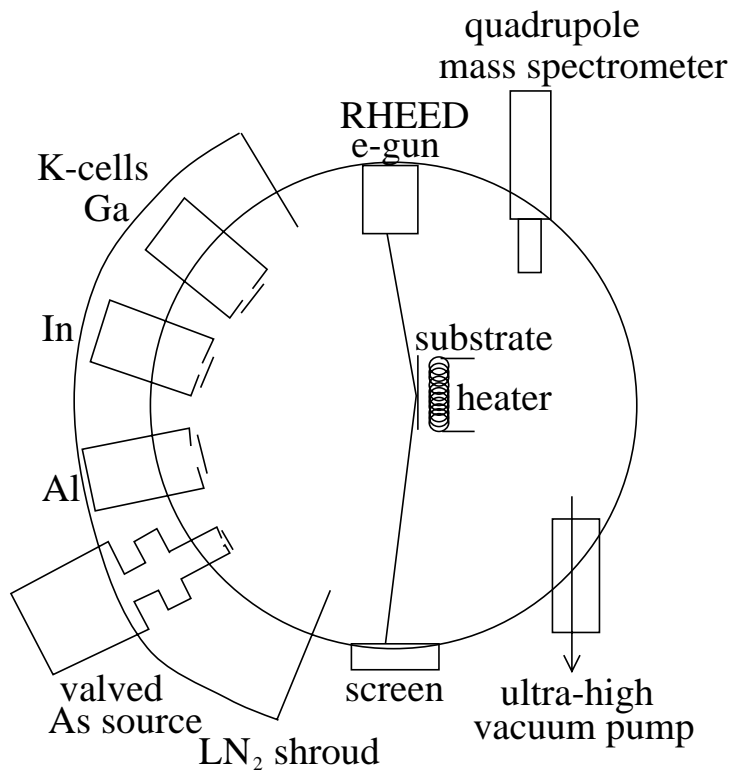


Figure 2.1: Schematic representation of an MBE system

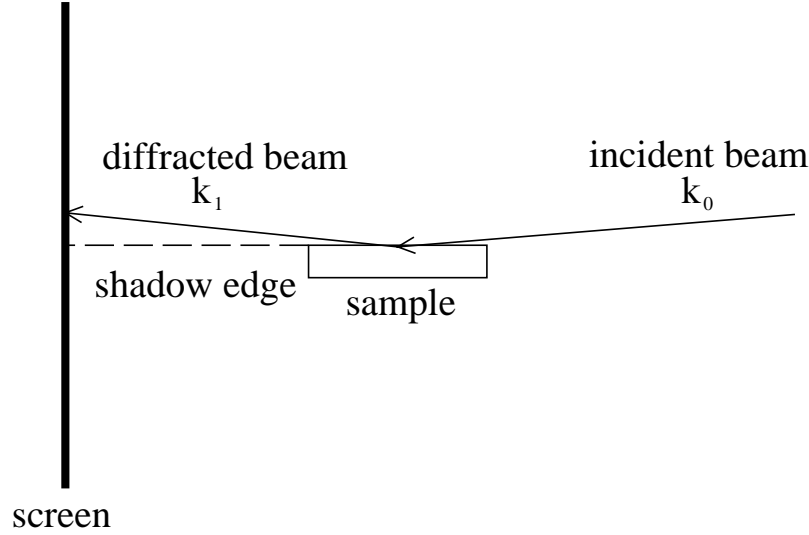


Figure 2.2: Schematic representation of an RHEED setup

2.2.2 RHEED and surface reconstruction

In an RHEED setup, an electron beam is directed so as to skim the sample surface at a very low angle of $1\sim 2^\circ$, resulting in the diffraction of the electrons by the surface atoms, as shown in figure 2.2. By studying the diffraction patterns of the electrons on a fluorescent screen, the growth surface reconstruction can be studied in real time.

An RHEED pattern is constructed from the points where the Ewald sphere coincide with the reciprocal lattice points of the surface atoms, as shown in figure 2.3. The radius of the Ewald sphere is defined as $|\mathbf{k}_0| (= |\mathbf{k}_1|)$; diffraction occurs when Laue's equation (equation 2.1) is satisfied.

$$\mathbf{k}_1 - \mathbf{k}_0 = \mathbf{r}^* \quad (2.1)$$

Here, \mathbf{k}_0 and \mathbf{k}_1 are the wave vectors of the incident and diffracted electron beams, respectively, and \mathbf{r}^* is the reciprocal lattice vector of the crystal.

Diffraction patterns differ depending on the direction of the incident electron beam relative to the surface crystal axis. This is due to the fact that the

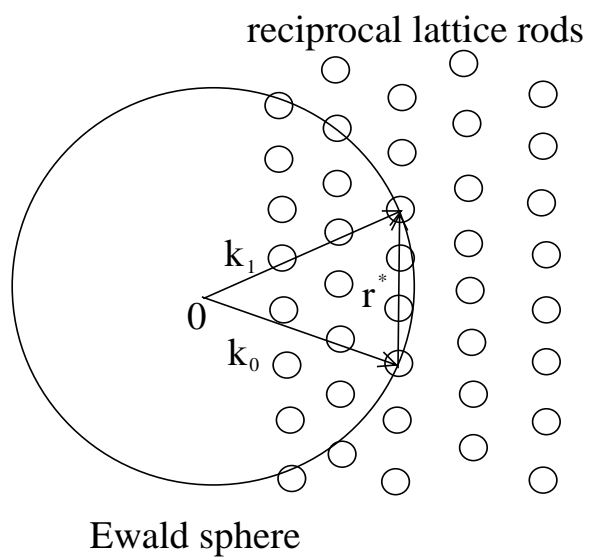


Figure 2.3: RHEED diffraction conditions

difference in the periodicity of the reconstruction of the surface atoms leads to the difference in the diffracted electron patterns. In the case of growth on a GaAs (001) surface, the $\langle 010 \rangle$, $\langle 110 \rangle$, and $\langle 1\bar{1}0 \rangle$ crystal axis directions are the incident beam directions which give important information concerning the surface reconstruction. In this case, the surface reconstruction depends on the surface coverage of As (θ_{As}). As will become important later, the periodicity of the surface is related to whether the surface is As-stabilized ((2×4) , $c(4 \times 4)$ surface) or Ga-stabilized ((4×1) , (4×2) surface). These periodic structures are two-dimensional, so the reciprocal lattice take the form of rods perpendicular to the surface; thus the RHEED patterns are streak-like. As the surface becomes roughened, the effects of three-dimensional islands on the electron beam becomes prominent, changing the RHEED pattern from a streak-like pattern to a spotty pattern.

The oscillatory behavior of the RHEED pattern intensity has been shown to be directly related to the single molecular layer surface growth; i.e., as the two-dimensional islands form, combine to recreate a new, flat surface, and two-dimensional islands begin to form again, the RHEED pattern intensity changes periodically in time. By monitoring this periodicity during the growth of a surface, it is possible to control the amount of material that is supplied to the surface (surface coverage) as well as the growth rate[5].

2.2.3 Mixed crystal growth

III-V mixed crystals can be grown using MBE by supplying different group III elemental materials during growth. The composition x depends on the growth rate ratio of the different group III materials. In the case of the mixed crystal $A_x^{III}B_{1-x}^{III}C^V$, the composition x is given as

$$x = \frac{GR_A}{GR_A + GR_B} \quad (2.2)$$

where GR_A and GR_B are the growth rates of material $A^{III}C^V$ and $B^{III}C^V$, respectively. Mixed crystals can also be achieved by first supplying the different group III elemental materials to form metal alloy droplets, and subsequently crystallizing these alloy droplets. This method will be explained later in this chapter.

2.2.4 Interdiffusion

Mixed crystal growth can also occur at the QD heterojunctions and is caused by the interdiffusion of group III elemental materials due to annealing. In the case of the interface between the mixed crystal $A_x^{III}B_{1-x}^{III}C^V$ surface and

$B^{III}C^V$ surface, a diffusion profile for the concentration of material A^{III} exists at the interface.

Interdiffusion at the QD-barrier interface is studied using the method employed by Sanguinetti, et. al.[6], in which, in the case of GaAs/AlGaAs QDs, the pyramidal QD shape is approximated by a cone shape, and the diffusion of material A^{III} is considered to be isotropic; the cone is split into discs which diffuse two-dimensionally in the lateral direction, as well as in the longitudinal direction of the cone, as shown in figure 2.4.

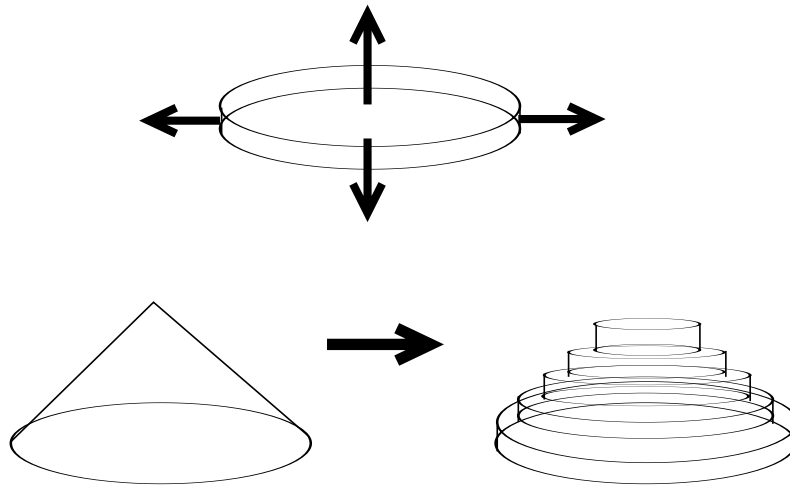


Figure 2.4: Direction of diffusion in a disc, and the approximation of a cone-shape by numerous discs

The diffusion in the longitudinal direction is set by connecting the surface composition between discs. The expression for diffusion of a disc in the lateral direction is expressed by the diffusion of the material A^{III} , the diffusion constant being independent of composition. The composition of the material A^{III} at a distance $|\vec{r}|$ from a point source in an infinite volume is expressed using D as the diffusion constant, and t as time[7]. If we set $\sqrt{Dt} = l(T)$ as the annealing-temperature dependent interdiffusion length at the mixed crystal interface, the following equation holds;

$$x(\vec{r}) = \frac{1}{8(\pi l^2(T))^{\frac{3}{2}}} \int x_0(\vec{r}_1) \exp\left(-\frac{(|\vec{r} - \vec{r}_1|)^2}{4l^2(T)}\right) d\vec{r}_1. \quad (2.3)$$

Here, the initial distribution of material A^{III} is $x_0(\vec{r})$. The interdiffusion length $l(T)$ will be used as a parameter in the calculations of the QD energy levels later in this dissertation.

An example of a diffusion profile at the interface in the case of $l=2.5\text{nm}$ is shown in figure 2.5. Here, the plotted numerical values (c) represent the spatial dependence of the concentration of material A^{III} in the QD material. When the value of c is 1, the concentration of material A^{III} is 0, and when c is 0 the concentration of material A^{III} is 0.3. Any intermediate value of c between 0 and 1 can be connected to the the concentration of material A^{III} in that position through the formula $(1 - c) \times 0.3$.

The shape of the QD before annealing is that of a cone with a base diameter of 20nm and a height of 16nm. The initially triangular concentration profile is rounded at the corners, and an overall size reduction is seen after interdiffusion. The resulting change in shape from a pyramidal shape to a nearly-spherical shape is in agreement with HRSEM images of cross sections of buried and annealed GaAs/AlGaAs QDs after stain etching[8].

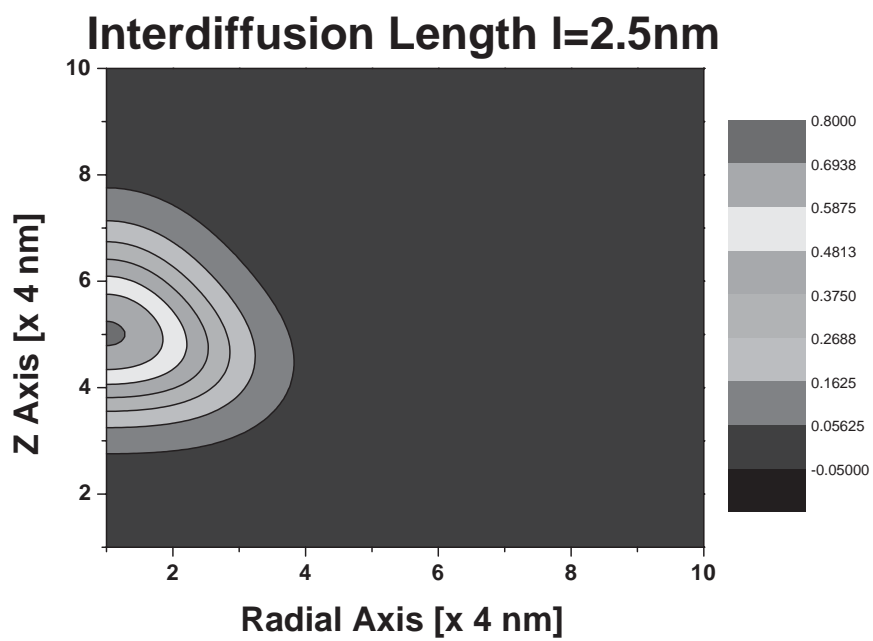


Figure 2.5: An example of a diffused concentration profile

2.2.5 Epitaxial crystal growth modes

The three typical epitaxial crystal growth modes are shown in figure 2.6.

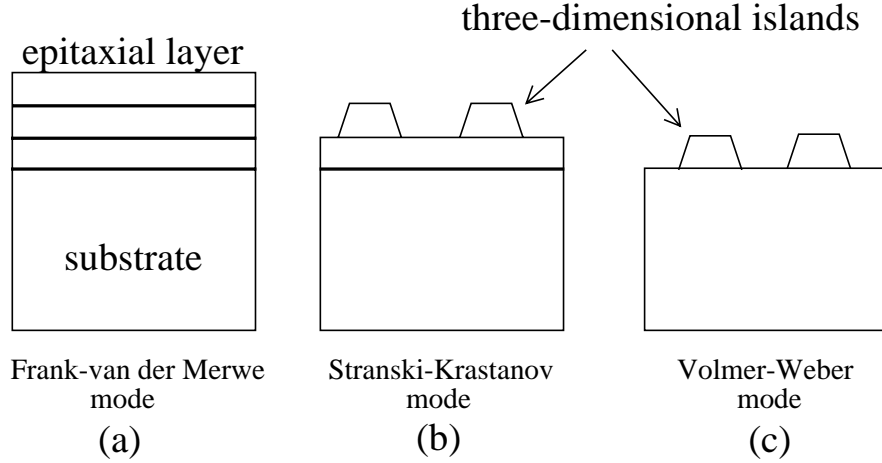


Figure 2.6: Epitaxial crystal growth modes

In Frank-van der Merwe (FM) mode, two dimensional nuclei form on the surface, which grow and join together to cover the entire surface. This process is repeated to grow one atomic layer of material at a time. In Stranski-Krastanov (SK) mode, two dimensional nuclei form into a two dimensional layer, which, upon reaching a critical thickness, form three dimensional islands on top of the two dimensional layer. In Volmer-Weber (VW) mode, three dimensional islands form upon the initiation of growth[9].

The actual growth modes are determined by the balance between the substrate-epitaxial layer strain energy due to lattice mismatch, the surface energies of the substrate and epitaxial layer, and the surface energy of the heterointerface. Generally, the stability of a growth mode is argued in terms of a droplet model[10]. As seen in figure 2.7, when a droplet with an angle t is formed stably on top of a substrate, Young's equation is satisfied:

$$E_A \cos(t) + E_{AB} = E_B \quad (2.4)$$

Here, E_A is the surface energy of the droplet, E_B is the surface energy of the substrate, and E_{AB} is the interface energy. When $0 < \theta < 180^\circ$, $E_B < E_A \cos(\theta) + E_{AB}$, and the droplet is stable. This condition corresponds to the VW growth mode. Furthermore, by calculating the free energy of

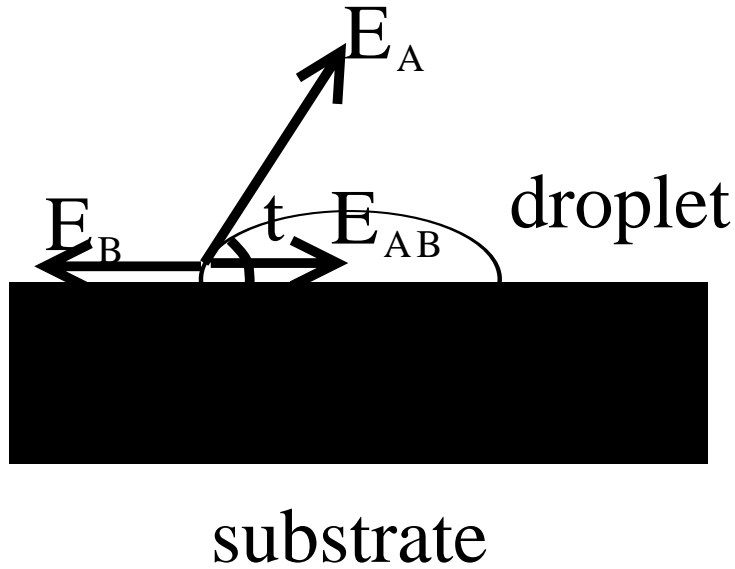


Figure 2.7: Droplet model of the growth modes

the FM, SK, and VW structure for the coverage of the epitaxial layer, one can determine which growth mode has the smallest free energy, and is thus stabler.

The three dimensional islands which form in SK and VW QD growth mode can be epitaxially covered by a different material of wider bandgap (barrier material) to realize quantum confinement of carriers into the islands, which can be considered as QDs. Conventional methods of QD growth rely

mostly on the SK growth mode; however, the existence of a wetting layer (two dimensional layer), which connect the dots, as well as the existence of strain, which affect the energy levels of the QD, are issues which accompany this growth mode.

2.3 Droplet epitaxy

Droplet epitaxy is an hierarchical epitaxial growth mode whereupon the formation of group III metallic droplets are followed by their crystallization by a group V material, in the case of III-V compound crystals. The growth process of such a mode can be described by a vapor-liquid-solid (VLS) mechanism[11]. In the VLS mechanism, an “impurity” forms a liquid alloy droplet of relatively low freezing temperature. For VLS growth of compound crystals such as GaAs, an excess of one of the component materials can act as a liquid-forming “impurity.” Initially a method for growing crystal whiskers, the growth can be stopped at the early stages to form QDs by the crystallization of nanometric droplets.

2.4 Modified droplet epitaxy

In the case of GaAs QD growth by droplet epitaxy, Ga is supplied on to a low temperature, As-terminated GaAs (001) surface. Upon supplying more Ga than the As coverage, a GaAs monolayer forms, and the excess Ga adatoms converge and form into droplets. However, after supplying As_4 , the two dimensional growth of GaAs occurs as Ga adatoms migrate from the droplets over the newly formed As-terminated surface, and the three dimensional growth of GaAs is suppressed.

In terms of growth modes, the SK mode-like growth occurs upon supplying Ga, and an FM mode-like growth occurs upon supplying As_4 to this surface. As stated earlier, a VW mode-like growth of GaAs epitaxial nanocrystals can be achieved by lowering the surface energy of the substrate relative to the droplet surface energy and interface energy. In order to form three dimensional islands by crystallizing the Ga droplets, the lowering of the surface energy by sulfur-termination of the droplet formation surface (the As-terminated surface) was initially used. Although pyramidal GaAs QDs with a base size of $25\text{nm}\times 43\text{nm}$ were seen to form with clear $\{111\}$ facets, the PL from the QDs could not be seen[12, 13, 14]. Thus, it was proposed to increase the As_4 flux irradiation used to crystallized the Ga droplets, as reported by Watanabe, et. al.[15], in order for the As atoms to be incorporated

directly into the Ga droplet from the vapor phase and to rapidly react with the Ga droplet. The two dimensional growth was restrained due to the increased consumption of Ga atoms in the droplet. This method was termed modified droplet epitaxy (MDE). This method made possible the growth of pyramidal nanostructures with strong carrier confinement in three dimensions, which was reflected in its PL spectrum, as well as the formation of QDs without strain or a wetting layer. No strain exists because of the nearly lattice-matched heterojunction. Further improvement in the PL spectrum, in terms of intensity, was observed by including a post-annealing process[8]. This process had the effect of interdiffusion at the QD interface, the details of which are written earlier in this chapter, and has been confirmed by high-resolution scanning electron microscopy (HRSEM) images of the cross sections of buried QDs after stain etching[8].

2.4.1 Growth of low density GaAs QDs by MDE

In single QD PL, a low density QD sample is desired, in order to reduce the number of QDs in the PL excitation area. The density desired is to the order of 10^8cm^{-2} . This goes against the general trend to achieve higher density QDs, and reported densities of GaAs QDs made by MDE are to the order of 10^{10}cm^{-2} [8]. Thus, QD growth conditions which differ from these higher density samples must be determined. In MDE, the density of the droplets are almost equal to the QD density, so it is safe to say that the desired QD density can be achieved by controlling the density of the droplets.

Three droplet formation parameters were taken into account in determining the best conditions for achieving low density GaAs QDs. These were the substrate temperature, the Ga flux, and the Ga supply. Watanabe, et. al. used the following droplet formation parameters: a substrate temperature of 180°C , a Ga flux of 0.5 monolayer(MLs)/s, and a Ga supply of 2.75ML or 4.75ML (both Ga supplies achieved almost the same density of 10^{10}cm^{-2})[8]. These values were used as a starting point in order to determine the low density droplet formation parameters.

Substrate temperature

Generally, a high substrate temperature achieves a lower density due the enhanced surface diffusion of the Ga adatoms, thus promoting the convergence of Ga adatoms instead of nucleation at various sites. Thus, a high droplet formation temperature of 330°C was chosen; a higher temperature would result in the re-evaporation of the surface As atoms, resulting in a roughening of the otherwise atomically smooth surface.

Ga flux

The Ga droplet density for different Ga flux is shown in figure 2.8 (the line is a guide to the eye). The substrate temperature is 330°C, and the Ga supply is 1.75ML. This Ga supply was chosen as a preliminary value greater than the As coverage at 330°C, in order to ensure the formation of droplets.

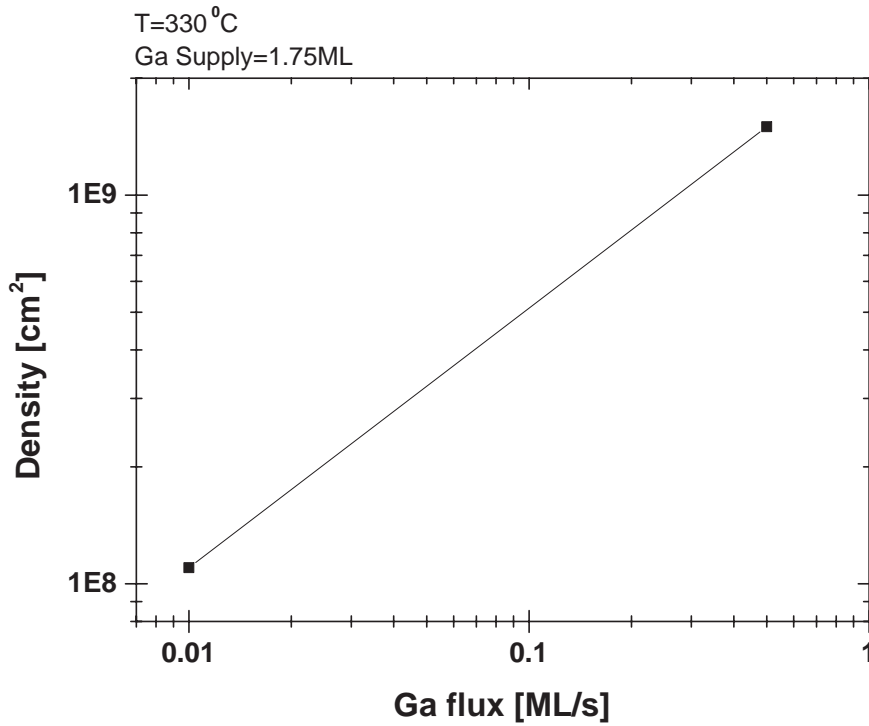


Figure 2.8: Ga droplet density for different Ga fluxes

The density decreases with flux; this result is in agreement with the predicted trend[12], and can be understood in the following way: The Ga atoms which reach the substrate surface are considered not to re-evaporate, and are all used to form the Ga-terminated surface and the Ga droplets. After the creation of a Ga-terminated surface, the time required for Ga adatoms to collide into each other while diffusing on the surface is τ_c , and is the determining factor in the formation and growth of a nucleus. From a kinetic analysis of nucleus formation and growth[12], the number of adatoms which an adatom collides into in a unit time can be expressed by the surface diffusion constant of the adatom D and the density of adatoms N_1 as

$$\tau_c = 1/DN_1. \quad (2.5)$$

When the flux, or the intensity of atoms impinging on the surface in a unit area for a unit time is J , and the critical number of adatoms needed to form a droplet is considered to be one, the dissociation of dimers do not occur, and stable nuclei larger than a dimer can be ignored. The temporal change of N_1 for $t \leq \tau_c$ can be expressed as

$$dN_1/dt = J - DN_1^2. \quad (2.6)$$

At equilibrium, N_1 can be expressed as

$$N_1 = \sqrt{J/D}. \quad (2.7)$$

After time τ_c , stable nuclei form due to the collision of adatoms, the number of such nuclei being $N_S = (N_1/\tau_c) \cdot \tau_c = N_1$. The average distance between nuclei, λ , can then be expressed as

$$\lambda^2 = 1/N_S = \sqrt{D/J}. \quad (2.8)$$

Thus, the density of droplets, or λ^{-2} , should decrease with the Ga flux J . It is interesting to note that, upon reaching equilibrium, new nuclei do not form, and the rest of the impinging Ga atoms are consumed by the existing nuclei.

Due to issues concerning the reproducibility of a flux as low as 0.01ML/s, a higher flux of 0.05ML/s was chosen.

Ga supply

The Ga supply was lowered as much as possible in order to reduce the amount of Ga adatoms which can converge into droplets. Figure 2.9 shows the droplet density and size for different Ga supplies. The substrate temperature is 330°C and the Ga supply rate is 0.05ML/s.

Droplet formation can be confirmed for a Ga supply greater than 1ML. This is in general agreement with the As coverage at 330°C for a c(4×4)α surface, which is reported to be 1ML[16, 17]. Thus, a Ga supply of 1ML was chosen.

2.4.2 Growth of low density GaAs QDs

Using the above conditions for droplet formation (a substrate temperature of 330°C, a Ga flux of 0.05ML/s, and a Ga supply of 1ML), a low density GaAs QD sample was grown using the following procedure.

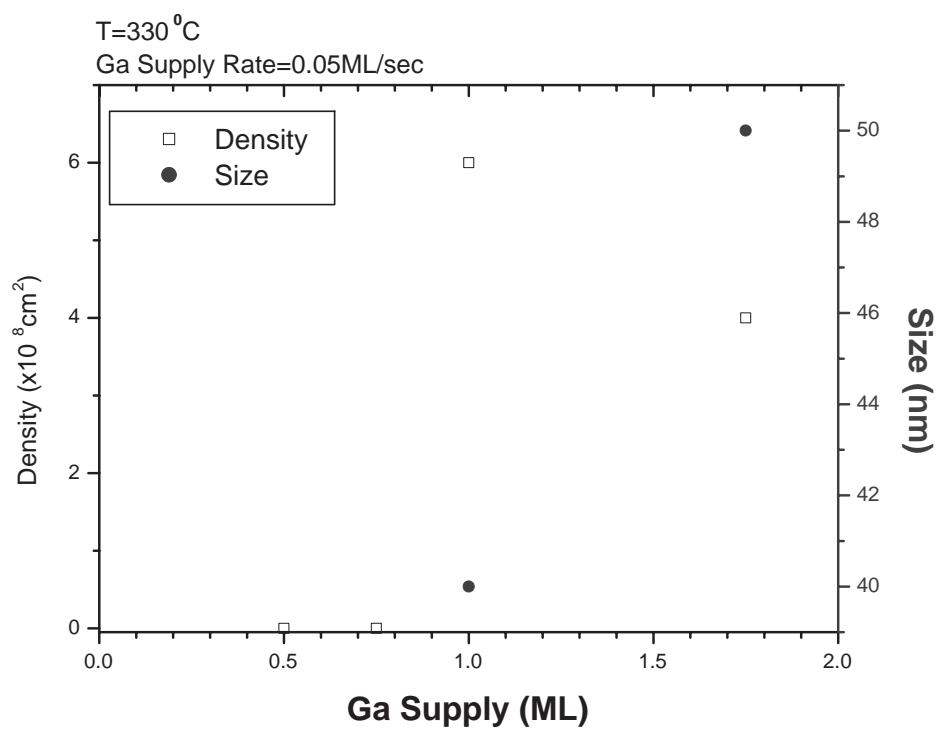


Figure 2.9: Ga droplet density and size for different Ga supplies

After native oxide desorption, a 300 nm-thick GaAs buffer layer and a 500 nm-thick AlGaAs barrier are grown on a GaAs (001) wafer at 580°C. The substrate temperature is then reduced to 330°C. The As supply is stopped, and a Ga supply of 1ML is irradiated with a Ga flux equivalent to a GaAs growth rate of 0.05 ML/s. The substrate temperature is lowered to 150°C, and these droplets are crystallized by the irradiation of a high As_4 flux. The substrate temperature is raised to 200°C, and a 10 nm-thick AlGaAs barrier layer is grown over the QDs using migration enhanced epitaxy (MEE) to avoid the two-dimensional regrowth of the QDs. The temperature is raised to 580°C, and a 90 nm-thick AlGaAs barrier and a 10 nm-thick GaAs capping layer are grown by standard MBE. The sample is consecutively annealed at 680°C for one hour. A schematic representation of the sample is shown in figure 2.10. No wetting layer exists, because any existing GaAs monolayer washes out during the annealing process, as calculated by Sanguinetti, et. al.[6].

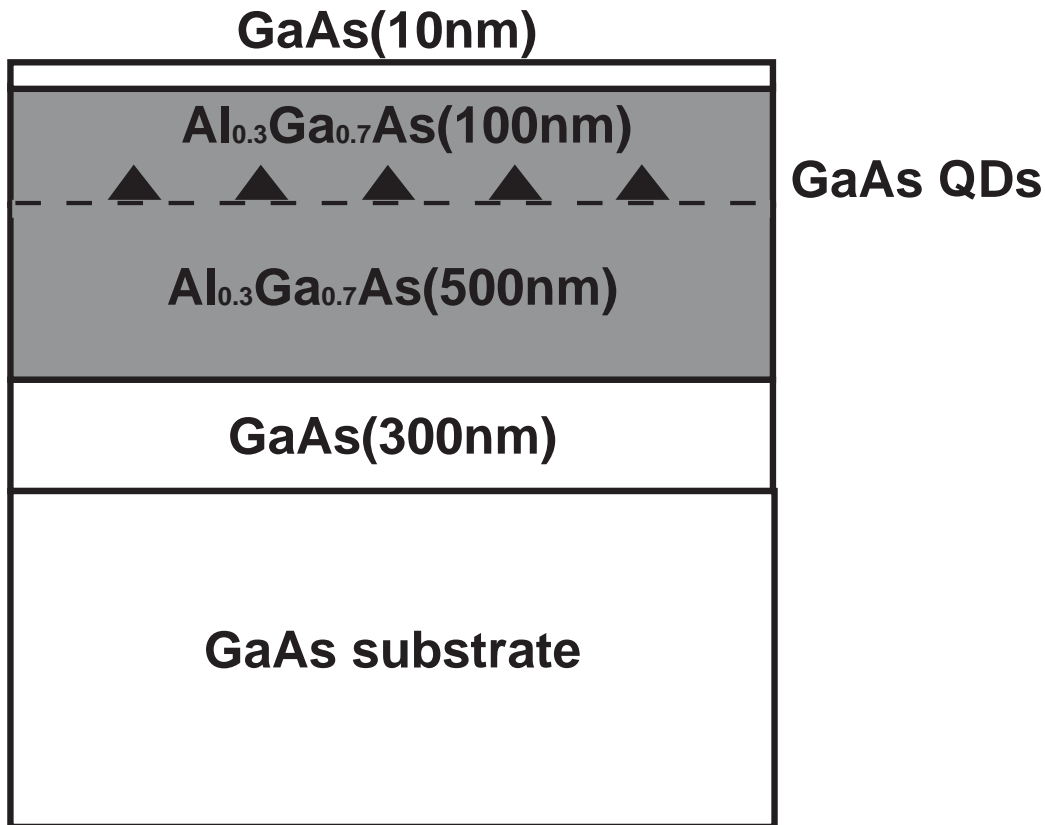


Figure 2.10: Schematic representation of the GaAs QD sample

2.4.3 Low density GaAs QD sample evaluation

A sample without a capping layer, i.e. a sample in which the growth process is stopped after Ga droplet crystallization, is studied to evaluate the sample.

RHEED pattern evaluation

The RHEED patterns during the droplet formation and crystallization processes are studied to understand the surface reconstruction during these growth processes. The RHEED patterns are shown in figure 2.11. After

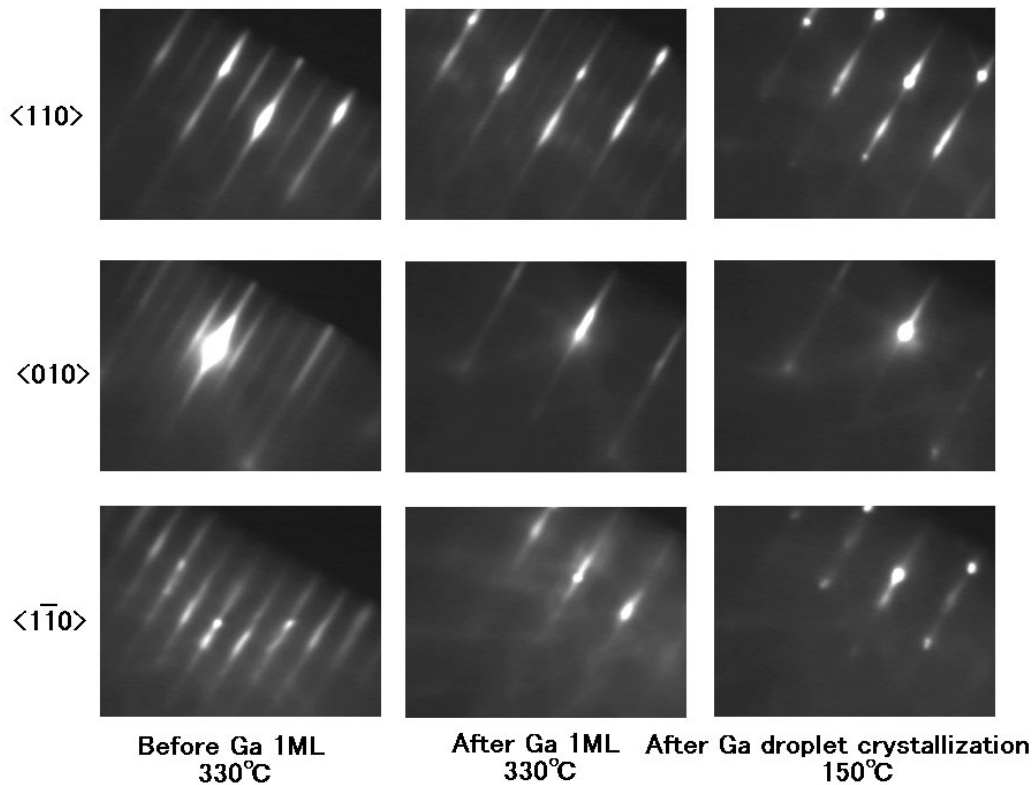


Figure 2.11: RHEED patterns during growth of low density GaAs QDs

supplying 1 ML of Ga, the surface changes from an As-rich $c(4 \times 4)\alpha$ surface to that of a mostly Ga-terminated (4×1) surface with very weak 4×4 lines. The supplied Ga corresponds to the As coverage of the As-stabilized GaAs (001) $c(4 \times 4)\alpha$ surface. Thus, most of the Ga adatoms contribute to the formation of a Ga-terminated surface, leaving a relatively low number of Ga adatoms to nucleate and be consumed into the nuclei to form droplets. A change from a streaky pattern to that of a spotty pattern is seen after

crystallization of the droplets, suggesting the formation of three dimensional islands, and weak $\{111\}$ facet patterns from the pyramidal QDs are seen.

SEM image evaluation

An SEM image of the sample is shown in figures 2.12 and 2.13. From these

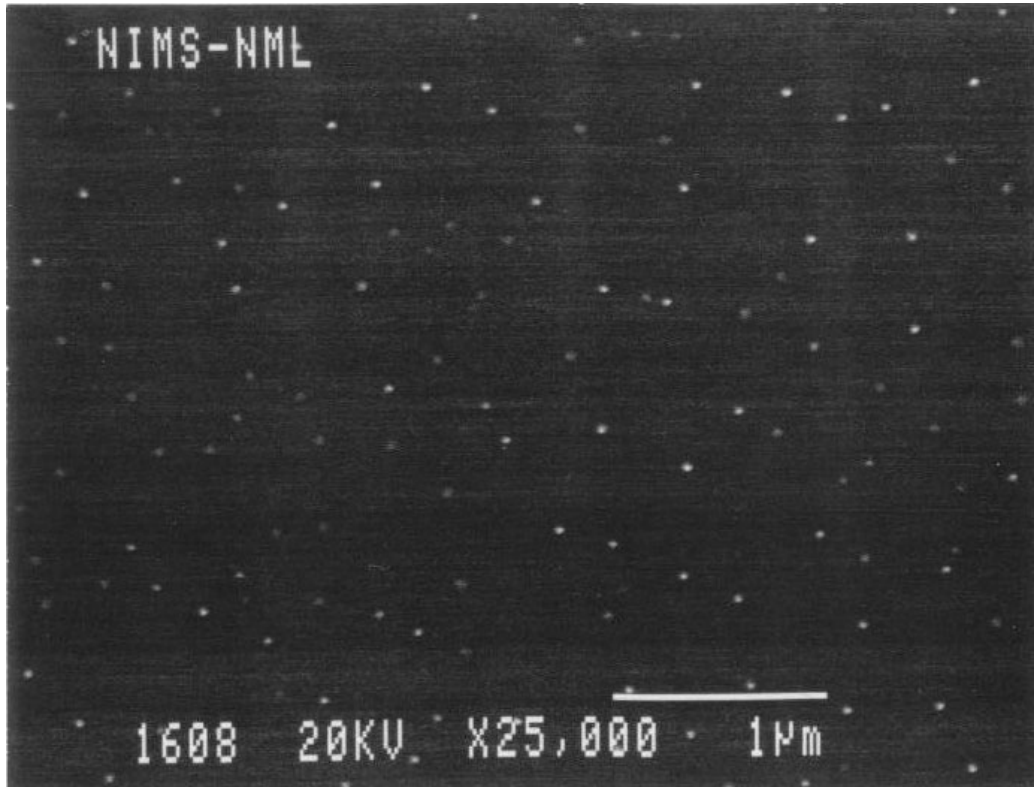


Figure 2.12: SEM image of a low density QD sample without a capping layer

figures it can be determined that the sample has an average QD base size of 40nm and a density of $7 \times 10^8 \text{cm}^{-2}$.

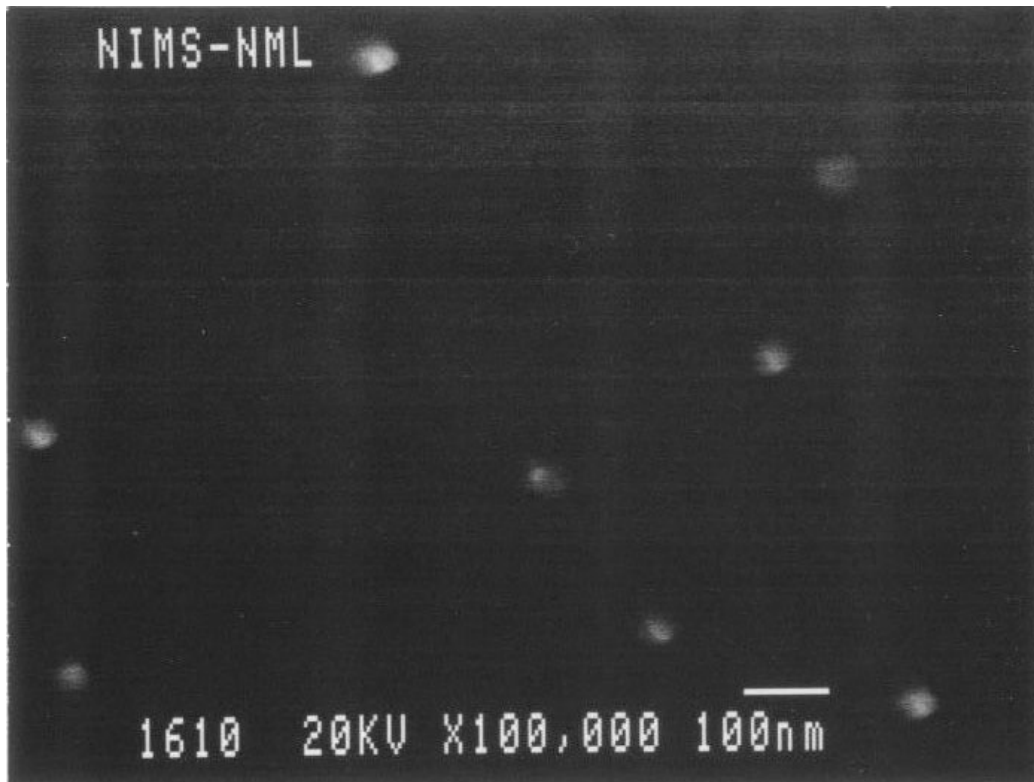


Figure 2.13: SEM image of a low density QD sample without a capping layer

Atomic force microscopy image evaluation

The atomic force microscopy (AFM) three dimensional and cross sectional images of the sample are shown in figures 2.14 and 2.15, and show that the QDs are of a pyramidal shape.

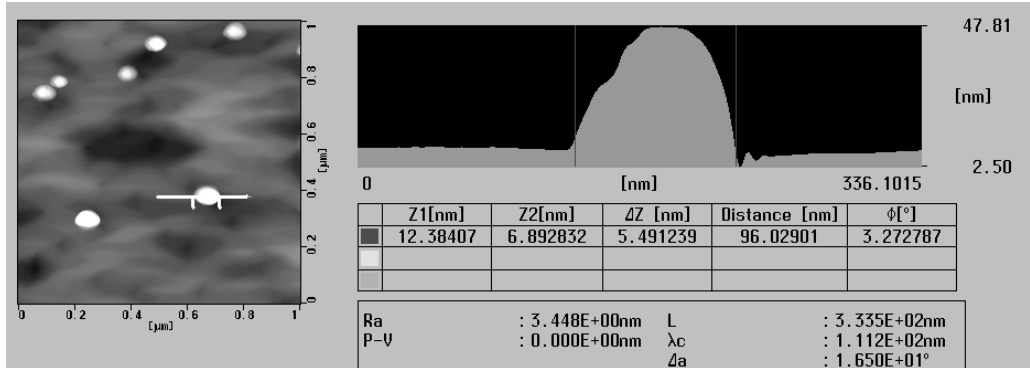


Figure 2.14: AFM image of a low density QD sample without a capping layer ($1\mu\text{m}\times 1\mu\text{m}$)

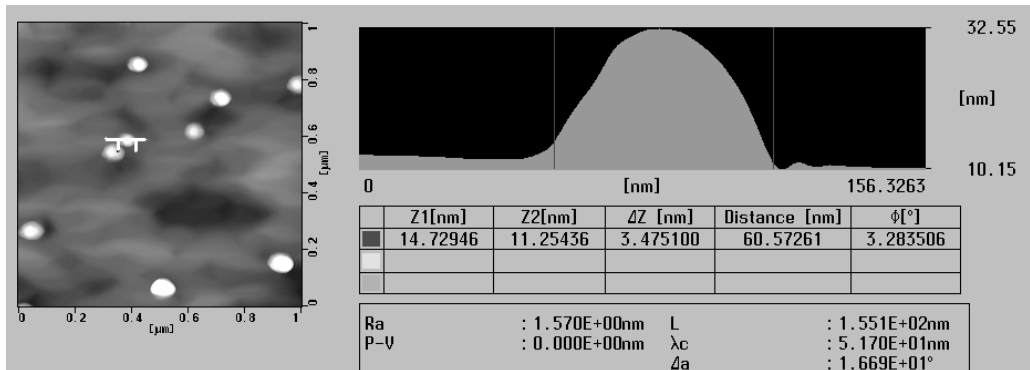


Figure 2.15: AFM image of a low density QD sample without a capping layer ($1\mu\text{m}\times 1\mu\text{m}$)

A distinct characteristic of this sample, one which is of crucial importance in single QD spectroscopy, is that a bimodal growth can be seen. There is a distinct QD size difference in the cross sectional image of the QD in figures 2.14 and 2.15. The QD in figure 2.14 is 40nm high, whereas the QD in figure 2.15 is 20nm high. There is also a distinct difference in the lateral size of the two QDs. The QD density of this sample is $7\times 10^8\text{cm}^{-2}$. When one counts the larger and smaller QDs separately, however, the larger QDs have a density of $4\times 10^8\text{cm}^{-2}$, whereas the smaller QDs have a density of $3\times 10^8\text{cm}^{-2}$. If one

considers the confinement energy to be almost negligible for the larger QDs, and the confinement energy to be much higher for the smaller QDs, then the “confining” QD density is much smaller than the actual QD density. Thus, it can be said that this QD sample with a density of $7 \times 10^8 \text{cm}^{-2}$ in fact has a lower density when considering the carrier confinement capability of the QD. This is a welcome fact in terms of single QD PL measurements.

Another characteristic of this sample is that the QDs tend to be elongated in one direction. It has been reported[12] that QDs tend to grow in the $\langle 110 \rangle$ direction and the QDs tend to be elongated in this direction. This is due to the fact that the $\{111\}A$ facet tends to appear more clearly than the $\{111\}B$ facet, due to the difference in the As supply rate inside the Ga droplet for different crystal axis directions.

2.4.4 GaAs QDs samples with different AlGaAs compositions

Low density samples with different AlGaAs compositions are prepared. Two samples with AlGaAs PL peaks at 1.885eV and 2.102eV at 4K have been made. The corresponding Al concentrations are $x=0.256$ and $x=0.405$, respectively. The energy separation between Γ -, X-, and L- conduction band minima and the top of the valence band versus Al composition is shown in figure 2.16. As can be seen from this figure, both samples' AlGaAs barriers are in the direct bandgap regime.

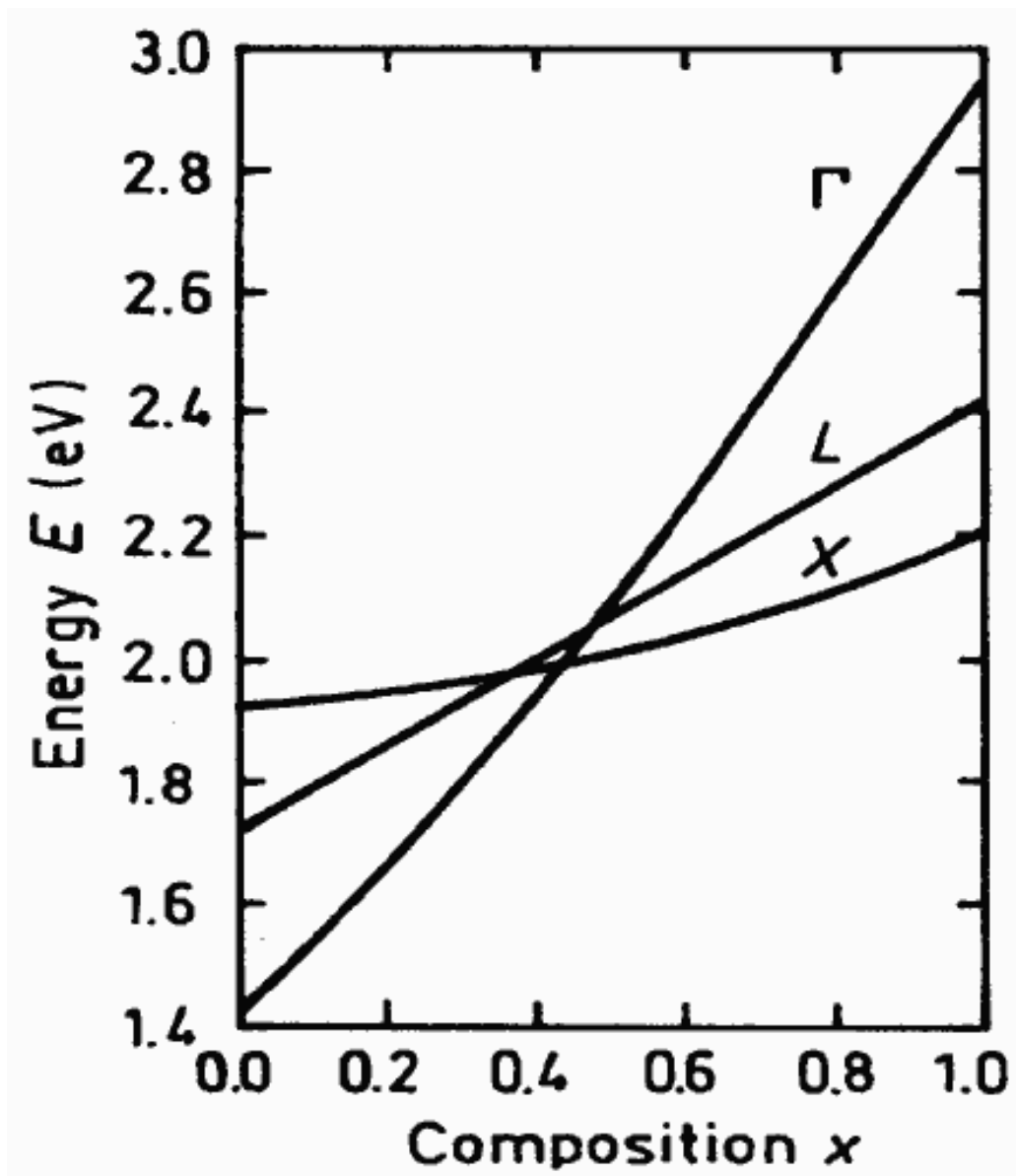


Figure 2.16: Energy separation between Γ -, X-, and L- conduction band minima and the top of the valence band versus composition[18]

2.5 Heterogeneous droplet epitaxy

InGaAs/GaAs QD samples prepared by heterogeneous droplet epitaxy (HDE) are grown by MBE on a GaAs(001) substrate with a 500nm thick GaAs buffer layer. 1.75ML of Ga (for covering the As-terminated surface with Ga to prevent SK mode growth), 2.5ML of In, and 50ML of Ga are supplied to this layer to form In and Ga droplets which are crystallized by an As flux, thus forming the InGaAs-QD/GaAs-barrier layer. The formation of InGaAs QDs occurs at this surface due to the incorporation of Ga atoms into the In droplets, as well as the surface-migration restriction effect of the highly dense Ga droplets. The structure is annealed at various temperatures and overgrown with an 100nm thick GaAs capping layer.

The size of the QDs in the lateral direction is estimated to be around 10nm, and the size of the QDs in the vertical direction is estimated to be around 3.7nm[19]. From cross-sectional TEM images, the shape of the QD is that of a concave disk, and no wetting layer is observed[2]. It is also found that the InGaAs QDs are strongly strained due to the compression by the GaAs capping layer[20]. The bright-field plan-view TEM image of the uncapped sample after the crystallization and the annealing process is shown in figure 2.17. The strong contrast originates from the InGaAs QDs' strain field. The QD density determined from this image is $7 \times 10^9 \text{cm}^{-2}$.

From a comparison of the PL spectra of the InGaAs QDs before and after annealing without the capping layer, only the annealed sample showed PL spectra originating from the QDs. Thus, the annealing process is necessary for the formation of high-quality QDs. The annealing process also results in the enhancement of In segregation due to the phase separation of InAs-GaAs. Samples made with different annealing temperatures are used in this thesis[21]. The annealing temperatures are 325, 400, 450, and 605°C.

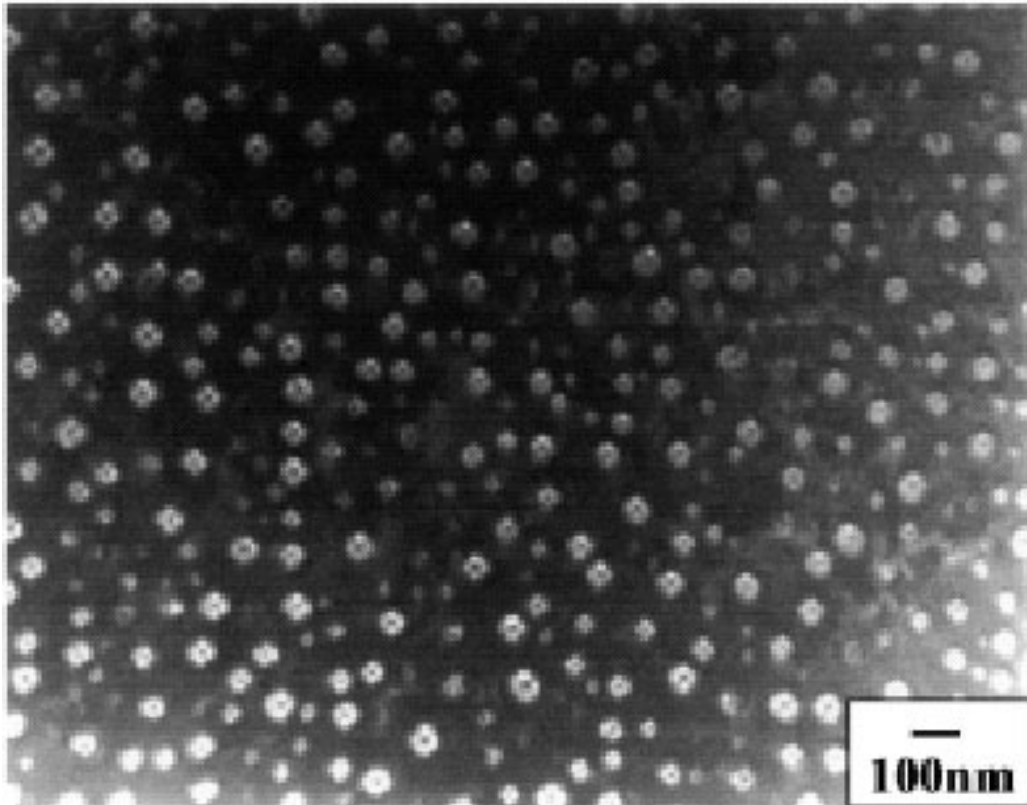


Figure 2.17: Plan-view TEM image of InGaAs QDs after the crystallization and annealing process[1]

Bibliography

- [1] Mano, T., Watanabe, K., Tsukamoto, S., Fujioka, H., Oshima M., Koguchi, N., *New self-organized growth method for InGaAs quantum dots on GaAs(001) using droplet epitaxy*, Jpn. J. Appl. Phys. **38**, L1009 (1999)
- [2] Mano, T., Watanabe, K., Tsukamoto, S., Koguchi, N., Fujioka, H., Oshima, M., Lee, C.-D., Leem, J.-Y., Lee, H. J., Noh, S. K., *Nanoscale InGaAs concave disks fabricated by heterogeneous droplet epitaxy*, Appl. Phys. Lett. **76**, 3543 (2000)
- [3] Mano, T., Watanabe, K., Tsukamoto, S., Fujioka, H., Oshima, M., Koguchi, N., *Fabrication of InGaAs quantum dots on GaAs(001) by droplet epitaxy*, J. Cryst. Growth **209**, 504 (2000)
- [4] Mano, T., Watanabe, K., Tsukamoto, S., Imanaka, Y., Takamasu, T., Fujioka, H., Kido, G., Oshima, M. Koguchi, N., *Fabrication of InGaAs Quantum Dots by SPEED Method and Its Photoluminescence Properties*, J. Surf. Sci. Soc. Jpn. **21**, 107 (2000)
- [5] Gonda, S., *Molecular Beam Epitaxy*, Baifukan Tokyo (1994)
- [6] Sanguinetti, S., Watanabe, K., Kuroda, T., Minami, F., Gotoh, Y., Koguchi, N., *Effects of post-growth annealing on the optical properties of self-assembled GaAs/AlGaAs quantum dots*, J. Cryst. Growth **242**, 321 (2002)
- [7] Crank, J., *The Mathematics of Diffusion*, Clarendon Press Oxford (1955)
- [8] Watanabe, K., Tsukamoto, S., Gotoh, Y., Koguchi, N., *Photoluminescence studies of GaAs quantum dots grown by droplet epitaxy*, J. Cryst. Growth **227**, 1073 (2001)
- [9] Nakajima, K., *The Mechanism of Epitaxial Growth*, Kyoritsu Shuppan Tokyo (2002)

- [10] Goto, Y., *Crystal Growth Handbook*, Kyoritsu Shuppan Tokyo (1995)
- [11] Wagner, R. S., Ellis, W. C., *Vapor-liquid-solid mechanism of single crystal growth*, Appl. Phys. Lett. **4**, 89 (1964)
- [12] Koguchi, N., *Growth of GaAs epitaxial microcrystals by Droplet Epitaxy*, Nihon Kinzoku Gakkai Kaiho **32**, 485 (1993)
- [13] Koguchi, N., Ishige, K., Takahashi, S., *New selective MBE growth method for direct formation of GaAs quantum dots*, J. Vac. Sci. Technol. B **11**, 787 (1993)
- [14] Koguchi, N., Ishige, K., *Growth of GaAs epitaxial microcrystals on an S-terminated GaAs substrate by successive irradiation of Ga and As molecular beams*, Jpn. J. Appl. Phys. **32**, 2052 (1993)
- [15] Watanabe, K., Koguchi, N., Gotoh, Y., *Fabrication of GaAs quantum dots by Modified Droplet Epitaxy*, Jpn. J. Appl. Phys. **39**, L79 (2000)
- [16] Ohtake, A., Nakamura, J., Tsukamoto, S., Koguchi, N., Natori, A., *New structure model for the GaAs(001)-c(4×4) surface*, Phys. Rev. Lett. **89**, 206102 (2002)
- [17] Ohtake, A., Kocán, P., Nakamura, J., Natori, A., Koguchi, N., *Kinetics in surface reconstructions on GaAs(001)*, Phys. Rev. Lett. **92**, 236105 (2004)
- [18] Saxena, A. K., *The conduction band structure and deep levels in Ga_{1-x}Al_xAs alloys from a high-pressure experiment*, J. Phys. C. **13**, 4323 (1980)
- [19] Mano, T., Watanabe, K., Tsukamoto, S., Imanaka, Y., Takamasu, T., Fujioka, H., Kido, G., Oshima, M., Koguchi, N., *Magneto-photoluminescence study of InGaAs quantum dots fabricated by droplet epitaxy*, Physica E **7**, 448 (2000)
- [20] Mano, T., Tsukamoto, S., Koguchi, N., Fujioka, H., Oshima, M., Lee, C.-D., Leem, J.-Y., Lee, H. J., Noh, S. K., , J. Kor. Phys. Soc. **38**, 401 (2001)
- [21] Mano, T., Tsukamoto, S., Koguchi, N., Fujioka, H., Oshima, M., *Indium segregation in the fabrication of InGaAs concave disks by heterogeneous droplet epitaxy*, J. Cryst. Growth **227**, 1069 (2001)

Chapter 3

Resonant Raman spectroscopy of InGaAs QDs

3.1 Introduction

Semiconductor QDs have an unusually large surface-to-volume ratio. As a result, their electronic properties are strongly influenced by the interface between the QD and the matrix in which they are embedded[1]. It is possible to modify this interface by interdiffusion due to the annealing process, as discussed in chapter 2, and thus alter the QD shape and the QD's interaction of the QD-confined excitons with its surroundings. Reported experimental studies suggest that the surface of QDs plays a potentially crucial role in their electronic and optical properties[2]. The polar bond of the material under study leads to the interaction of the LO mode phonon with charge distributions within the crystallite through the Frölich interaction, giving rise to enhanced exciton-LO phonon coupling[3, 4].

In this study, resonant Raman spectroscopy is employed as a method for studying exciton-phonon interactions in QDs. InGaAs/GaAs QDs made by HDE are used, as this QD system has a barrier that is transparent to the QD PL line. Furthermore, QDs made by HDE have no wetting layer, and the QD/barrier interface is well defined. Thus, InGaAs/GaAs QDs made by HDE are a practical choice for this investigation. The InGaAs/GaAs QD samples are annealed at different temperatures, and the effects of QD/barrier interface modification on the exciton-phonon coupling in QDs is observed by resonant Raman spectroscopy.

3.2 Experimental setup

The experimental setup for resonant Raman spectroscopy is shown in figure 3.1. The excitation laser is a Coherent INNOVA300 Ar⁺ laser-pumped Spectra Physics 3900S Ti:sapphire cw laser capable of tuning the laser line from 840 to 1000nm. The laser is focused into a multimode fiber, and the output beam is focused on the sample. The sample is cooled to 5K using a Janis cryostat. The scattered Raman line is collected, collimated, and focused onto the entrance slit of the monochromator. The Raman line is dispersed by a SPEX 1401 750mm double monochromator. The signal is picked up by a Perkin Elmer Optoelectronics SPCM-AQR series single-photon counting module with a silicon avalanche photo diode, and is photon counted by a Stanford Research System SR400 two-channel gated photon counter. The signal from the photon counter is sent to a PC, which also controls the monochromator grating via a NF Wavefactory WF1943A 1ch multifunction synthesizer, which is used here as a pulse generator.

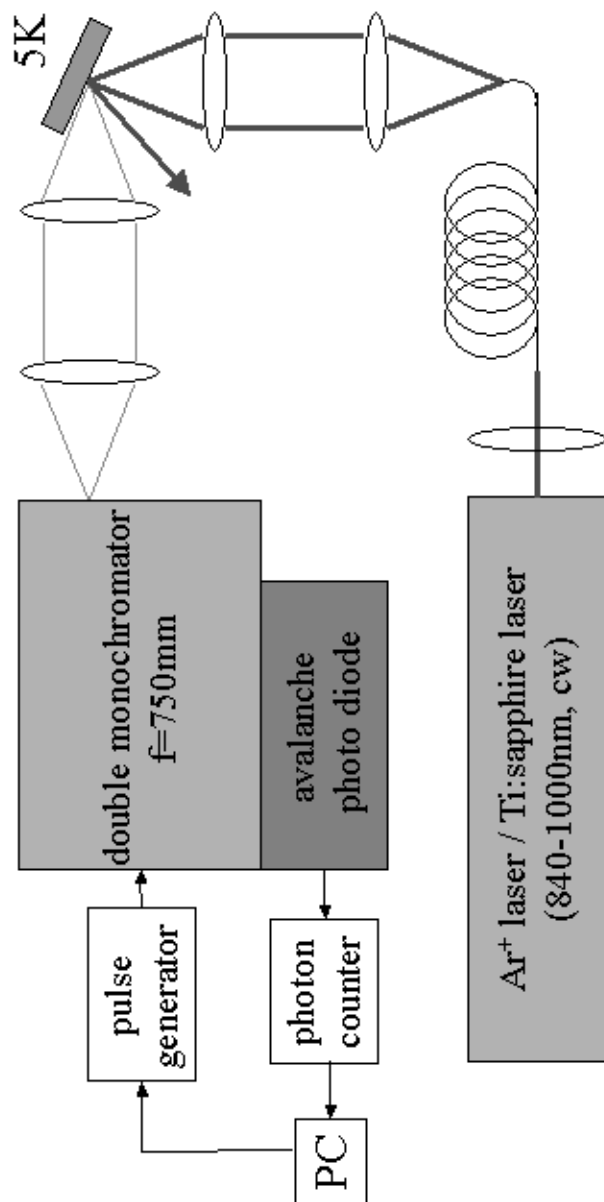


Figure 3.1: Experimental setup for resonant Raman spectroscopy

3.3 Results

3.3.1 PL

As explained in chapter 2, four InGaAs/GaAs QDs samples made by HDE are annealed at 325, 400, 450, and 605°C, and are used for this experiment. The samples will be denoted as sample 2 for the sample annealed at 325°C, sample 4 for the sample annealed at 400°C, sample 5 for the sample annealed at 450°C, and sample 8 for the sample annealed at 605°C. The PL of these QDs at 4K are shown in figure 3.2, along with their relative PL peak intensities in figure 3.3. These data are shown to explain why no resonant Raman signal was attainable from samples 4 and 8; due to their relatively weak PL intensities, their weak Raman signal could not be obtained.

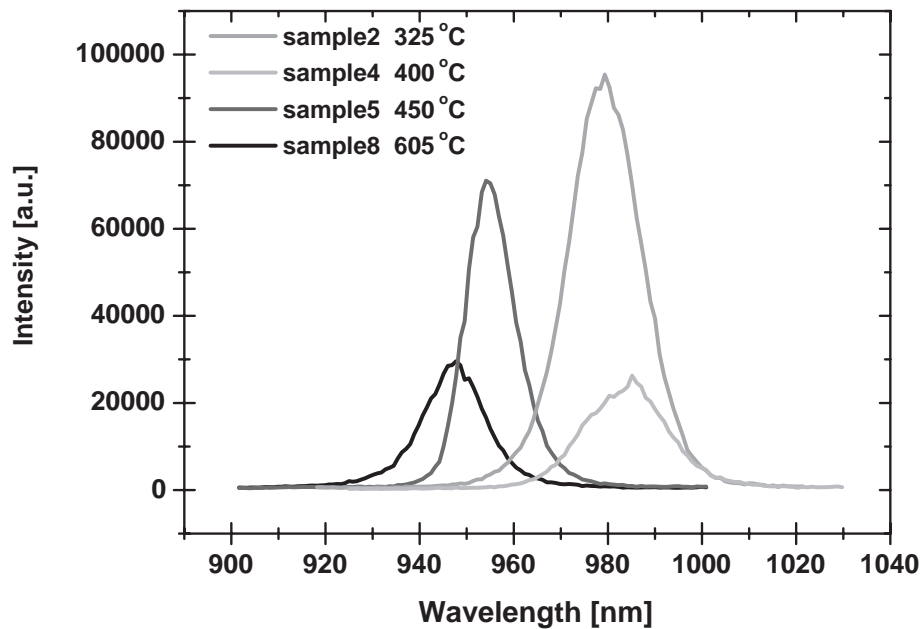


Figure 3.2: PL of InGaAs QD samples taken at 4K

Thus, all resonant Raman spectroscopy data were acquired from samples 2 and 5, indicated by the circled data points in figure 3.3.

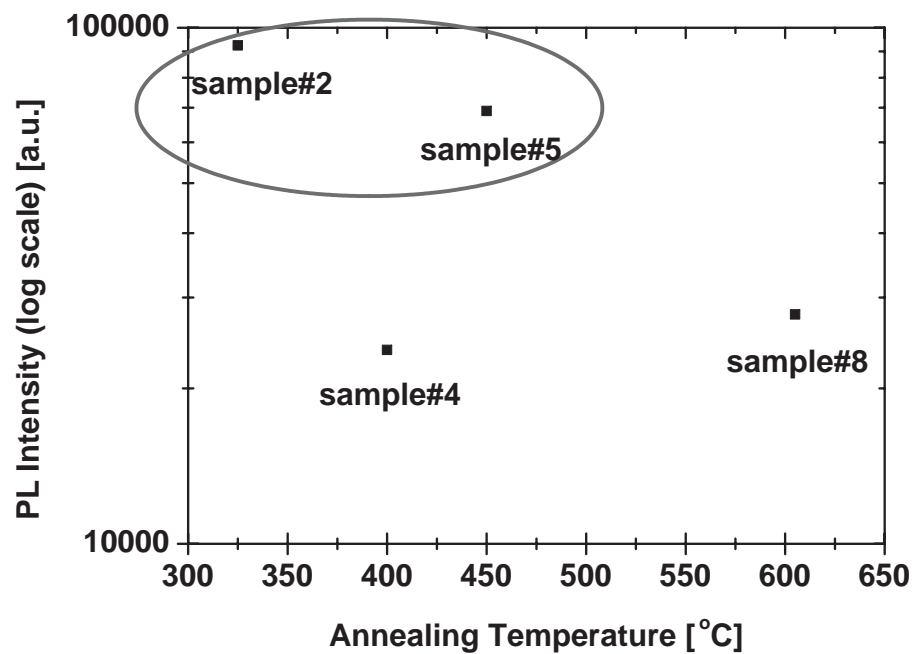


Figure 3.3: Relative PL peak intensities of InGaAs QD samples

3.3.2 Resonant Raman spectra of samples with different annealing temperatures

The resonant Raman spectra of samples 2 and 5 are shown in figure 3.4. Sample 2 was resonantly excited with a wavelength of 970nm at 70mW, and sample 5 was resonantly excited with a wavelength of 950nm at 80mW.

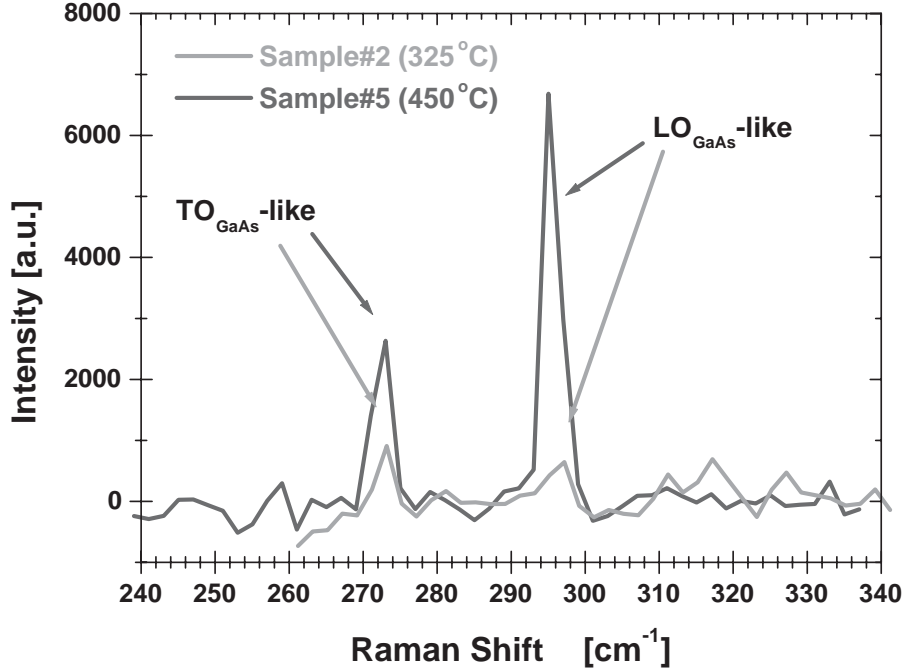


Figure 3.4: Resonant Raman spectra of samples 2 and 5

Both LO_{GaAs} and TO_{GaAs} -like Raman lines can be seen from samples 2 and 5, although the signals are much weaker in sample 2. The observation of TO lines indicate the existence of deformation potential interactions, and the observation of LO lines indicate the existence of Frölich interactions.

In sample 5, exciton coupling to lattice vibrations is increased due to the TO mode interacting with the confined carriers via the internal strain (i.e. the deformation potential); coupling to lattice vibrations is also increase due to the LO mode interacting with charge distributions within the crystallite through the Frölich interaction. In sample 2, these couplings are less pronounced. This is in agreement with the fact that, in sample 2, In segregation

in the QD is more enhanced, whereas in sample 5, InAs and GaAs intermixing is enhanced[5]. Intermixing increases the polar bonds in the QD material. Furthermore, the local strain energy is reduced by intermixing. Sample 5 will be studied in detail to investigate the two types of exciton-phonon interactions at work.

3.3.3 Deformation potential interactions

The resonant and non-resonant Raman spectra of sample 5 are shown in figure 3.5, which confirm that the observations of the phonon lines are due to the phonon interactions with the InGaAs QD-confined excitons, and not due to the non-resonant Raman scattering of the bulk GaAs. The non-resonant Raman spectrum was taken with an excitation wavelength of 990nm at 65mW.

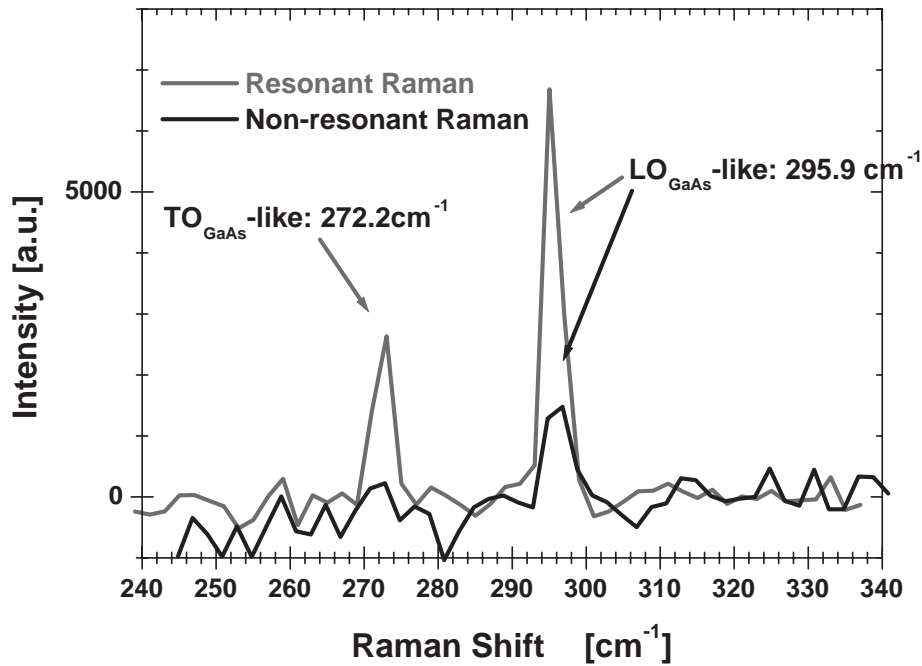


Figure 3.5: Resonant and non-resonant Raman spectra of sample 5

As can be clearly seen, both the TO and LO lines are enhanced when the excitation laser is in resonance with the QD, and are weak when the excitation

laser is not in resonance with the QD. This trend is also observed when the laser line is closer to the bandgap of the bulk GaAs, where, theoretically, the non-resonant Raman lines of the bulk GaAs should be enhanced. The conclusion here is that the Raman spectra from the bulk is relatively weak, and that the TO and LO lines are enhanced only when the laser line is in resonance with the QD band. It should be noted that the TO line is especially enhanced in the resonant Raman spectrum, indicating that the deformation potential interaction plays an important role.

3.3.4 Frölich interactions

In the case of Frölich interaction within the InGaAs QD, the only relevant phonon modes are the LO and the surface (SO) modes. So far, only the LO modes have been identified; a closer examination shows that the SO modes are also present in the resonant Raman spectrum of sample 5. Figure 3.6 shows the resonant Raman spectrum of sample 5, and it can be seen from the Lorentzian peak fits that the spectrum consists of three peaks.

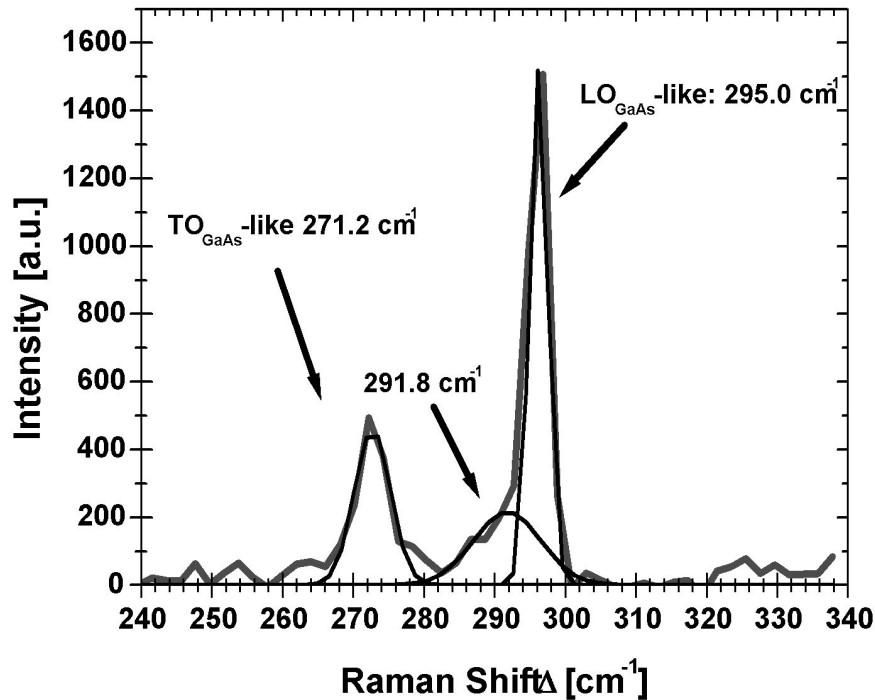


Figure 3.6: Resonant Raman spectra of sample 5

The SO modes can be calculated using the dielectric continuum approach[6, 7, 8]. Here, a system consisting of a single QD with dielectric function $\epsilon_1(\omega)$ embedded in a second material with dielectric function $\epsilon_2(\omega)$ is considered. Each dielectric function is frequency dependent and is assumed to be isotropic and independent of wave vector \vec{k} . Each material is taken to be characterized by dispersionless LO and TO modes, and the dielectric functions are taken to be

$$\epsilon_i(\omega) = \epsilon_{\infty,i} \frac{\omega_{LO,i}^2 - \omega^2}{\omega_{TO,i}^2 - \omega^2}, i = 1, 2, \quad (3.1)$$

where $\epsilon_{\infty,i}$ is the high-frequency relative dielectric constant of each material, and $\omega_{LO,i}$ and $\omega_{TO,i}$ are the wavenumbers of the LO and TO phonons in each material. No net charge resides within either material, so within each material,

$$\vec{\nabla} \cdot \vec{D} = \vec{\nabla} \cdot [\epsilon_i(\omega) \vec{E}] = \epsilon_i(\omega) \vec{\nabla} \cdot \vec{E} \quad (3.2)$$

where \vec{D} is the displacement field, and \vec{E} is the electric field. This gives

$$\epsilon_i(\omega) \vec{\nabla} \cdot \vec{E} = 0 \quad (3.3)$$

in each material. From equation 3.1, it can be seen that the condition $\epsilon_i(\omega) = 0$ describes a bulk LO mode confined in material i with frequency $\omega_{LO,i}$ and that $\epsilon_i(\omega) = \infty$ gives a bulk TO mode confined in material i . To calculate the SO modes, equation 3.1 must be solved for $\epsilon_i(\omega) \neq 0$; thus,

$$\vec{\nabla} \cdot \vec{D} = \vec{\nabla} \cdot \vec{E} = 0. \quad (3.4)$$

for each material. Ignoring retardation effects, \vec{E} can be derived from a scalar potential Φ which satisfies Laplace's equation

$$\nabla^2 \Phi = 0. \quad (3.5)$$

This partial-differential equation is associated with the standard electrostatic boundary conditions imposed at the interface between the media, which are the continuity of the tangential components of \vec{E} and the continuity of the normal component of \vec{D} . The condition that \vec{E} vanish far from the interface specifies a surface mode. The SO modes can be calculated analytically for spherically shaped QDs. For a sphere of radius R , Φ is expressed in spherical coordinates (r, θ, ϕ) as

$$\begin{aligned}\Phi(r, \theta, \phi) &= e^{im\phi} P_l^m(\cos\theta) \times (r/R)^l, r \leq R \\ \Phi(r, \theta, \phi) &= e^{im\phi} P_l^m(\cos\theta) \times (R/r)^{l+1}, r \geq R,\end{aligned}\tag{3.6}$$

where the integers $l(\geq 0)$ and $m(|m| \leq l)$ are SO mode quantum numbers, and P_l^m are associated Legendre polynomials of the first kind. From these equations it can be seen that Φ satisfies Laplace's equation everywhere except at $r = R$, that Φ is everywhere continuous, and that Φ vanishes far from the QD. The only discontinuity in $\nabla\Phi$ occurs at $r = R$ in the direction normal to the dot interface. Continuity of the normal component of $\vec{D} = \epsilon(\omega)\vec{E}$ across the boundary gives the eigenfrequency condition

$$\frac{\epsilon_1(\omega_{lm})}{\epsilon_2(\omega_{lm})} = -1 - \frac{1}{l}.\tag{3.7}$$

By entering equation 3.1 into 3.7, one obtains the SO mode frequencies ω_{lm} .

In order to determine ω_{lm} numerically, the following material values have been used, where material 1 refers to $\text{In}_{0.75}\text{Ga}_{0.25}\text{As}$, and material 2 refers to GaAs.

Table 3.1: Material parameters used for the ω_{lm} calculations[9, 10]

material	ω_{TO} (cm^{-1})	ω_{LO} (cm^{-1})	ϵ_∞
1 ($\text{In}_{0.75}\text{Ga}_{0.25}\text{As}$)	230.6	279.2	11.3
2 (GaAs)	273.3	297.3	10.6

The calculated values for $\omega_{l=2}$ is 293.8 cm^{-1} , and agrees well with the peak value in figure 3.6, which is 291.8 cm^{-1} . The 2 cm^{-1} difference is due to the slightly ellipsoidal shape of the InGaAs QD. Thus it can be said that the peak at 291.8 cm^{-1} in figure 3.6 corresponds to the SO mode.

3.4 Conclusions

The TO, LO, and SO phonon-exciton interactions are observed by resonant Raman spectroscopy of InGaAs QDs made by HDE. The appearance of TO lines indicate the existence of deformation potential interactions between the QD confined exciton and the TO phonon, while the appearance of LO and SO lines indicate the existence of Frölich interactions between the QD confined exciton and the LO and SO phonons.

As intermixing at the QD-barrier interface is increased with increasing annealing temperature, it can be seen that both Frölich and deformation potential interactions are enhanced, judging from the intensities of these

peaks in the resonant Raman spectra of samples with different annealing temperatures. The effect of annealing is more prominently seen in the Frölich interaction, as seen in figure 3.4. It can be seen that interdiffusion enhances the exciton -LO phonon coupling in the QD.

The observation of SO phonon-exciton interactions suggest that the annealed QDs are not perfect spheres because a radial charge distribution in a spherical QD does not couple to surface modes[3]. This coupling between the charge distribution and the surface modes is observed due to the lower symmetry of the shape of the QD, and give rise to issues such as the non-adiabaticity of the exciton-phonon systems[11]. The non-adiabaticity of the exciton-phonon systems is known to play a crucial role in the phonon-assisted optical transitions in a QD[12]. The issue of the change in QD shape symmetry due to annealing will be discussed in the following chapters.

Bibliography

- [1] Nirmal, M, Murray, C. B., Bawendi, M. G., *Fluorescence-line narrowing in CdSe quantum dots: Surface localization of the photogenerated exciton*, Phys. Rev. B **50**, 2293 (1994)
- [2] Bawendi, M. G., Carroll, P. J., Wilson, W. L., Brus, L. E., *Luminescence properties of CdSe quantum crystallites: Resonance between interior and surface localized states*, J. Chem. Phys. **96**, 946 (1992)
- [3] Klein, M. C., Hache, F., Ricard, D., Flytzanis, C., *Size dependence of electron-phonon coupling in semiconductor nanospheres: The case of CdSe*, Phys. Rev. B **42**, 11 123 (1990)
- [4] Nomura, S., Kobayashi, T., *Exciton-LO-phonon couplings in spherical semiconductor microcrystallites*, Phys. Rev. B **45**, 1305 (1992)
- [5] Mano, T., Tsukamoto, S., Koguchi, N., Fujioka, H., Oshima, M., *Indium segregation in the fabrication of InGaAs concave disks by heterogeneous droplet epitaxy*, J. Cryst. Growth **227-228**, 1069 (2001)
- [6] Englman, R., Ruppin, R., *Optical phonons in finite crystals*, Phys. Rev. Lett. **16**, 898 (1966)
- [7] Englman, R., Ruppin, R., *Optical lattice vibrations in finite ionic crystals:I*, J. Phys. C **1**, 614 (1968)
- [8] Knipp, P. A., Reinecke, T. L., *Classical interface modes of quantum dots*, Phys. Rev. B **46**, 10 310 (1992)
- [9] Yu, P. Y., Cardona, M., *Fundamentals of Semiconductors 3rd Edition*, Springer Berlin (2001)
- [10] Ioffe Physico-Technical Institute, *NSM Archive - Physical Properties of Semiconductors*, Ioffe Physico-Technical Institute Electronic Archive <http://www.ioffe.rssi.ru/SVA/NSM/Semicond/index.html>

- [11] Devreese, J. T., *Enhanced probabilities of phonon-assisted optical transitions in semiconductor quantum dots*, 9th Int. Symp. "Nanostructures: Physics and Technology" St. Petersburg, Russia (2001)
- [12] Fomin, V. M., Gladilin, V. N., Devreese, J. T., Pokatilov, E. P., Balaban, S. N., Klimin, S. N., *Photoluminescence of spherical quantum dots*, Phys. Rev. B **57**, 2415 (1998)

Chapter 4

Pressure dependence of GaAs QD PL

4.1 Introduction

The QD PL pressure dependence is a powerful method for studying the band crossover, and thus the band-edge discontinuity, of the GaAs/AlGaAs QD heterojunction. This method utilizes the fact that the semiconductor bandgap changes due to a reduction in the lattice constant caused by pressure application. By measuring the pressure induced bandgap shift by PL, it is possible to reconstruct the heterojunction band structure.

In the case of GaAs/AlGaAs QDs, both materials change from a direct to indirect bandgap under sufficiently high pressure. The energy shift in this case depends on each material's energy band pressure coefficients, with the GaAs and AlGaAs X band and Γ band shifting in opposite directions. At a certain pressure, a band crossover can be observed. By calculating the energy shift required until crossover occurs, the relative band lineups at the heterojunction at ambient pressure are reconstructed.

A schematic representation of the X- Γ band crossover for GaAs/AlGaAs QDs is shown in figure 4.1. The confinement changes from type I to type II at crossover pressure. In type I confinement the electron and hole are confined in the same layer, whereas in type II confinement the electron and holes are confined in separate layers.

Furthermore, the heavy hole energy levels can be resolved after crossover due to the type II recombination. The difference in the QD valence band confinement levels are determined, and are used in effective mass calculations with interdiffusion taken into account.

Application of high hydrostatic pressure to GaAs QDs

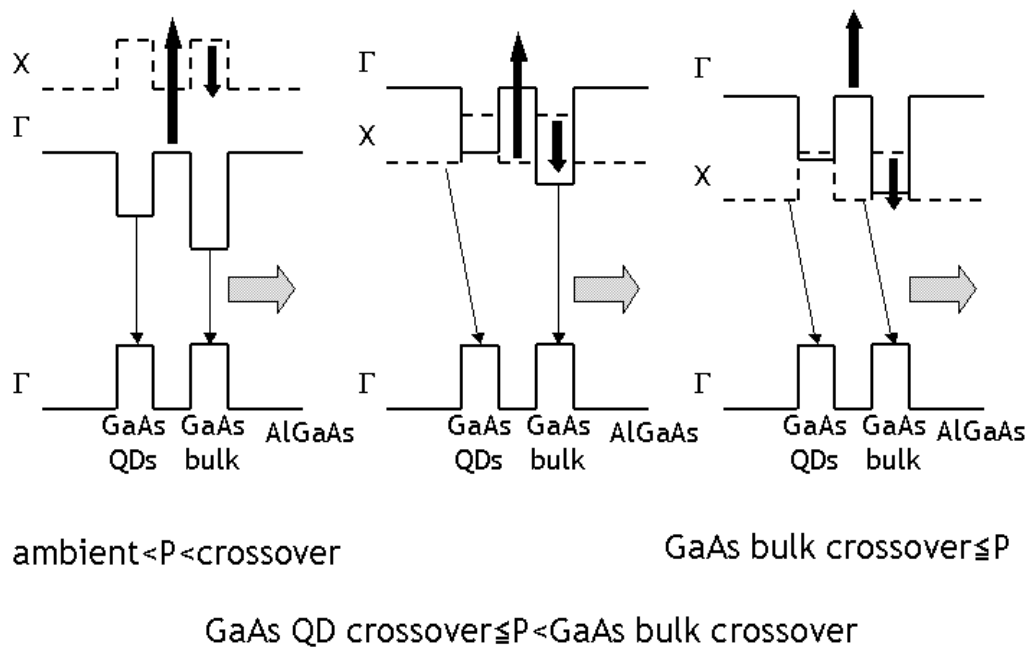


Figure 4.1: A schematic representation of the X- Γ band crossover for GaAs/AlGaAs QDs

4.2 Experimental setup

The use of a diamond anvil cell as a pressure inducing mechanism is suitable for measuring the band crossover due to the hardness of diamond and its transparency at the wavelength range under study. In this experiment, a Merrill-Bassett diamond anvil cell is adopted as a pressure application mechanism, which is small enough to fit inside a glass cryostat. A schematic representation of a Merrill-Bassett diamond anvil cell is shown in figure 4.2. The applied pressure is adjusted by directly pushing together two plates, each with a diamond attached, via screws which connect the two plates. The diamonds are attached to the plates using an epoxy-type adhesive, which will insure their adhesion at low temperature. An inconel gasket with a $300\mu\text{m}$ hole contains an 1:4 ethanol-methanol compound solution which serves as the hydrostatic pressure transmitting medium; the sample is put into the hole with the solution, and is sandwiched between the two diamonds' flat facets. This compound solution is known to be hydrostatic up to 200kbar at room temperature, mostly nonaxial, and is often used in low temperature measurements. Pressure adjustment is done hydrostatically at room temperature. Due to the small sample space available, as well as the shrinkage of the sample space upon pressure application, the sample must be mechanically and chemically etched to a foil-like thickness.

The pressure is usually calibrated by monitoring the shift of the PL of ruby chips encased in the Merrill-Bassett diamond anvil cell along with the sample. However, the ruby chips' PL spectrum line coincides with that of the GaAs QDs'; thus the bulk AlGaAs and GaAs PL spectral line shift is used to calibrate the pressure.

The cell is directly immersed in liquid helium to obtain data at 4.2 K. A frequency-doubled YAG cw laser (532 nm, 20 mW) is used as an excitation light source and the PL spectra are observed using an Acton SpectraPro-300i 30cm spectrometer with a 600 g/mm grating and a liquid nitrogen-cooled CCD detector, as shown in figure 4.3.

The sample under investigation is different from those made by the conditions described in chapter 2. The sample contains GaAs QDs in a AlGaAs barrier, and are made by MDE. The main differences between this sample and the samples described in chapter 2 are the QD density and the barrier material composition. In this experiment, a high density QD sample is desired, in order to achieve higher PL signal intensity. Signal intensity is known to decrease after crossover occurs and the carrier confinement becomes type II. Thus, a sample with an average QD base size of 15nm and a density of $1.2 \times 10^{10} \text{cm}^{-2}$ is used. The PL of this sample at 3K has a QD PL peak centered at 1.721eV. The Al concentration x of the $\text{Al}_x\text{Ga}_{1-x}\text{As}$ barrier layer is

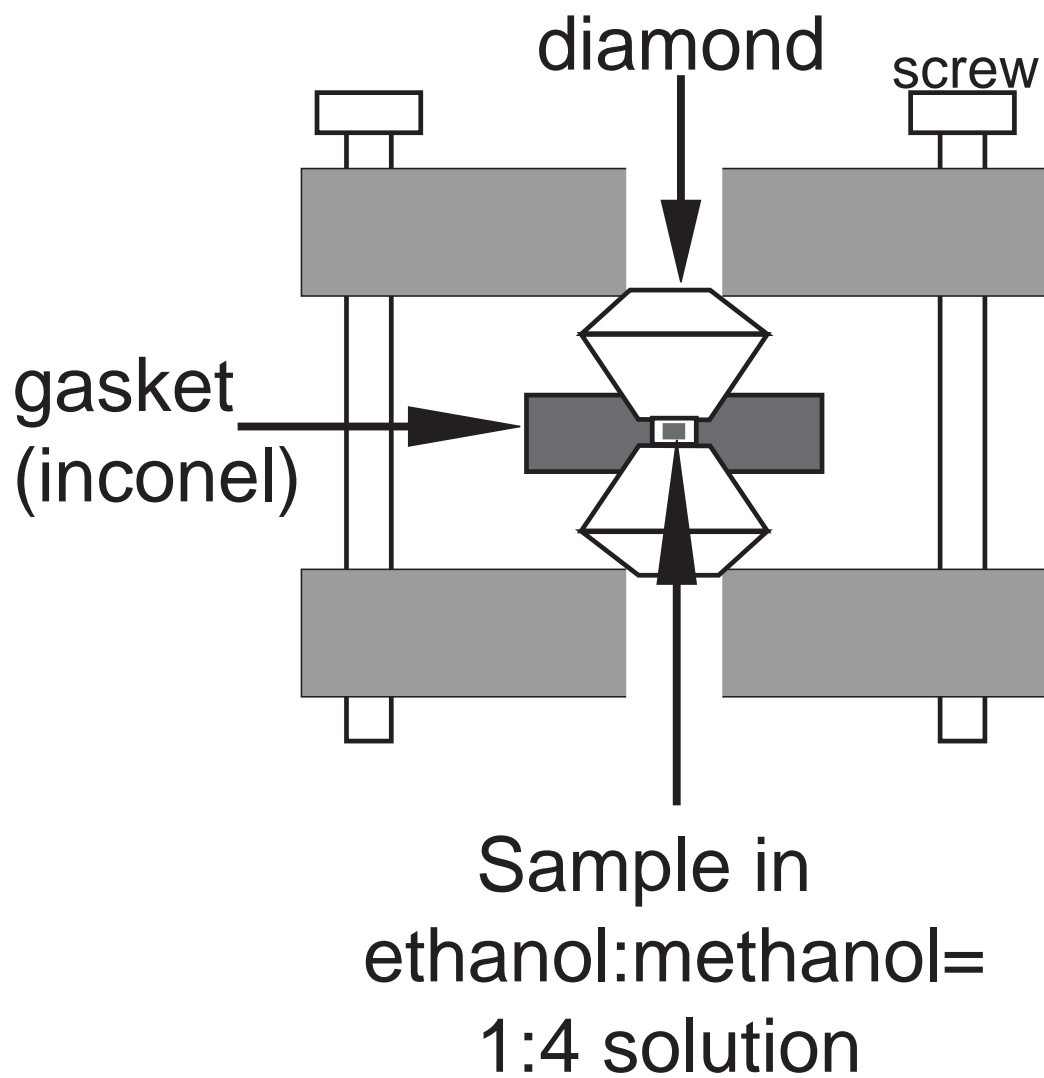


Figure 4.2: A schematic representation of a Merrill-Basset diamond anvil cell

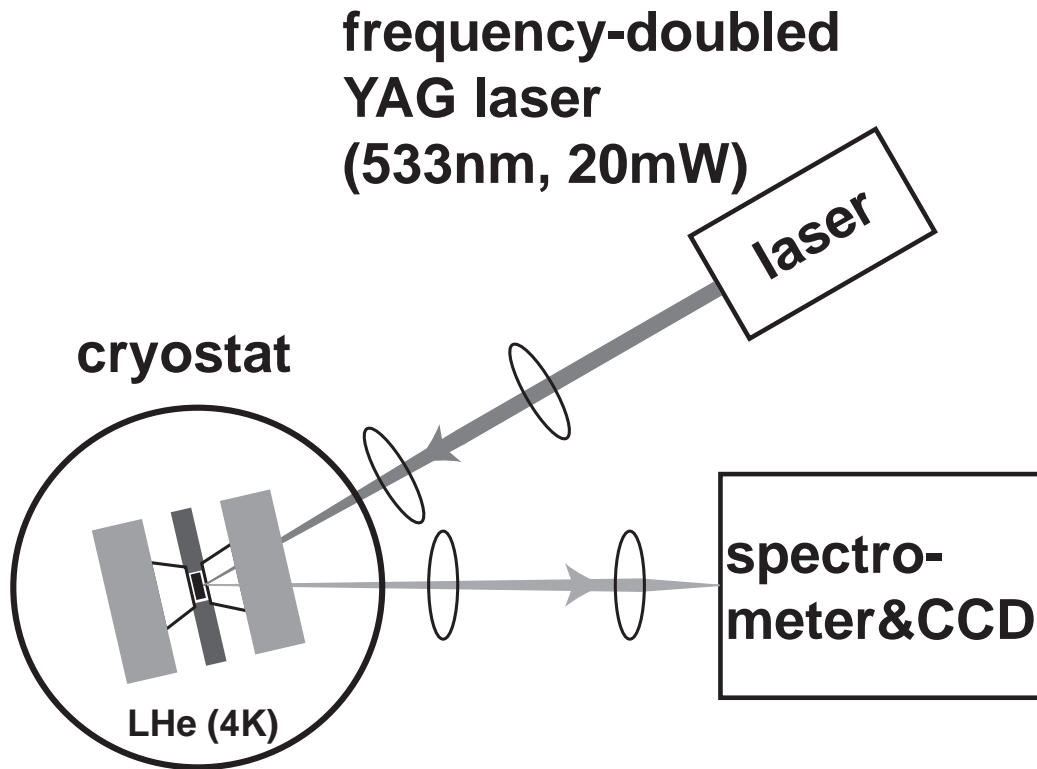


Figure 4.3: Experimental setup of the QD PL pressure dependence measurement

determined to be $x=0.31$.

4.3 Results

The shift in the PL peak energies with pressure for bulk GaAs, AlGaAs, and GaAs QDs are shown in figure 4.4. The dotted lines are linear fits to the data. The solid lines are linear fits to the data with the exciton binding energy considered. The split QD peak after crossover is expressed by the open and closed squares. All peaks shift to higher energies, with the bulk GaAs and GaAs QD peaks shifting back to lower energies, beyond a certain pressure, where the Γ -X conduction band crossover is considered to occur. The AlGaAs emission becomes too weak to detect after 7.8 kbar, reflecting a change to an indirect recombination emission. This pressure is regarded as the band crossover pressure for AlGaAs and the pressure coefficient is 12.2 meV/kbar. This value is comparable to the reported pressure coefficient for $\text{Al}_{0.3}\text{Ga}_{0.7}\text{As}$, which is 9.5 meV/kbar[1]. The energies of the bulk GaAs and GaAs QD peaks deviate from a linear pressure dependence near the band crossover. This is due to several effects, including the change in exciton binding energy at high pressure and the direct/indirect recombination emission spectra overlap of the inhomogeneously broadened QD PL peak.

The pressure dependence of the exciton binding energy for bulk GaAs is given as $d\ln(\mathcal{R}/\mathcal{R}')/dP=0.0083(/\text{kbar})$, where the bulk GaAs exciton binding energy at ambient pressure is $\mathcal{R}'=4.2\text{meV}$ [2, 3]. The exciton binding energy for GaAs and GaAs QDs before and after the band crossover can be derived using a hydrogenic model as given by

$$\mathcal{R} = \frac{e^4\mu}{2\hbar^2\varepsilon^2}. \quad (4.1)$$

Here e is the electronic charge, \hbar is Plank's constant over 2π , ε is the electric permittivity and μ is the reduced mass given by

$$\mu = \frac{1}{m_e^*} + \frac{1}{m_h^*}. \quad (4.2)$$

Here, only the reduced mass of the electron m_e^* and heavy hole m_h^* is considered, because of the non-degeneracy of the valence band in the case of quantum dots. Application of this model to QDs has been reported by Li[4]. ε and μ are used as parameters to calculate the exciton binding energy. Assuming the bulk GaAs crossover occurs at 30 kbar, and the GaAs QDs crossover occurs at 20 kbar, the exciton binding energy is found to be 5.4 meV for bulk GaAs before crossover, 18.3 meV for bulk GaAs after crossover, 5.3 meV for

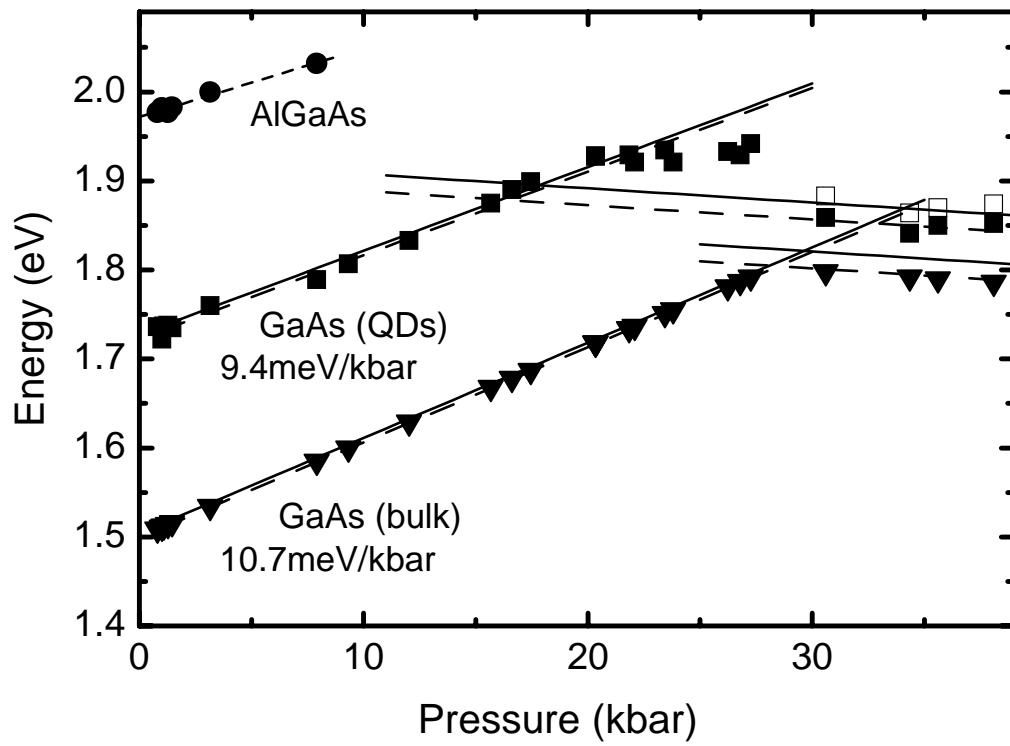


Figure 4.4: Pressure dependence of the QD PL spectrum

GaAs QDs before crossover and 19.7 meV for GaAs QDs after crossover. Taking these binding energies into account, the energy gap derived from the emission spectra energy is shown as the solid lines in figure 4.4. From this, the actual crossover pressure for bulk GaAs is found to be 30.0 kbar, and for GaAs QDs, 18.3 kbar. The pressure coefficient is found to be 10.7 meV/kbar for bulk GaAs and 9.4 meV/kbar for GaAs QDs. The bulk GaAs pressure coefficient is in good agreement with the reported value of 10.6 meV[5]. After the band crossover, the pressure coefficient of the AlGaAs X conduction band is found to be -1.6 meV/kbar, which is also in good agreement with the reported value of -1.7 meV/kbar[1].

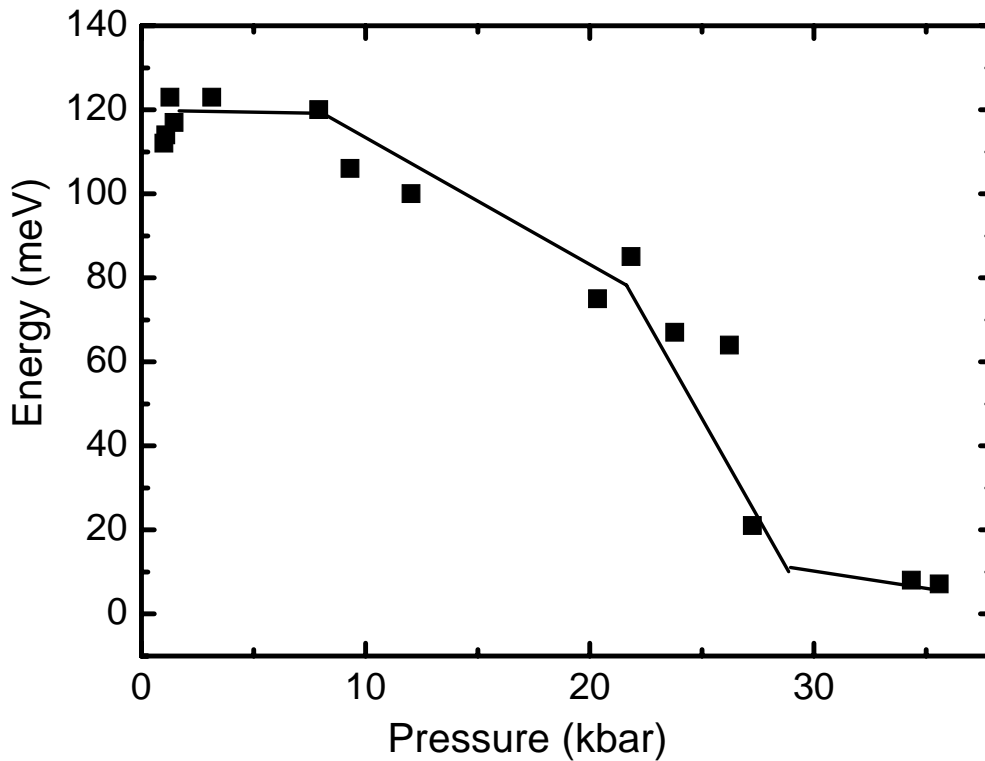


Figure 4.5: Pressure dependence of the QD PL spectrum FWHM (the line is a guide to the eye)

Figure 4.5 shows the pressure dependence of the QD PL spectrum FWHM. A drop in FWHM can be seen near the crossover pressure, accompanied by a marked drop in emission intensity. The 10 % difference in the pressure coefficient for bulk GaAs and GaAs QDs, as well as the drop in FWHM and emission intensity can be explained by the size distribution of the QDs; the smaller QDs at the higher energy side of the peak have a smaller pressure

coefficient than the larger QDs, which have a pressure coefficient closer to that of bulk GaAs. A similar structure dependence of pressure coefficient has been reported for superlattices[6]. Near the crossover pressure, as more GaAs QD Γ conduction bands and the AlGaAs X conduction band cross over with pressure, the number of QDs contributing to the indirect recombination emission increases. After the band crossover, the GaAs QD PL spectrum FWHM changes from that of an inhomogeneously broadened peak to that of the sharp excitonic spectrum of an AlGaAs X conduction band electron to QD Γ valence band recombination. This type II recombination emission has a long radiative lifetime, and consequently has a low luminescent efficiency. This is supported by the results of time-resolved PL measurements taken at 3kbar and 20kbar. At 3kbar, an emission with a lifetime of 358 ps can be observed, while at 20kbar, the emission decay time exceeds the upper limits of the streak camera. This is due to the weak emission intensity as well as the long relaxation time of an indirect recombination emission. At pressures higher than the GaAs QDs crossover, the GaAs QD peak splits into two peaks with the same pressure constant. The energy separation between these two peaks is 24 meV. This is considered to be the recombination emission of AlGaAs electrons with a GaAs QD heavy-hole ground state and the first excited state.

4.4 Conclusions

4.4.1 Determination of the QD band lineup

The band offset can be determined by the following model. When the measured photon energy is $E_{PL}(P)$, the exciton binding energy is $E_{bind}(e-h)$, and the bandgap is $E_g(P)$, the observed PL is related to the bandgap by

$$E_{PL}(P) = E_g(P) - E_{bind}(e - h). \quad (4.3)$$

The total energy shift until crossover, ΔE_{shift} , can be determined experimentally by the crossover pressure P_c as

$$\Delta E_{shift} = \frac{dE_{\Gamma}^{cond}}{dP} \times (P_c - 1) - \frac{dE_X^{cond}}{dP} \times (P_c - 1), \quad (4.4)$$

where E_{Γ}^{cond} and E_X^{cond} denote the conduction band energy at the Γ point and X point of the Brillouin zone, respectively. Furthermore, when $E_g^{QD}(P)$ is the bandgap of the QD at pressure P , $E_g^{barr}(P)$ is the bandgap of the barrier at pressure P , ΔE_C is the conduction band offset, ΔE_V is the valence band

offset, and $\Delta[E^{barr,cond}(X - \Gamma)]$ is the energy difference between the barrier conduction band at the X point and Γ point, the following relations hold.

$$E_g^{barr}(P) - E_g^{QD}(P) - \Delta E_C = \Delta E_V, \quad (4.5)$$

$$\Delta[E^{barr,cond}(X - \Gamma)] + \Delta E_V = \Delta E_{shift}. \quad (4.6)$$

From the experimentally determinable values $E_g^{barr}(P)$, $E_g^{QD}(P)$, $E_g^{barr}(P_c)$, $E_g^{barr}(P_c)$, the energy shift until crossover (P_c), and $\Delta[E^{barr,cond}(X - \Gamma)]$, the valence band offset can be determined as

$$\Delta E_V = \frac{dE_\Gamma^{cond}}{dP} \times (P_c - 1) - \frac{dE_X^{cond}}{dP} \times (P_c - 1) - \Delta[E^{barr,cond}(X - \Gamma)]. \quad (4.7)$$

From equation 4.5, the conduction band offset can be determined as follows

$$\Delta E_C = E_g^{barr}(P) - E_g^{QD}(P) - \Delta E_V. \quad (4.8)$$

From the pressure coefficients of AlGaAs, bulk GaAs and GaAs QDs, the energy shift necessary for the band crossover for bulk GaAs and GaAs QDs can be calculated. This gives the GaAs QDs conduction-band ground state confinement energy $\Delta E_e^{n=1,l=0}$ and valence-band ground state confinement energy for heavy holes $\Delta E_h^{n=1,l=0}$ at ambient pressure. The GaAs QDs' valence-band excited state confinement energy for heavy holes $\Delta E_h^{n=2,l=0}$ at ambient pressure is given by the energy separation between the two GaAs QDs peaks after crossover. Using the AlGaAs Γ - X conduction-band energy difference, the GaAs QDs conduction- and valence-band offsets ΔE_C and ΔE_V at ambient pressure can also be determined. The reconstructed band lineups of the GaAs QDs are shown in figure 4.6.

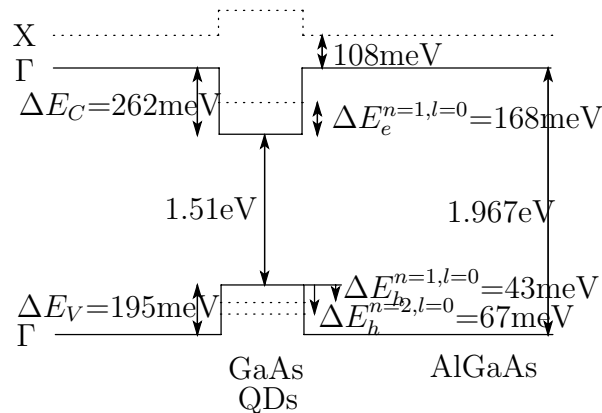


Figure 4.6: Reconstructed band lineups of the GaAs QDs

From the band lineup, it is possible to determine ΔE_V and ΔE_C for any GaAs/AlGaAs QD sample with different Al concentrations using Dingle's method[7], whereupon the conduction-band discontinuity Q factor is defined as being equal to the ratio between ΔE_C and the bandgap difference ΔE_g as a way to characterize the band offset.

$$Q = \frac{\Delta E_C}{\Delta E_g}. \quad (4.9)$$

From this relation, the Q factor for GaAs/AlGaAs QDs is determined to be 0.57, which is equal to the reported value of 0.57[8]. This Q factor will be used in the next chapter to determine the band offsets for GaAs QDs with different barrier bandgaps.

4.4.2 Effective mass approximation calculations of the energy levels

The calculation of the transition energies for GaAs/AlGaAs QD systems with band offsets as described above is performed numerically within the effective mass approximation, using the method outlined in reference [9]. The numerical approach to the problem is to enclose the cluster inside a cylinder of radius R and height Z_c on the surface of which the wave functions are forced to vanish. The QD potential is treated as a perturbation. A schematic diagram as well as the dimensions of the analysis space is shown in figure 4.7. The typically pyramidal QD shape has been approximated, for computational purposes, by a cone shape. A QD base size of $\approx 20\text{nm}$ and a height of $\approx 16\text{nm}$ are considered in this calculation, from the HRSEM microscopic analysis of the QDs[10]. Taking into account the commutation of H and $\partial/\partial\theta$ the eigenfunctions of equation

$$H_{e(h)} = E_{ce(h)}^z + E_{ce(h)}^{r,\theta} + V_{e(h)}(z, r) \quad (4.10)$$

where

$$E_{ce(h)}^z = -\frac{\hbar^2}{2} \left(\frac{\partial}{\partial z} \frac{1}{m_{e(h)}^z(r, z)} \frac{\partial}{\partial z} \right) \quad (4.11)$$

$$E_{ce(h)}^r = -\frac{\hbar^2}{2} \left(\frac{1}{r} \frac{\partial}{\partial r} \frac{r}{m_{e(h)}^r(r, z)} \frac{\partial}{\partial r} \right) - \frac{\hbar^2}{2} \left(\frac{1}{r^2 m_{e(h)}^r(r, z)} \frac{\partial^2}{\partial \theta^2} \right). \quad (4.12)$$

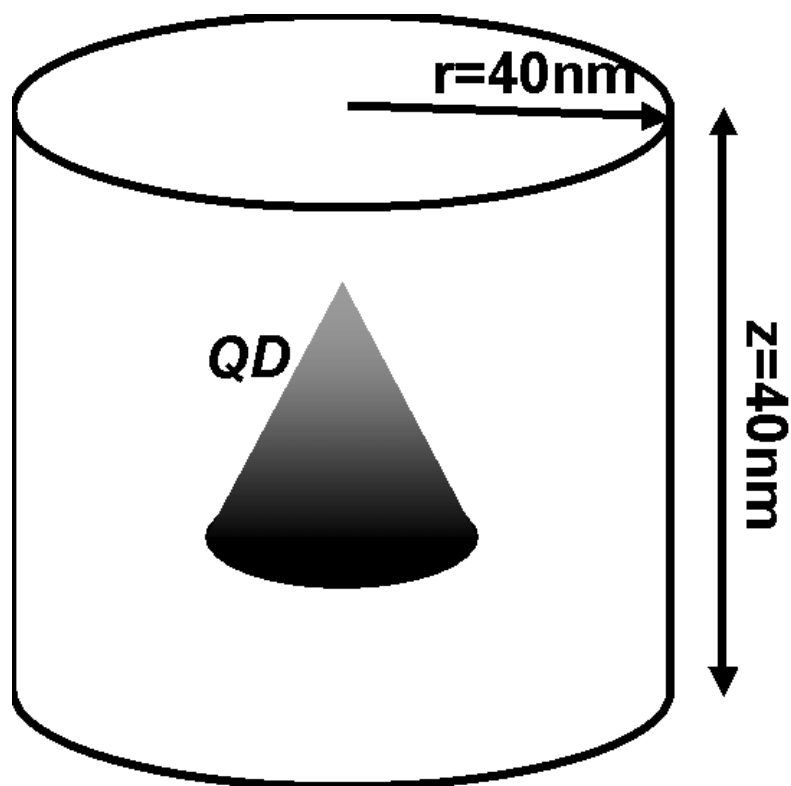


Figure 4.7: Schematic diagram of the analysis space

Eigenvectors satisfying these boundary conditions can be decomposed on the basis formed by products of Bessel functions of integer order n and by sine functions of z of the form

$$\chi_l(r, z, \theta) = \sum_{n>0, m>0} A_{n,m}^l \xi_{n,m}^l(r, z, \theta) \quad (4.13)$$

$$\xi_{n,m}^l(r, z, \theta) = \beta_n^l J_l(k_n^l r) e^{il\theta} \sin(K_m z), \quad (4.14)$$

where $k_n^l R$ is the n th zero of the Bessel function of integer order $J_l(x)$, and $K_m = \pi m/Zc$ and β_n^l is a normalization factor. In the actual numerical calculations, 20 Bessel and sine functions are used.

$m_{e(h)}^z(z, r)$ and $m_{e(h)}^r(z, r)$ are the electron (hole) effective masses for the motion along z and in the layer planes, both depending on r and z if they are taken to be different in different materials. It is assumed that the inverse masses and potential $V_{e(h)}$ vary linearly with the Al concentration.

When interdiffusion of Al is considered in the calculation, the spatial distribution of the Al concentration for interdiffusion length l , as calculated in chapter 2, is used, instead of the cone-shaped, step-function like Al concentration distribution shown in figure 4.7.

The cylindrical symmetry used in this calculation is justified when $l \neq 0$, i.e. when the actual QD shape is no longer pyramidal, because the isotropically annealed QD becomes more rounded in shape, as described in chapter 2.

Material parameters are given in table 4.1.

Table 4.1: Material parameters used for the effective mass calculations[10]

	band mismatch (eV)	$m_{r,z}^{GaAs}(m_0)$	$m_{r,z}^{AlGaAs}(m_0)$
electrons	-0.262	0.067	0.093
holes	-0.195	0.51	0.57

The ground-to-excited state transition energy separation E1, as well as the ground-to-excited hole state transition energy separation E2, as depicted in figure 4.8, are calculated for different interdiffusion lengths l . E1 and E2 are plotted as a function of l in figure 4.9, and show the induced changes in the QD transition energy caused by the modification in the confining potential.

E2, or the $n=1, l=0$ electron- $n=1, l=0$ heavy hole and $n=1, l=0$ electron- $n=2, l=0$ heavy hole transition energy difference, was determined to be 24meV from the high pressure GaAs QD PL experiments. As the line drawn at $E2=24\text{meV}$ in figure 4.9 shows, the light-colored curve showing the l -E2 relation coincides with $E2=24\text{meV}$ at $l=1.0\text{nm}$ and 2.5nm . When $l=1.0\text{nm}$, the E1 transition is calculated to be 87meV, whereas when $l=2.5\text{nm}$, the E1 transition is calculated to be 72meV. Thus, the E1 transition is expected to be near these values.

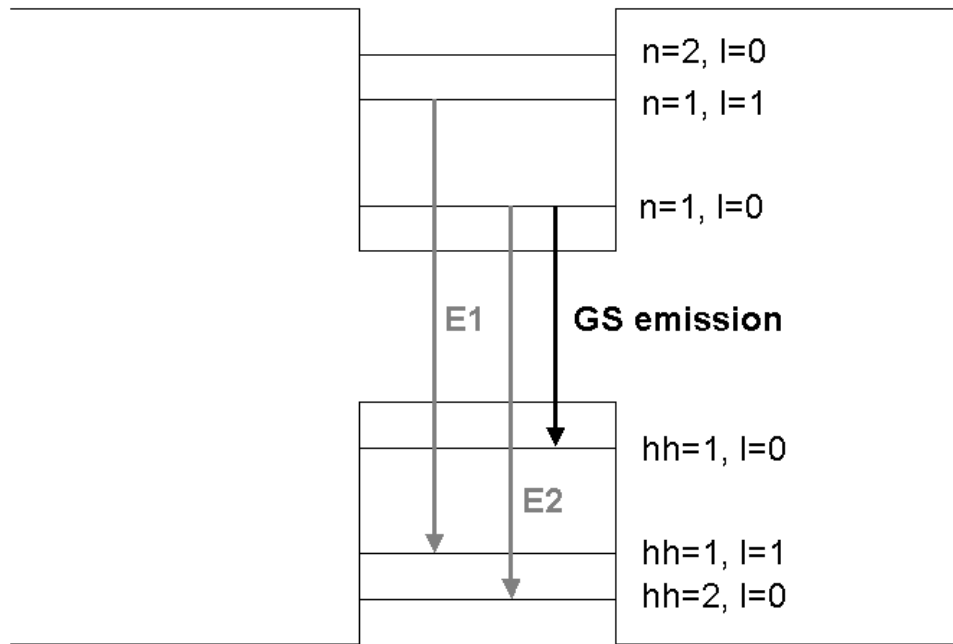


Figure 4.8: Schematic diagram of various optical transitions

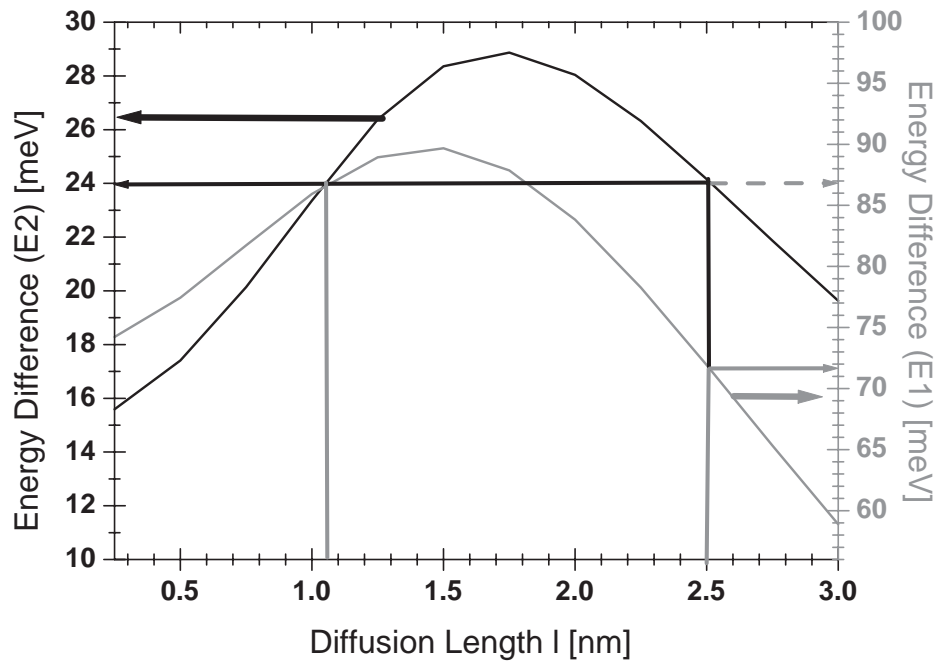


Figure 4.9: E1 and E2 as a function of l

The E2 transition discussed here is normally dipole forbidden, and should not be optically active. In the special case of an indirect recombination, as in the type II recombination after crossover, the energy levels of the holes can be optically observed. In the next chapter, single QD spectroscopy is selected as a method to determine the various optically observable energy levels, as well as the renormalization of the energy levels due to many body effects, and the observation of E2 transitions at ambient pressure due to many body effects will be discussed.

Bibliography

- [1] Roach, W. P., Chandrasekhar M., Chandrasekhar, H. R., Chambers, F. A., *Electronic transitions in bulk $Al_{0.3}Ga_{0.7}As$ under hydrostatic pressure*, Phys. Rev. B **44**, 13404 (1991)
- [2] Goñi, A. R., Cantarero, A., Syassen, K., Cardona, M., *Effect of pressure on the low-temperature exciton absorption in GaAs*, Phys. Rev. B **41**, 10111 (1990)
- [3] Goñi, A. R., Cantarero, A., Schwarz, U., Syassen, K., Chevy, A., *Low-temperature exciton absorption in InSe under pressure*, Phys. Rev. B **45**, 4221 (1992)
- [4] Li, G. H., Goñi, A. R., Syassen, K., Brandt, O., Ploog, K., *State mixing in InAs/GaAs quantum dots at the pressure-induced Γ -X crossing*, Phys. Rev. B **50**, 18420 (1994)
- [5] Phillips, J., Bhattacharya, P., Venkateswaran, U., *Pressure-induced energy level crossings and narrowing of photoluminescence linewidth in self-assembled InAlAs/AlGaAs quantum dots*, Appl. Phys. Lett. **74**, 1549 (1999)
- [6] Lambkin, J. D., Adams, A. R., Dunstan, D. J., Dawson, P., Foxon, C. T., *Pressure dependence of the valence-band discontinuity in GaAs/AlAs and GaAs/ $Al_xGa_{1-x}As$ quantum-well structures*, Phys. Rev. B **39**, 5546 (1989)
- [7] Dingle, R., Wiegmann, W., Henry, C. H., *Quantum states of confined carriers in very thin $Al_xGa_{1-x}As$ -GaAs- $Al_xGa_{1-x}As$ heterostructures*, Phys. Rev. Lett. **33**, 827 (1974)
- [8] Miller, R. C., Kleinman, D. A., Gossard, A. C., *Energy-gap discontinuities and effective masses for GaAs- $Al_xGa_{1-x}As$ quantum wells*, Phys. Rev. B **29**, 7085 (1984)

- [9] Marzin, J.-Y., Bastard, G., *Calculation of the energy levels in InAs/GaAs quantum dots*, Solid State. Commun. **92**, 437 (1994)
- [10] Sanguinetti, S., Watanabe, K., Kuroda, T., Minami, F., Gotoh, Y., Koguchi, N., *Effects of post-growth annealing on the optical properties of self-assembled GaAs/AlGaAs quantum dots*, J. Cryst. Growth **242**, 321 (2002)

Chapter 5

Single GaAs QD micro-PL spectroscopy

5.1 Introduction

Due to the distribution of different-sized QDs with slightly different confinement energies, many of these QDs' sharp PL peaks overlap slightly and form a much broader band whose width is known as the inhomogeneous linewidth. Thus, single or few QD spectroscopy is needed to resolve the sharp spectral lines of single QDs to gather information hidden by the inhomogeneous linewidth. Furthermore, single QD spectroscopy is necessary to assign the various spectral lines to the energy levels and carrier correlation within the QD. Also, multi-excitonic features such as Coulomb and exchange interactions are resolved in single QD spectroscopy. Due to the diffraction limit of light (approximately $\lambda/2$) and the high density of QDs, single QD spectroscopy is difficult. These challenges are overcome by combining high spatial resolution spectroscopy (micro-PL) with a method for the reduction of the number of excited and/or observed QDs.

Many methods for single zero-dimensional structure spectroscopy have been proposed, using mesa structure fabrication[1, 2, 3, 4], metallic masks[5, 6, 7, 8, 9], scanning near-field optical microscopy(SNOM)[10], and solid immersion lens (SILs)[11, 12, 13]. Mesas can be fabricated to a size of 40nm. Mesa structure fabrication, however, leads to possible damage to the sample. SNOM has high spatial resolution, but is a complex, large-scale system, and becomes even more complex when used at low temperatures. The PL signal intensity is also quite low for SNOM. SILs also have high spatial resolution and are much easier to use, but have low position controllability. Masks also have high spatial resolution with nanoholes down to 100nm, and by making

an array of nanoholes, it is possible to observe a QD via a nanohole without requiring the manipulation of the mask; only the positioning of the sample/mask's nanohole to the excitation/observation spot is necessary. Thus, this method is easily extended to low temperature measurements. When the mask is fabricated directly onto the sample surface, it is possible to observe the same QD through the same nanohole over a long period. However, this does not provide the high portability of a SIL. A mask consisting of a transparent substrate with a thin metal coating on one side can be made into a mask by puncturing nanoholes in the metal coating and placing the mask directly onto the sample (a portable mask). A schematic diagram of such a mask is shown in figure 5.1. Such a mask has been proposed before[14], and has the ease of use of a SIL. At the same time, an array of nanoholes can be made in a single mask. However, as with any nanometric aperture, the high spatial frequency cutoff leads to an inevitable drop in transmitted light intensity. In the end, it is desirable to have a low density sample in which single QD spectroscopy is possible by micro-PL alone.

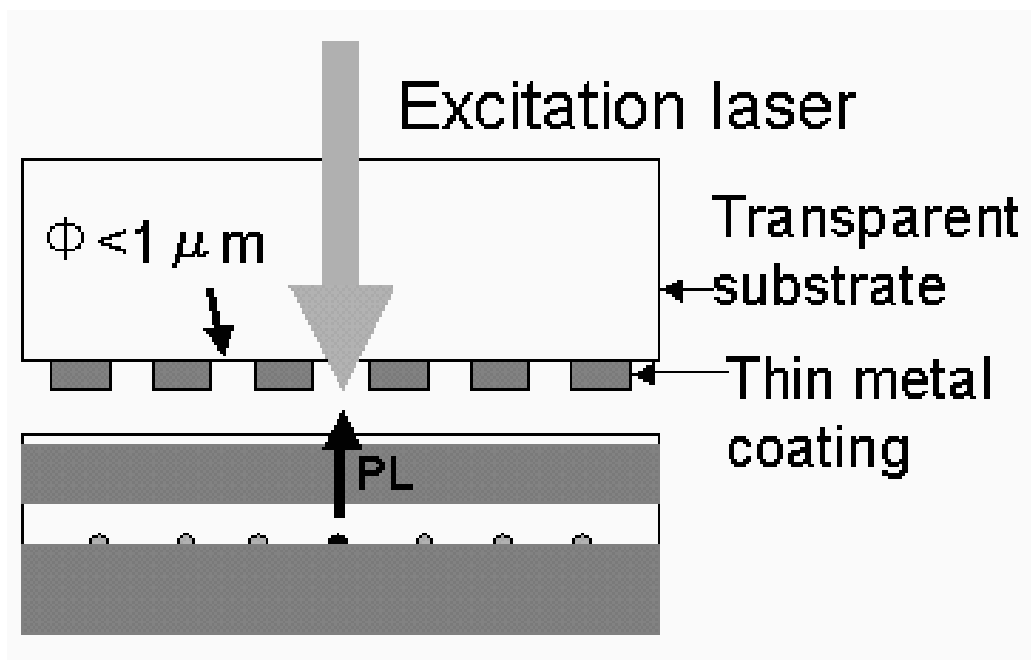


Figure 5.1: Schematic diagram of a portable mask placed on top of a sample

Initially, the feasibility of single QD micro-PL spectroscopy via a mask is evaluated by using a portable mask as a non diffraction-limited light source. The mask is made using standard micro-machining methods. The sample used is of a higher density than those made in chapter 2, and is used as a

readily available test sample for achieving single QD spectroscopy without having to process the sample in any way. Although this mask can be used as a near-field light source, it is difficult to directly illuminate a QD using near-field light because of the difficulty in maintaining nanometer order spacing between the nanohole and sample surface. Using a transparent substrate with a very flat surface ($\lambda/10$) it is possible to achieve close proximity between the nanohole and the sample surface.

Next, a mask is fabricated directly on the low density sample described in chapter 2 in order to achieve closer proximity between the nanohole and the sample surface, in the hopes of achieving better signal-to-noise ratio. The mask is made using the lift-off method[15]. Masks also have the capacity to keep the illuminated area constant for increased excitation intensity. This maintains a constant excitation area, and thus keeps other QDs in the periphery of the observed QD from also being excited at higher excitation intensities. From masked-sample micro-PL spectroscopy, an idea of single QD PL spectra is obtained.

Finally, micro-PL spectroscopy is used to obtain single QD spectra from low density QD samples with no mask, which have the same spectral characteristics of single QD spectroscopy via a mask and are expected to originate from a single QD, as will be explained later in this chapter. The fabrication of such a sample has already been explained in detail in chapter 2.

5.2 Experimental setup

5.2.1 micro-PL

In the micro-PL measurements, the sample is placed on a continuous-flow Janis ST-500 Microscopy Cryostat and cooled to below 10 K. A frequency-doubled YAG cw laser (532 nm, 20 mW) is used as an excitation light source and the light is coupled into a single-mode fiber. The light from the fiber is collimated by a fiber coupler and focused onto the sample by a $50\times$ objective lens to a spot size of $0.6\ \mu\text{m}$. The position of the excitation beam spot on the sample is controlled by adjusting the position of a concave lens placed between the fiber coupler and the objective lens. The PL is picked up by the same objective and coupled into a different single-mode fiber. The PL spectra from the fiber is observed using an Acton SpectraPro 500i 50 cm spectrometer with a 1800 g/mm grating and a liquid nitrogen-cooled CCD detector. The excitation power is changed by a neutral-density filter. A schematic diagram of the experimental setup is shown in figure 5.2.

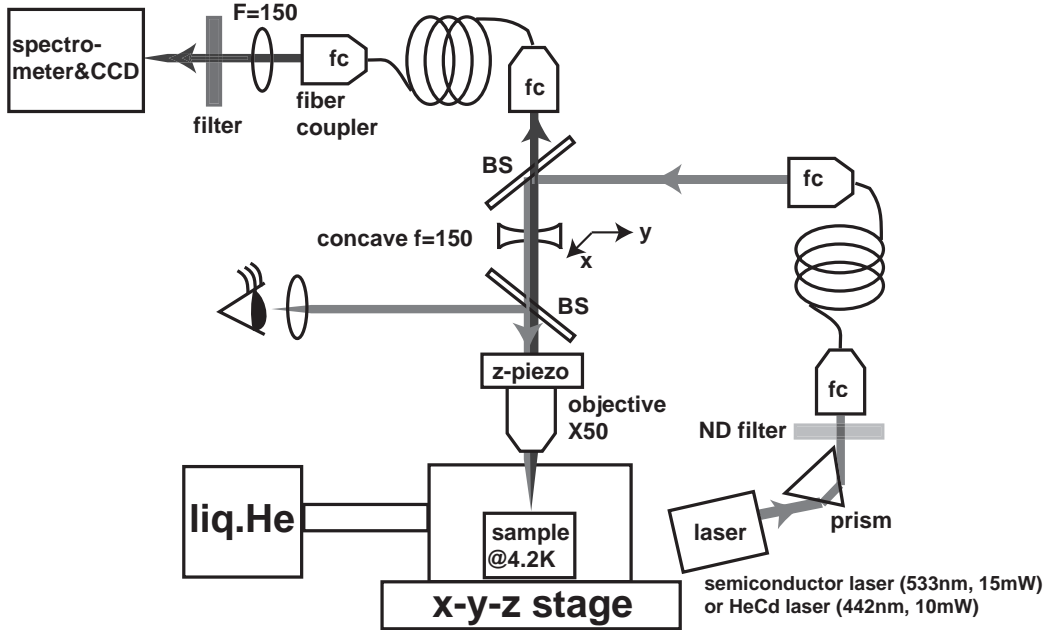


Figure 5.2: Schematic diagram of the micro-PL experimental setup

5.2.2 Gold mask design and fabrication

Gold mask design

Gold (Au) masks are designed to have nanoholes with a diameter of several hundreds of nanometers, which are smaller than the diffraction limit of the excitation light, and are made into an array of a reasonable number. The size and number of the nanohole are mainly determined by the density of the QD under study. As a test sample, a GaAs/AlGaAs QD sample made by MDE with an average QD size of 10nm and a density of $6 \times 10^8 \text{cm}^{-2}$ is used. Thus, approximately one to two QDs should exist under a nanohole with a diameter of 500nm. Statistically, one nanohole should suffice for finding a QD under a nanohole; however, to circumvent the possibility of their being no QDs under the nanohole, an array of nanoholes are made in the Au film. This facilitates the experiment at low temperatures, because one only needs to study any nanohole without the cumbersome task of raising the sample temperature back to room temperature to move the mask to a different position.

Gold mask fabrication

A quartz plate with a thickness of $750 \mu\text{m}$ and a surface roughness of $\lambda/10$ is used as a supporting substrate. One side of this plate is coated with a

thin Au film by the sputtering method, and a nanohole is punctured in this thin film using focused ion beam (FIB) etching. A schematic diagram of the fabrication process is shown in figure 5.3.

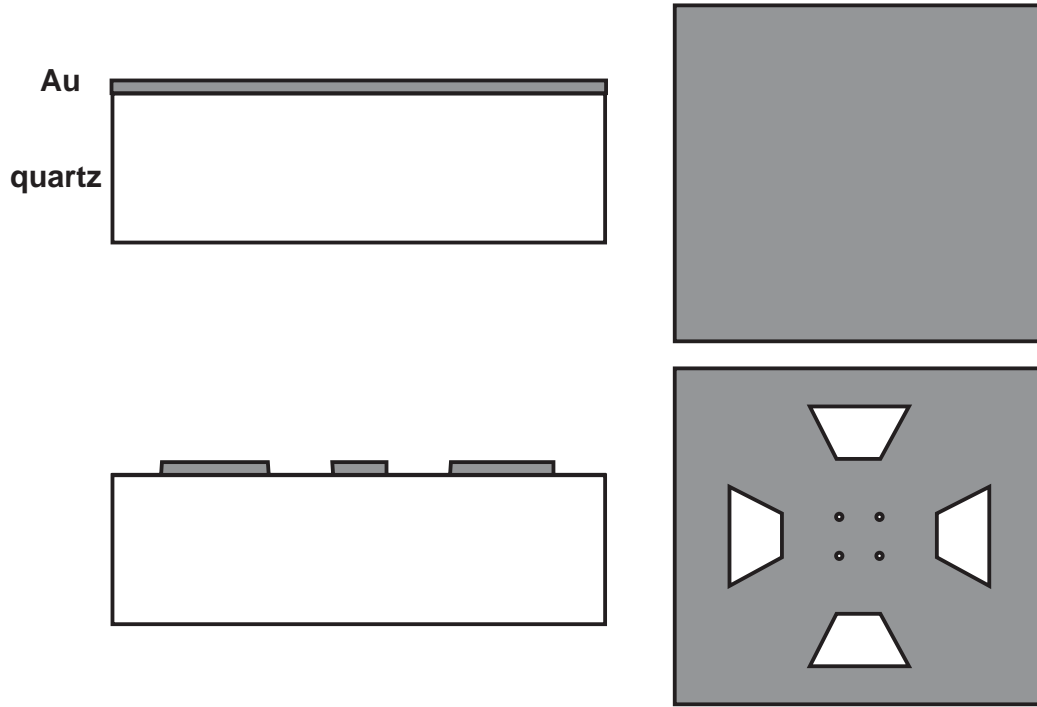


Figure 5.3: Schematic diagram of the Au mask fabrication process

The Au film thickness is thicker than the skin depth of Au to ensure that the excitation laser passes only through the nanohole and reflects elsewhere. A film thickness of over 80nm provides sufficient reflectivity while allowing enough light to pass through the nanohole. An Au film with a thickness of 200nm is made on the quartz plate.

An array of 5×5 nanoholes with a diameter of approximately 500nm are made on this Au film using an FIB system. A scanning ion-beam microscopy (SIM) image of a nanohole taken directly after FIB etching is shown in figure 5.4. A crosshair-like pattern around $10\mu\text{m}$ in size is also fabricated around the nanohole array to facilitate the finding and positioning of the sample/mask's nanohole to the excitation/observation spot. A SIM image of the crosshairs-like pattern is shown in figure 5.5.

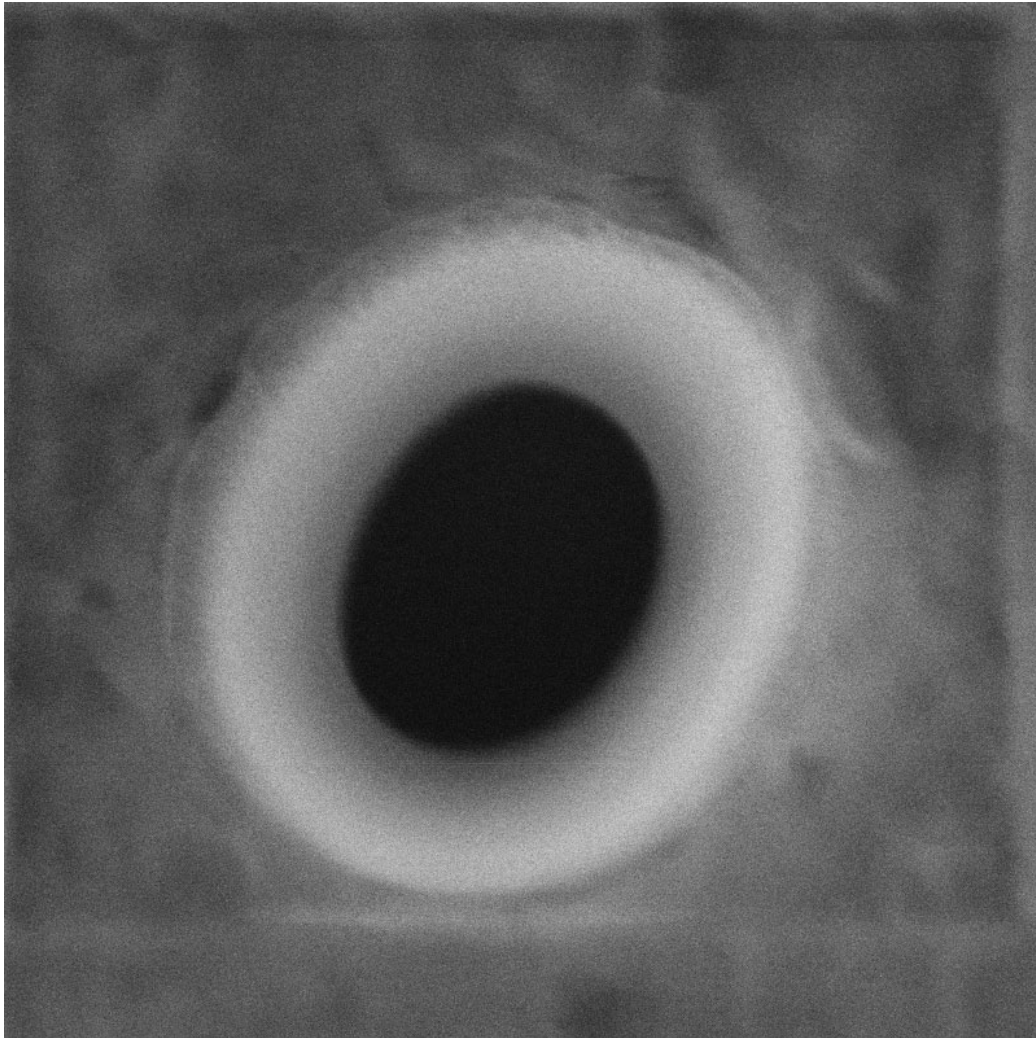


Figure 5.4: SIM image of a nanohole made by FIB etching (image area is $1.5\mu\text{m}\times 1.5\mu\text{m}$)

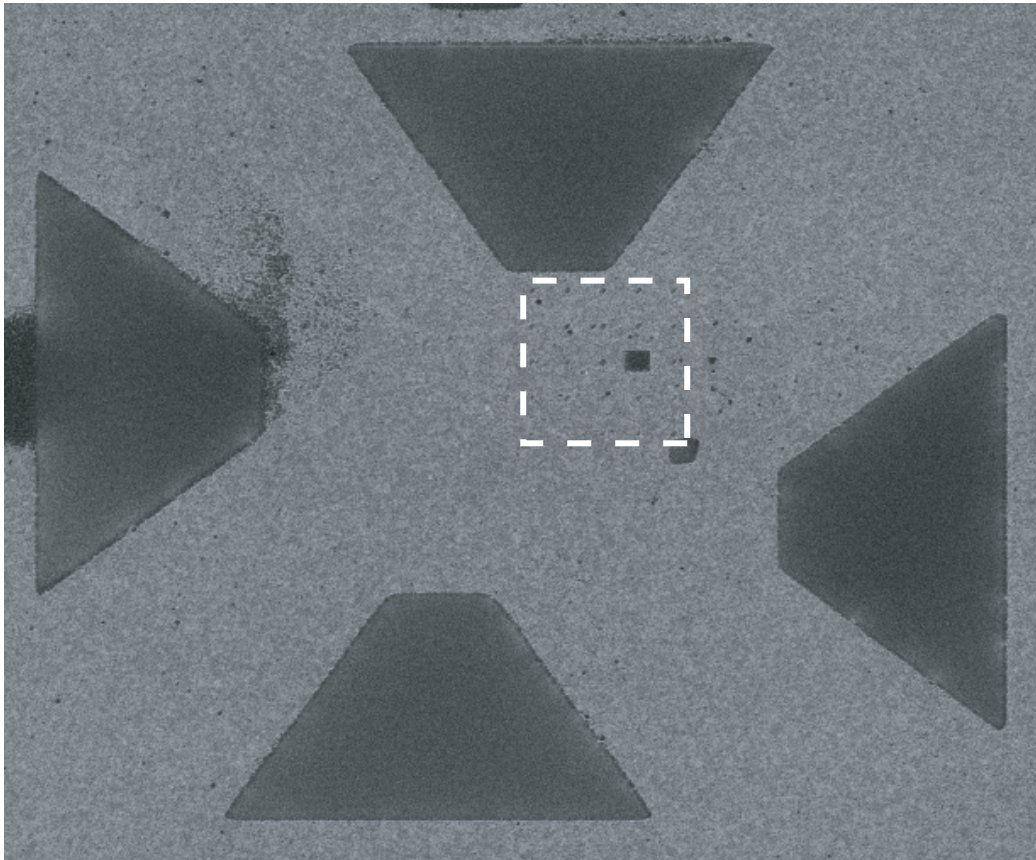


Figure 5.5: SIM image of the crosshairs-like pattern (image area is $45\mu\text{m}\times 40\mu\text{m}$) the nanohole array is made in the area outlined by the white dotted line

5.2.3 Titanium mask design and fabrication

Titanium mask design

The basic philosophy behind the titanium (Ti) mask design is the same as that of the Au mask. The size and number of the nanoholes are mainly determined by the density of the QD under study. Here, a test sample with a lower density than the one used for the Au mask is used. A GaAs/AlGaAs QD sample made by MDE with an average QD size of 40nm and a density of $3 \times 10^8 \text{cm}^{-2}$ is used. The growth conditions are similar to those outlined in chapter 2. In order that one or no QD exists under the nanohole, a 3×3 array of nanoholes with a diameter of 500nm, as well as a 7×7 array of nanoholes with a diameter of 200nm was designed. Due to the fact that, once the mask is fabricated on the sample, it cannot be moved as the portable mask can, the number of nanoholes in the array are increased so that, statistically, several nanoholes which are made on top of a QD exist.

Titanium mask fabrication

E-beam lithography was used to pattern the nanohole onto the sample. Ti was chosen as a readily available material for thin film fabrication by vacuum evaporation. The Ti skin depth at 533nm excitation wavelength was determined to be 34nm. Here, a Ti thin film thickness of 100nm was fabricated. Hydrofluoric Acid (HF) was chosen as a Ti etchant that does not attack GaAs. The Ti material over the patterned resist was etched by HF, and the e-beam resist was washed away, resulting in the fabrication of a nanohole in a Ti film. A scanning electron-beam microscopy (SEM) image of the mask nanohole is shown in figure 5.6.

5.3 Results

5.3.1 Single QD spectroscopy using a gold mask

When the Au mask is placed on the test sample, interference patterns are seen in the area of the mask where no gold is sputtered. From this pattern, it is estimated that the sample surface-Au mask spacing is less than $1 \mu\text{m}$.

The nanoholes, which are not discernible by eye even under a microscope, can be more easily found by first looking for the crosshair-like pattern. The actual fine-positioning of the sample/mask is done by centering the excitation/observation spot to the center of the crosshair-like pattern and then randomly moving the sample/mask in small steps while monitoring the PL

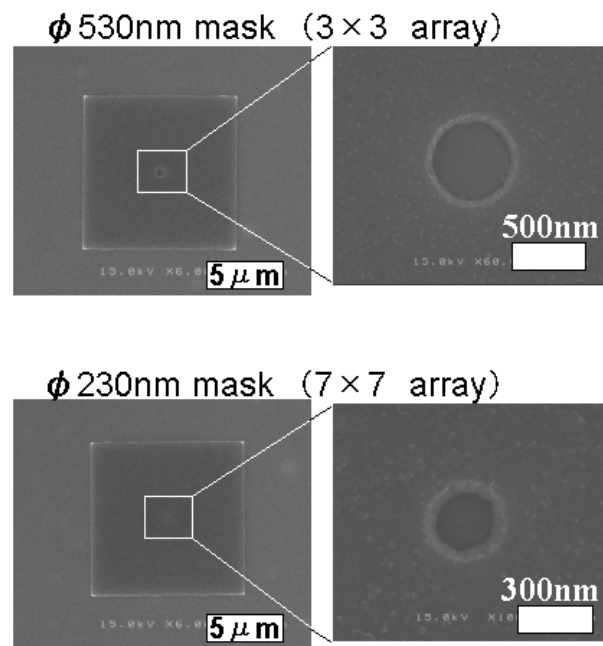


Figure 5.6: SEM image of the Ti mask nanohole

spectrum in real time. The PL from the barrier material, which should appear through any excited nanohole, is used as a signal which indicates whether the excitation spot is over the nanohole or not; a strong AlGaAs PL signal should appear only when the excitation spot is over the nanohole. By this method, the best excitation spot position relative to the nanohole is found. Once this position is found, the concave lens of the micro-PL setup is used as a final fine-tuning mechanism to find the best excitation/observation spot position. This is done by maximizing the AlGaAs PL peak intensity.

The PL spectrum of the test sample is shown in figure 5.7. The QD PL has a spectrum centered at 1.710eV with a FWHM of 209meV. As can be clearly seen, the inhomogeneous broadening hides the expected sharp spectral peaks of the individual QDs.

An example of a wide spectral-region micro-PL spectra of the test sample without and with a mask are shown in figure 5.8. An example of a short spectral-region micro-PL spectra of the test sample without and with a mask are shown in figure 5.9. The spectra are taken at 10K.

From figure 5.8, it can be seen that the micro-PL spectrum without a mask has many sharp peaks originating from many QDs' ground state recombinations and possibly also their excited levels, and it is impossible to assign any of the peak's origin to individual QDs in any comprehensible manner. The micro-PL spectrum with a mask, however, shows one peak in the entire spectrum. This is so for the spectral region from the AlGaAs PL to the sample substrate bulk GaAs PL, where the QD PL is expected to be seen. The reason for the rather large FWHM of this peak, compared to that of the micro-PL spectrum without a mask, is due to the reduced spectrometer resolution. The resolution was reduced in order to accumulate the PL signal weakened by the presence of the Au mask.

In order to confirm that a single QD PL line is observed, the spectra are taken at higher spectral resolutions. From figure 5.9, it can be seen that the single PL peak in the micro-PL spectrum with a mask has a FWHM comparable to those of the peaks seen in the micro-PL spectrum without a mask, taken at a nearly equivalent resolution. Thus, it can be said that a single QD PL spectra has been obtained by micro-PL with the assistance of a mask, from a sample in which single QD PL was not possible otherwise.

It is interesting to note that, in figure 5.9, the micro-PL spectrum without a mask is taken using an excitation intensity which is smaller than that of the micro-PL spectrum with a mask; generally, one would expect more QDs to be excited as the intensity is increased, yet only a single QD PL peak is seen when a mask is used. This is the effect of the fixed excitation spot size due to the mask. A reduction in the excitation intensity due to the small nanohole size, however, cannot be ignored.

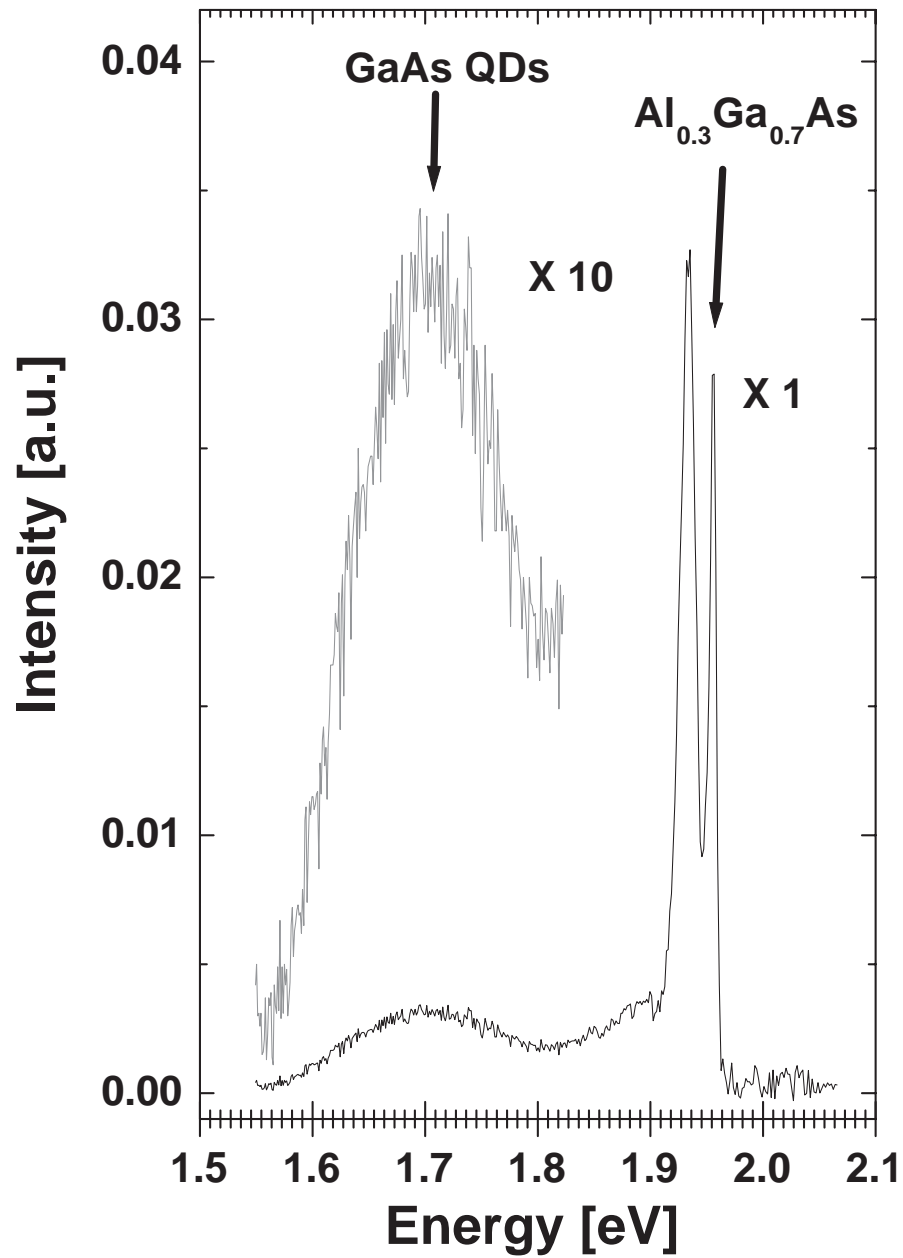


Figure 5.7: PL spectrum of test sample used for Au mask evaluation

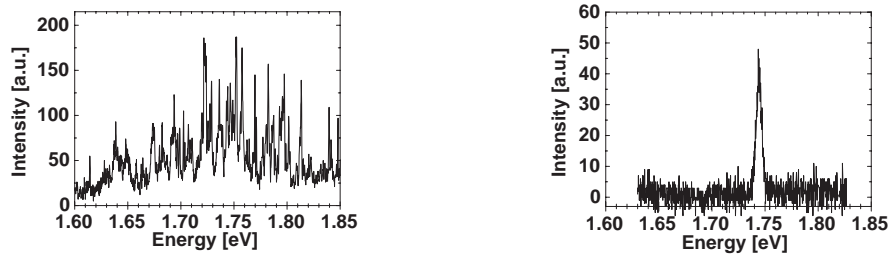


Figure 5.8: Wide spectral-region micro-PL spectra without (left) and with (right) a mask (spectral resolution and excitation power for the spectrum without a mask: 0.42meV, 0.15mW; with a mask: 0.61meV, 0.02mW)

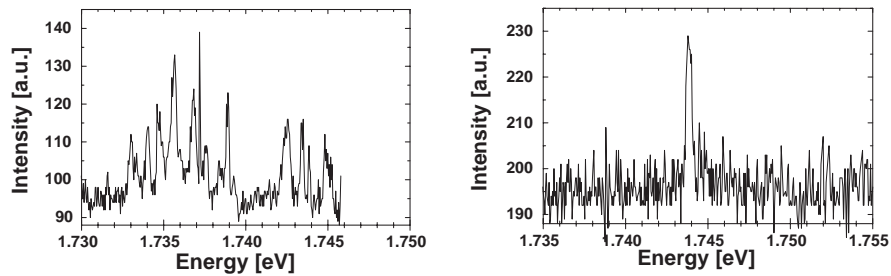


Figure 5.9: Short spectral-region micro-PL spectra without (left) and with (right) a mask (resolution and excitation power for the spectrum without a mask: 0.15meV, 0.05mW; with a mask: 0.17meV, 0.15mW)

5.3.2 Single QD spectroscopy using a titanium mask

Comparison with the gold mask

Au mask micro-PL spectroscopy proves the feasibility of using a mask for single QD spectroscopy. The low PL signal intensity is a drawback, however, when one wishes to see various excited peaks originating from a single QD with high spectral resolution. The observation of such spectra is necessary, as the point of single QD spectroscopy using a mask is to determine the spectral characteristics of single QDs. From similarities in the spectral structure, it is possible to characterize the spectrum of single QD spectra. Observations of such spectra may be difficult when using an Au mask, due to the decreased excitation and PL intensity resulting from the small nanohole size, the distance from the nanohole to the sample surface, and possibly some residual Au in the nanohole. The methods for circumventing these problems are to make a larger nanohole at the cost of a lower spatial resolution, to make the mask directly on the sample at the cost of losing the portability of the Au mask, and to make the mask by the lift-off method. The first method is non-negotiable, as the sample's QD density cannot be changed once the sample is grown. Thus, the growth of a lower density sample becomes necessary. The second method is acceptable, as portability is not an important issue when concentrating on one type of sample, and even more so when it is possible to grow as many desired samples as necessary. The third method is highly desirable, and leads to the fabrication and use of the Ti mask.

Analysis of the electric field distribution under a nanohole

Here, before any further analysis of micro-PL spectra via the Ti mask is discussed, it is necessary to address a basic question concerning the diffraction of light from a nanohole. Simply put, light coming from a nanohole should be diffracted in a wide solid angle, thus exciting a larger area under the nanohole than that which is directly under the nanohole. To see whether this is actually so, a numerical analysis of the electric field distribution under a nanohole is conducted. The finite difference time domain (FDTD) calculation is a good method for the analysis of the electric field distribution of nanometric structures[16], and is adopted here. In the FDTD method, the analysis space is first discretized in both time and space, and then Ampere's and Faraday's equations are solved on the mesh. The cell size is chosen according to the desired resolution, which is chosen to be much smaller than a wavelength for accurate results. The analysis space of the mask nanohole is modeled in two dimensions, and a two dimensional FDTD code (FDTD2D[17]) is used. An excitation light source wavelength of 544nm

and an excitation power of 15mW is assumed. The schematic diagram of the analysis space with material size and optical parameters, and the two dimensional FDTD calculation result are shown in figure 5.10.

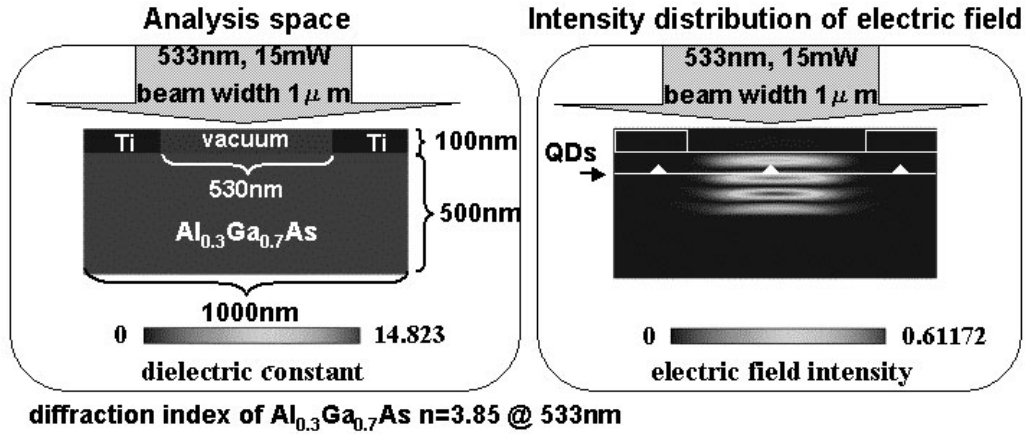


Figure 5.10: Schematic diagram of the analysis space (left) and the two dimensional FDTD calculation result (right)

Surprisingly, the beam is well collimated under the nanohole to below the depth of the buried QDs. This phenomenon is most probably due to the high refractive index of AlGaAs, which is 3.85 at 533nm. From this analysis, it can be expected that, when studying QDs via the Ti nanohole by micro-PL spectroscopy only, the QDs in the area directly under the nanohole is excited.

micro-PL of sample via Ti mask

The Ti mask has been shown to be viable for the micro-PL spectroscopy of QDs under the nanohole by FDTD analysis. Here, an example of the micro-PL spectrum of the sample without a mask is shown in figure 5.11. Although this is only a test sample, the growth conditions are almost the same as those explained in chapter 2 (only the Ga flux is slightly higher at 0.1ML/s) and is

thus expected to share the characteristics of the sample described in chapter 2, such as the bimodal growth of different sized QDs. The spectrum is taken at 8K, with a spectral resolution of 0.25meV.

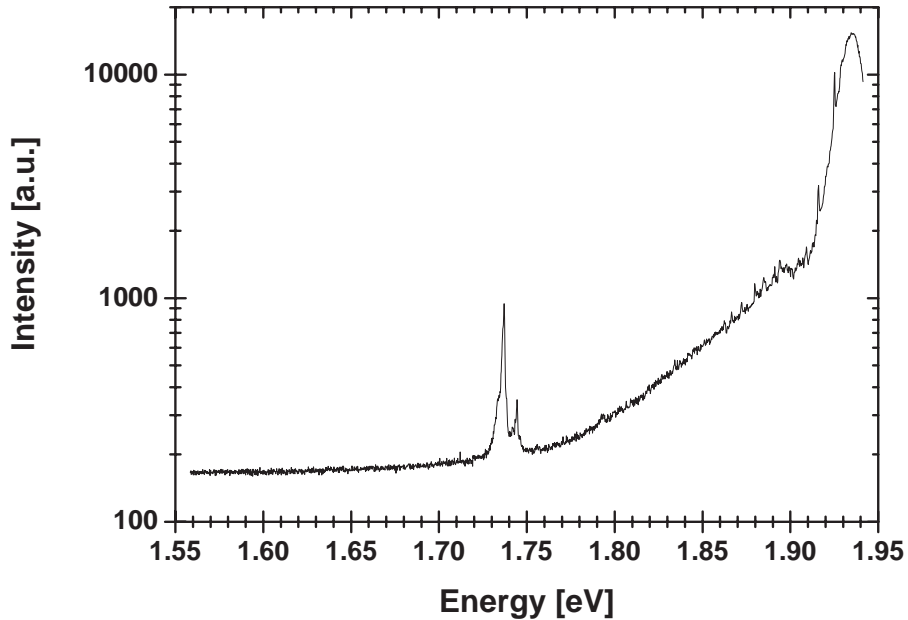


Figure 5.11: micro-PL spectrum of sample used for the Ti mask ($T=8\text{K}$, 0.25meV resolution, excitation source: HeCd laser (442nm))

Here, only one peak group (consisting of at least two peaks) is seen in the entire spectrum from the AlGaAs PL peak to the bulk GaAs peak. The peak at the higher energy side belongs to the impurity-bound AlGaAs excitonic peak. In order to determine whether this peaks originates from a single QD, an example of the micro-PL spectrum of the sample taken via the Ti mask nanohole of 530nm diameter is shown in figure 5.12.

From the “confining” QD density of this test sample, as arugued in chapter 2, it is expected that at most one QD will be found under a nanohole of 500nm diameter. Thus, it can be said that figure 5.12 represents the spectrum coming from a single QD. The characteristics of the spectrum are similar to those seen in figure 5.11, i.e. the spectrum consists of a sharp peak with a broader peak at the lower energy side, and no other peak can be seen from the AlGaAs peak to the bulk GaAs peak. Furthermore, the test sam-

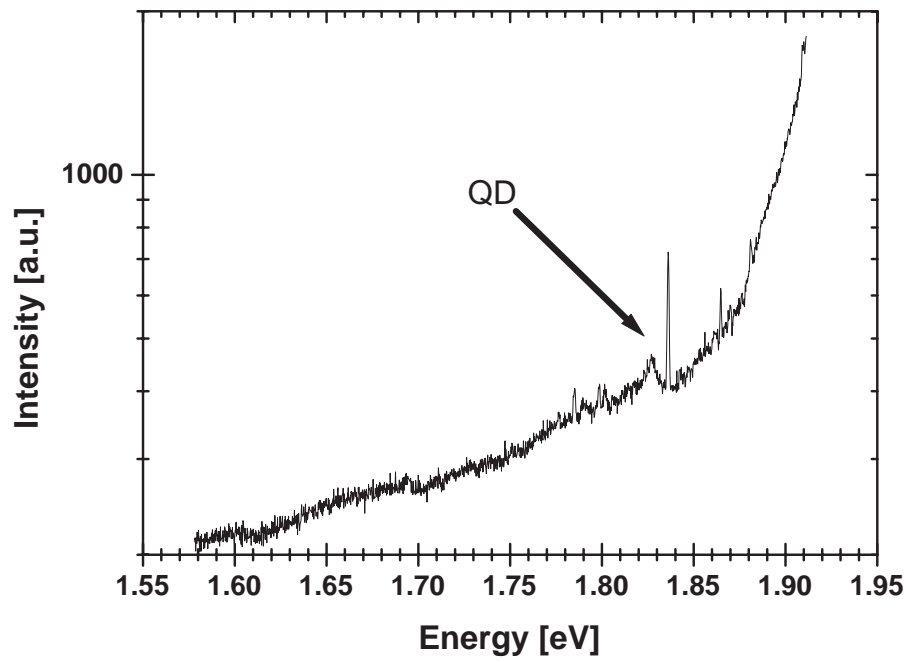


Figure 5.12: micro-PL spectrum of sample taken via the Ti mask nanohole ($T=8\text{K}$, 0.51meV resolution, excitation source: frequency-doubled YAG laser (533nm))

ple also has the bimodal growth of QDs observed in the sample described in chapter 2. Since the number of QDs excited in micro-PL spectroscopy without a mask should be an average of three for a spot size of $1\mu\text{m}$, it can be said that only the small QDs in the samples show strong confinement, resulting in the PL peak at the higher energy side of the spectrum. This, combined with the comparison of the spectrum taken with and without the Ti mask, leads to the conclusion that single QD spectroscopy is achieved in this type of QD whether there is a mask or not.

Excitation intensity dependence of micro-PL spectrum of sample via Ti mask

To observe various excited peaks originating from a single QD with high spectral resolution, the excitation intensity dependence of the micro-PL spectrum is taken via the Ti mask nanohole of 530nm diameter, and is shown in figure 5.13.

Two peaks, labeled A and B, are seen at high excitation intensities. Following the argument stated above, these two peaks are expected to originate from a single QD. In excitation intensity dependence PL, the excitons are expected to fill the QD states from the lowest energy levels. Thus peak A is expected to be from the ground state exciton recombination. The energy spacing between these two peaks are approximately 28meV. The confined heavy hole energy level spacings measured in chapter 4 was 24meV, and is very close in value to the A-B peak energy spacing. On the other hand, the first excited state-ground state energy spacing was calculated to be between approximately 71 to 87meV. Thus, it can be said that the ground state electron inside the QD conduction band recombining with the heavy hole in the first excited state of the QD valence band is seen in peak B. Such a recombination in bulk semiconductors is not allowed. However, due to the confinement of the wavefunctions in the QD, there is a greater overlap of the wavefunctions; the coupling between optically allowed and forbidden transitions induced by Coulomb interaction among the carriers occurs. Thus, such an emission line can be observed. This kind of emission will be discussed later in single QD spectroscopy in detail. The same spectrum is expected to be seen from the sample by micro-PL without a mask.

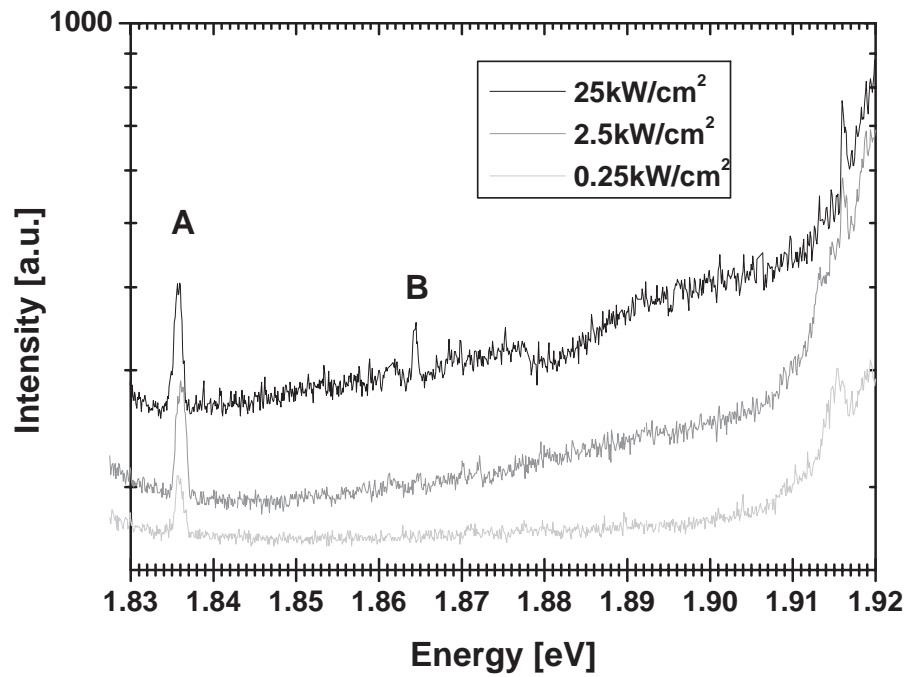


Figure 5.13: Excitation intensity dependence of the micro-PL spectrum of sample taken via the Ti mask nanohole ($T=8\text{K}$, 0.26meV resolution, excitation source: frequency-doubled YAG laser (533nm))

5.3.3 Single QD spectroscopy

Introduction

From the previous arguments of single QD spectroscopy via a mask, it can be expected that the micro-PL spectrum from a single GaAs QD can be observed from the GaAs/AlGaAs QD sample described in chapter 2. Furthermore, the various spectral lines which appear at high excitation intensity can be attributed to carrier recombination emission from various discrete levels inside the QD.

In order to circumvent the possibility that two QDs in close proximity to each other are being observed, the micro-PL spectrum of every QD under study is observed in real time at strong excitation while the concave lens shown in the experimental setup in figure 5.2 is moved in two perpendicular directions. While the concave lens is being moved, two issues determine whether the observed spectrum is from a single QD or not: (i) the main peak, which is considered to be the only peak to appear at low excitation intensities, as well as those peak in close proximity to this peak is constantly the most intense peak, and any other peak which appears with a stronger intensity is considered to be from a different dot, and (ii) the correlated peaks whose relative intensities change in unison to each other are considered to come from the same single QD. The first issue is justified by the fact that emission from any state other than the ground state cannot be more intense than that from the ground state, considering the fact that most of the carriers should non-radiatively relax to the ground state before recombining to emit a photon. The second issue is justified by the fact that the resolution of the excitation spot step by adjustment of the concave lens is calculated to be close to 100nm. Considering the low QD density, as well as the order of the QD size, which is 10nm, it is safe to say that the concave lens is capable of focusing the excitation spot around a single QD with spatial resolution high enough to discern one QD from another. Here, a Gaussian excitation spot is assumed, and the intensity of the PL signal from the QD is considered to drop off as the center of the Gaussian excitation spot moves away from the QD.

In this section, the excitation intensity dependence of the single QD micro-PL spectrum is measured in order to understand the energy levels within the QD as well as the energy level renormalizations due to many-carrier correlations within the QD. Excitation intensity dependence is a powerful method for studying such properties of QDs, as increasing the excitation intensity can increase the number of confined carriers in the QD. As the carriers fill the discrete levels according to Pauli's principle, in which only two

carriers of opposite spin can fill any given level, state filling occurs, and at high excitation intensities, the carriers begin to fill higher energy levels, as shown in figure 5.14. Thus, recombination emissions from carriers in higher energy levels can be observed. The PL spectra of the recombination emission of these carriers reflect the states of the individual carriers as they recombine. That is, carriers experience an added many-body interaction energy caused by the existence of other, non-recombining carriers (“spectators”) before they recombine, thus slightly lowering the photon energy created by the carriers’ recombination.

In this experiment, the excitation intensity dependence of the single QD micro-PL spectrum is studied. In particular, the peaks which appear at an energy approximately 20meV higher than that of the main peak is studied. Also, the peaks which appear at an energy several meV lower than that of the main peak (i.e. the ground state recombination emission) is also studied in detail.

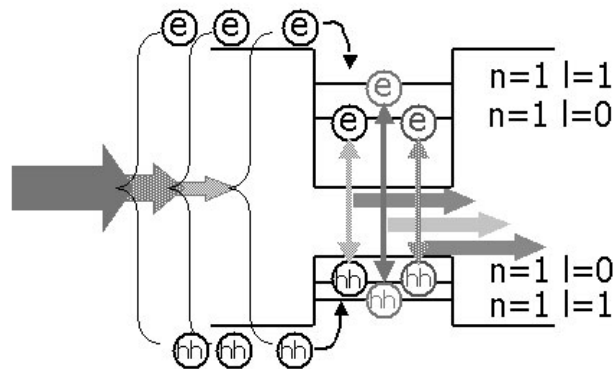


Figure 5.14: Schematic diagram of the optical state filling of the QD energy levels with increased excitation intensity

Single QD spectroscopy - GaAs/Al_{0.256}Ga_{0.744}As QD sample

The PL spectrum of the low density GaAs/Al_{0.256}Ga_{0.744}As QD sample described in chapter 2 is shown in figure 5.15. The Al concentration x is 0.256.

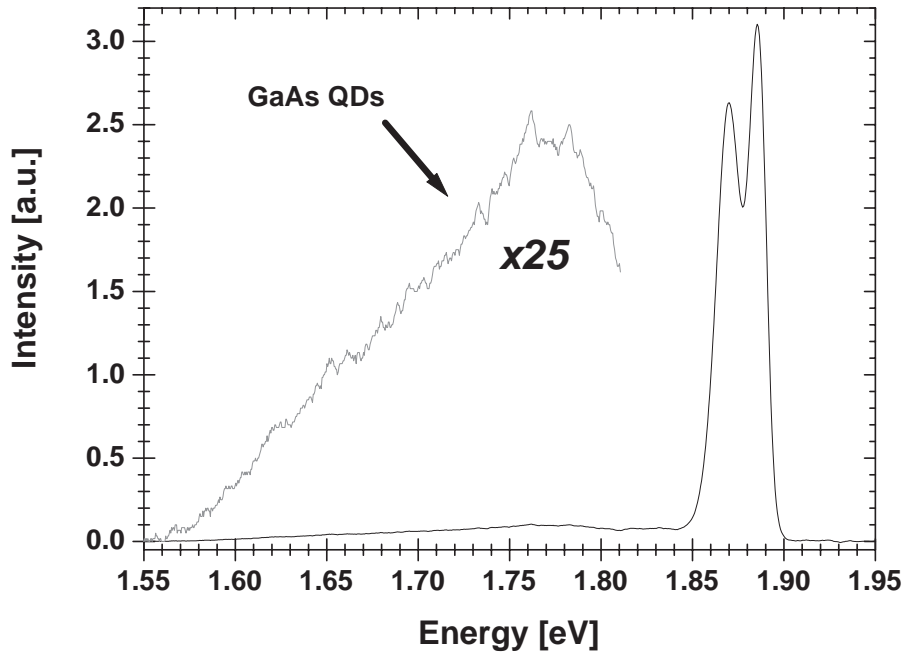


Figure 5.15: PL spectrum of low density GaAs/Al_{0.256}Ga_{0.744}As QD sample

The PL intensity from the QDs is low compared to that of the barrier, due to the low QD density. The FWHM of the QD PL is approximately 200meV, which is rather broad. The QD PL is centered at 1.77eV. No PL from a wetting layer can be seen, confirming that no wetting layer exists in this sample.

An example of the single QD micro-PL spectrum excitation intensity dependence, out of the many taken, is shown in figure 5.16. The intensity is shown in the logarithmic scale, in order to emphasize the peaks with small intensities. These are the only peaks seen in the spectral region from the substrate bulk GaAs PL peak to the barrier AlGaAs PL peak, where the QD PL peaks are expected to appear. The peaks in figure 5.16 originate from

a single QD. These spectra, along with all further PL spectra, are taken at 10K, with 0.1meV monochromator resolution, using a frequency-doubled YAG laser (533nm) as an excitation source.

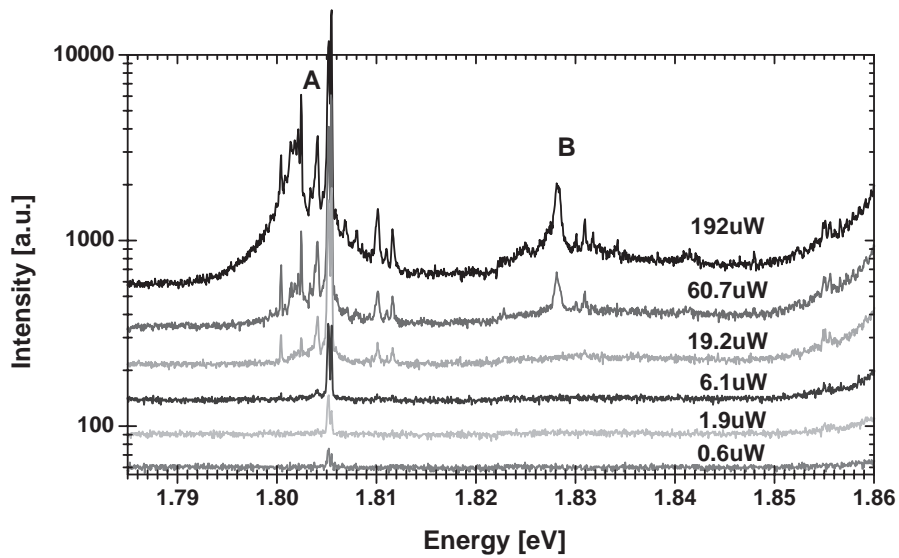


Figure 5.16: Single QD micro-PL spectrum excitation intensity dependence of low density GaAs/ $\text{Al}_{0.256}\text{Ga}_{0.744}\text{As}$ QD sample

At high excitation intensities, two strong peak groups (labeled A and B) appear, with approximately the same energy difference as the peaks A and B in figure 5.13. In this case, the peak group separation is 23meV. The characteristic of peak group A is that it consists of discrete, sharp peaks separated by approximately 1meV from the main peak. The main peak is the only peak to appear at low excitation intensities. In some cases, the main peak is a doublet, and remains so even at the weakest excitation intensities. The characteristic of peak group B is that it consists of at least two relatively

sharp peaks near the center of a broad peak. Peak groups A and B will be the center of discussion in the following arguments concerning the QD energy levels and carrier correlations.

In some single QD spectra, peaks appear with an energy difference of approximately 80meV. Peaks with such energy separation cannot be observed from single QDs with ground state emissions higher than 1.77meV.

An example of the single QD micro-PL spectrum excitation intensity dependence of peak group A is shown in detail in figure 5.17. The intensity is shown in the logarithmic scale, in order to emphasize the peaks with small intensities. Several peaks appear at the lower energy side of the main peak at high excitation intensities, with a spacing of approximately 1meV. The peaks appear with increased excitation in the order closest to the main peak. In other words, the closer the peak is to the main peak, the more distinct they become as excitation intensity is increased. The labeling of the peaks will be referred to later, in the calculation of the carrier exchange interaction energies.

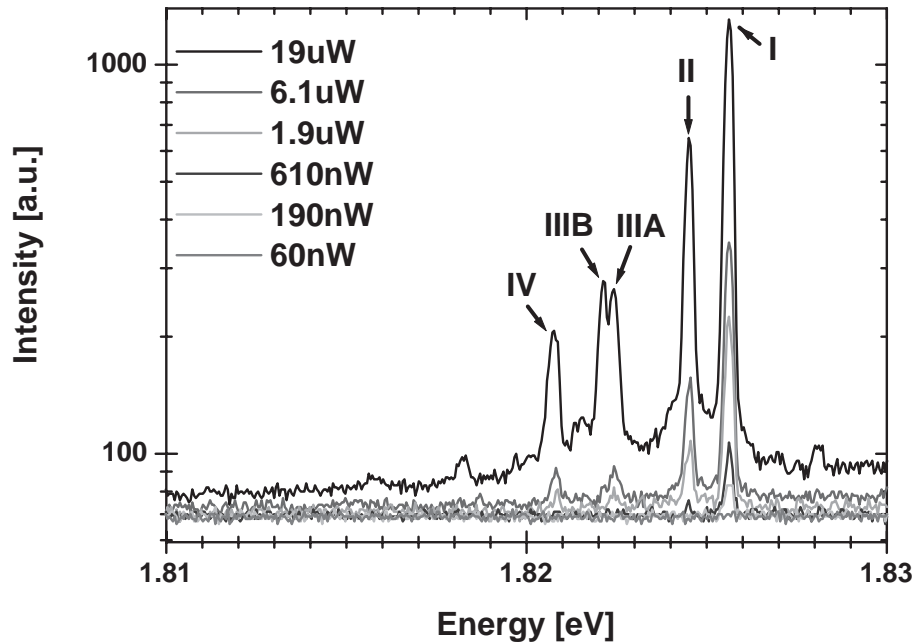


Figure 5.17: Single QD micro-PL spectrum excitation intensity dependence: the peaks near the lower energy side of the main peak

In order to correlate the various peaks in the peak groups A and B, the excitation intensity dependence of the single QD micro-PL spectrum is taken with minute increases in excitation, and is shown in figure 5.18. The excitation power is that which is measured after the $50\times$ objective lens. A redshift of peak group A is seen, which tends to broaden with increasing excitation intensity. The appearance of peak group B is also seen at high excitation intensities.

The intensities of the peaks in group A of this spectra are plotted for excitation intensity in figure 5.19. Peak I is seen to grow linearly with excitation intensity. Peaks II and IIIa are seen to grow super-linearly with excitation intensity. Thus, peaks II and IIIa are likely to be related to biexcitonic recombinations. The onset of the appearance of peaks II and IIIa is at $3.4\mu\text{W}$; this amounts to 9.1×10^{12} photons. Although some of these photons are absorbed and re-emitted by the AlGaAs barrier, and the number of photons which are introduced into the QD as carriers are not entirely relaxed radiatively, it gives an estimate of the order of the maximum intensity in which the creation of a single exciton occurs.

The peaks in group B of the spectra in figure 5.18 are shown figure 5.20. Here, at least five discrete peaks are discernible. The intensities of these peaks, along with the intensities of the peaks in peak group A of the spectra in figure 5.18 are plotted for excitation intensity in figure 5.21.

As can be seen, peak group B appears abruptly as the intensity of peak II and IIIa grow rapidly. At the same excitation intensity, peak IIIb appears. A vertical line is drawn at this excitation intensity as a guide to the eye. This intensity amounts to three times the maximum intensity in which the creation of a single exciton occurs. Thus, peak IIIb is most probably related to the existence of three excitons in a QD. It can also be seen, at the positions of the other two vertical lines, that peaks I, II, and IIIa are seen to decrease and then increase, while peak IIIb and the peaks in peak group B are seen to do the opposite, in unison. This indicates some correlation between peak groups A and B.

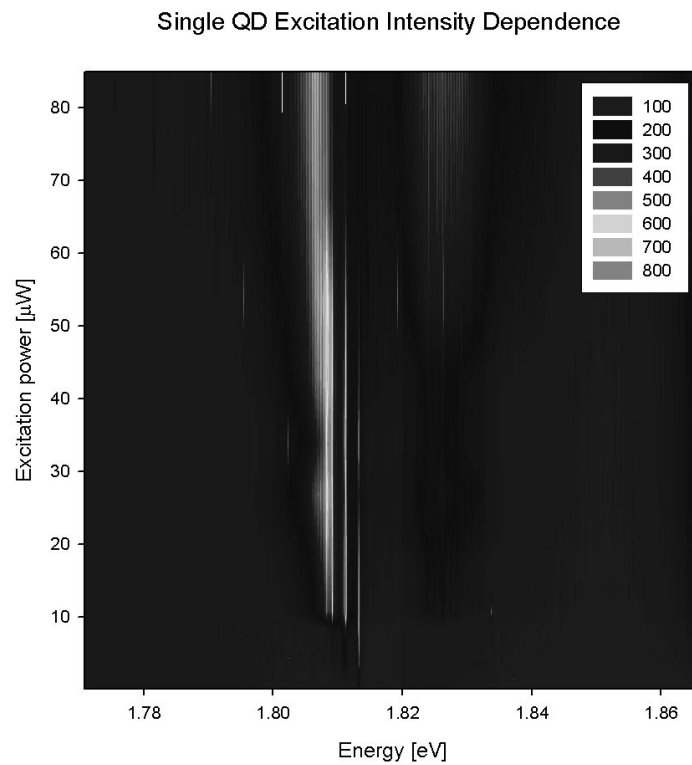


Figure 5.18: Single QD micro-PL spectrum: a detailed image of the excitation intensity dependence

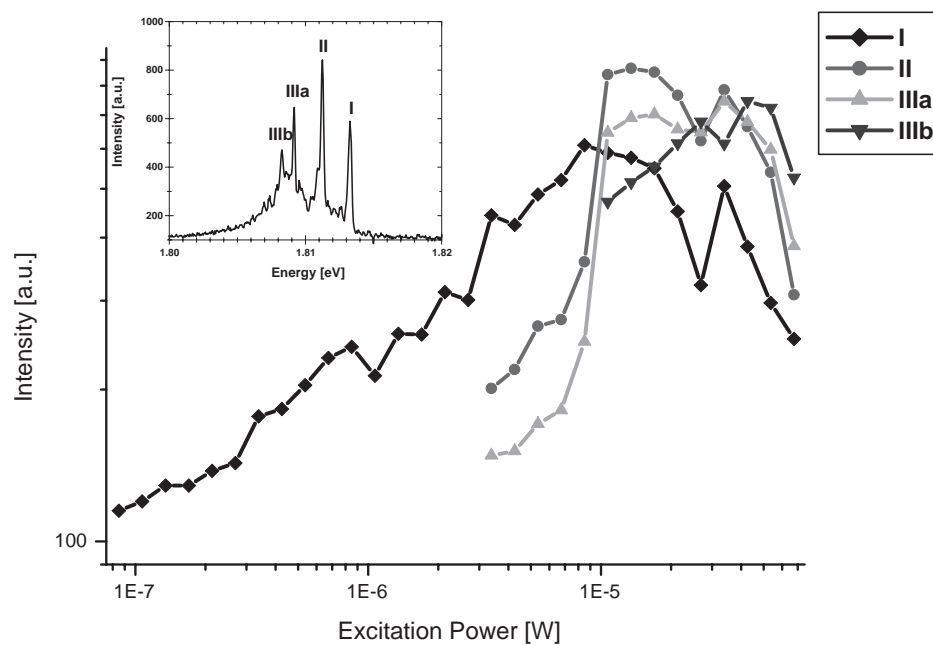


Figure 5.19: Group A peaks' PL intensity-excitation intensity dependence (the inset shows the peak assignment)

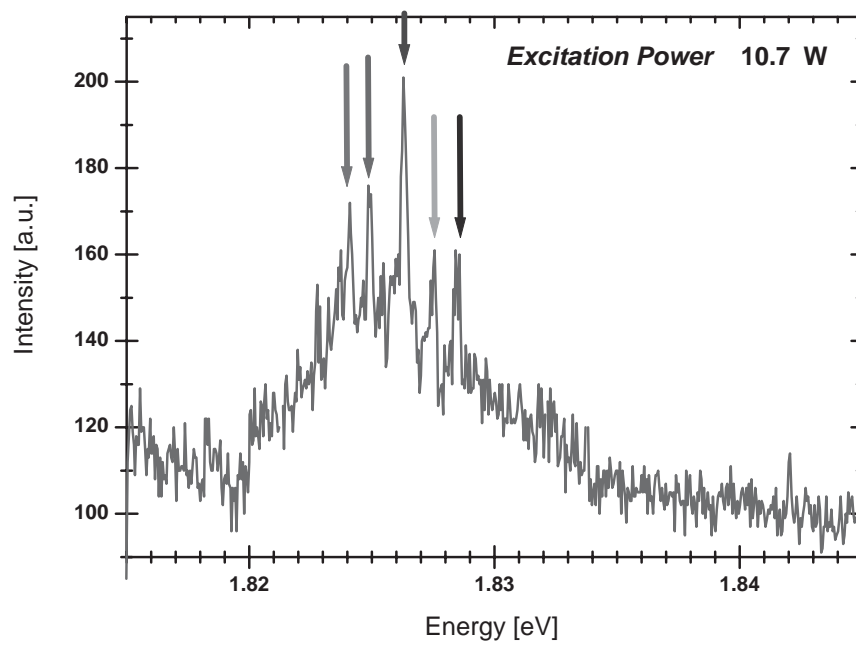


Figure 5.20: PL spectra of the peaks in group B

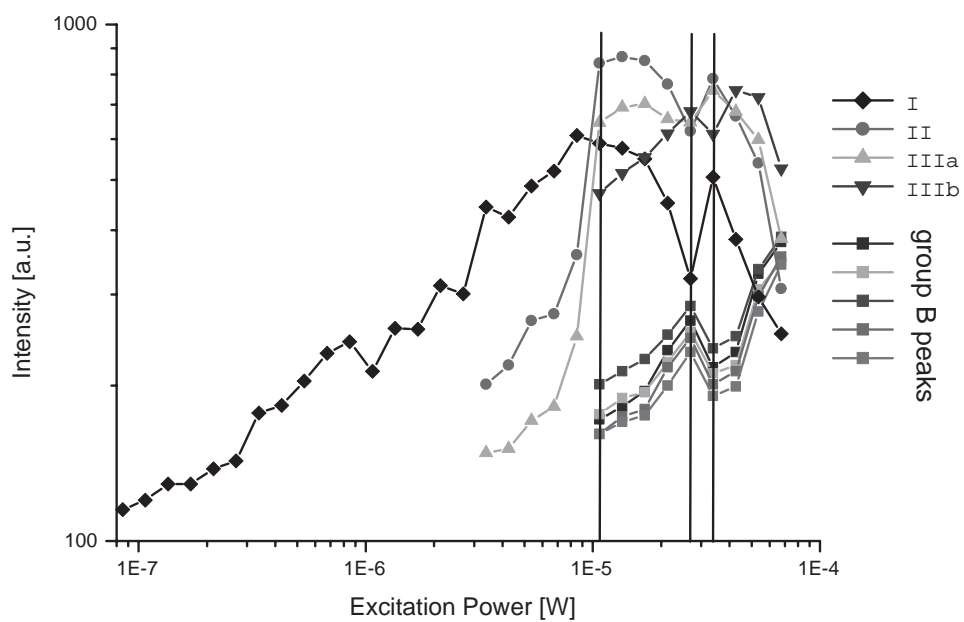


Figure 5.21: Peaks belonging to groups A and B - PL intensity-excitation intensity dependence

5.4 Conclusions

From the characteristics of single GaAs QD masked-micro-PL spectra, an idea of a single GaAs QD PL spectrum is achieved. From this, along with the arguments concerning “confining” QD density, the conclusion is that single QD micro-PL measurement without the use of a mask is possible, and is actually demonstrated in this thesis. This is an important point, as any use of a mask involves the reduction of the signal-to-noise ratio, making the reliable analysis of the spectra rather difficult. From single QD micro-PL measurements without a mask, sharp peaks originating from carrier recombinations confined in a single QD are clearly verified. The introduction of more than one exciton inside the QD is achieved by observing the excitation intensity dependence of the single QD micro-PL spectrum. From this observation, two prominent peak groups (A and B) are seen to appear as excitation intensity is increased. A correlation between the intensity of these peak groups is seen, thus confirming that these peak groups originate from the same QD. From the effective mass calculations in chapter 4, it is found that the energy level spacings are to the order of tens of meV. Thus, peak group B will be considered to originate from carrier recombinations from higher energy levels in the following analysis. The peaks in group A are expected to originate from the ground state under various carrier correlation influences, which affect the energy of the photon during the recombination of the carriers, and will also be analyzed in detail.

5.4.1 Energy levels of the GaAs QD

Energy levels of individual QDs

The transition energies of the GaAs QD are calculated using the effective mass calculation described in chapter 4, with the interdiffusion length l taken into consideration; the calculated values are compared to the peaks’ spacings of the single GaAs QD spectra to determine the origin of the peaks.

At this point, the QD size and its relation to the QD’s ground state emission must be established. Generally, as the QD size becomes smaller, the confinement energy increases, and the QD’s ground state emission shifts to higher energies. Of course, one may adopt the size of the exciton radius as the actual QD size; however, this requires that the electron-hole pair confined in the QD is not in the strong confinement regime, i.e. that the electron-hole pair can exist as an exciton inside the QD. So far, the electron-hole pair confined in QDs have been referred to as excitons in this thesis; however, the QDs under consideration have a size of the order of the bulk

GaAs exciton radius and thus confines an electron-hole pair in the strong confinement regime (i.e. as an electron-hole pair). The term “exciton” will be used as well as “electron-hole pair” throughout the rest of this thesis to describe an electron-hole pair confined in the same spatial region due to the QD potential.

Thus, further arguments concerning the energy levels of the QD will be conducted in terms of the QD’s ground state emission energy.

First, pre-annealed conical QDs are assumed with a distribution of base sizes of 5, 10, 15, 20, and 25nm. This is done to ensure that the calculated values of E1 and E2 are determined for a ground state emission in a wide spectral range, thus simplifying the comparison of these values with the values determined by experiment. The height of the conical QD is kept constant at 16nm. This assumption is made on the basis that the Ga droplet, once crystallized, are covered by GaAs grown at low temperatures by MEE. Thus, the height of the QD is expected to be more or less the same value. An average height of the conical QD is chosen in order to reduce the number of different-sized QD which are included in the calculations. Next, the effect of annealing, taking l as a parameter, is calculated using the method outlined in chapter 2. The QD profile is thus smoothed out, as depicted in figure 2.5. The possible values of l determined by macroscopic high pressure spectroscopy measurements give only an estimate of the general interdiffusion length l , and the actual value of l must have a distribution, most likely dependent on QD size, but also on other parameters such as the local variations in Al concentration in the barrier. Thus, the actual value of l should be slightly different from dot to dot. Therefore, a distribution of l is allowed for each QD with different base sizes. The values of l used in the calculations are 0.5,1.0,1.5,2.0,2.5, and 3.0nm. Finally, the effective mass calculations are conducted for all 30 different-shaped QDs.

Material parameters are given in table 5.1. An Al concentration (x) - dependent effective mass for the barrier is used in the calculations[18, 19].

Table 5.1: Material parameters used for the effective mass calculations

	band mismatch (eV)	$m_{r,z}^{GaAs}(m_0)$	$m_{r,z}^{AlGaAs}(m_0)$
electrons	-0.215	0.067	0.084
holes	-0.160	0.51	0.57

The calculated values of E1 and E2 for different values of l are shown in figure 5.22.

As can be seen, despite the fact that the same sized QDs were chosen at the beginning, the ground state emission energy is determined to be quite different for different interdiffusion lengths l . This means that the effective size of the QD is reduced by the interdiffusion process, which is reflected in the general blue-shift of the ground state emission energy for the calculated

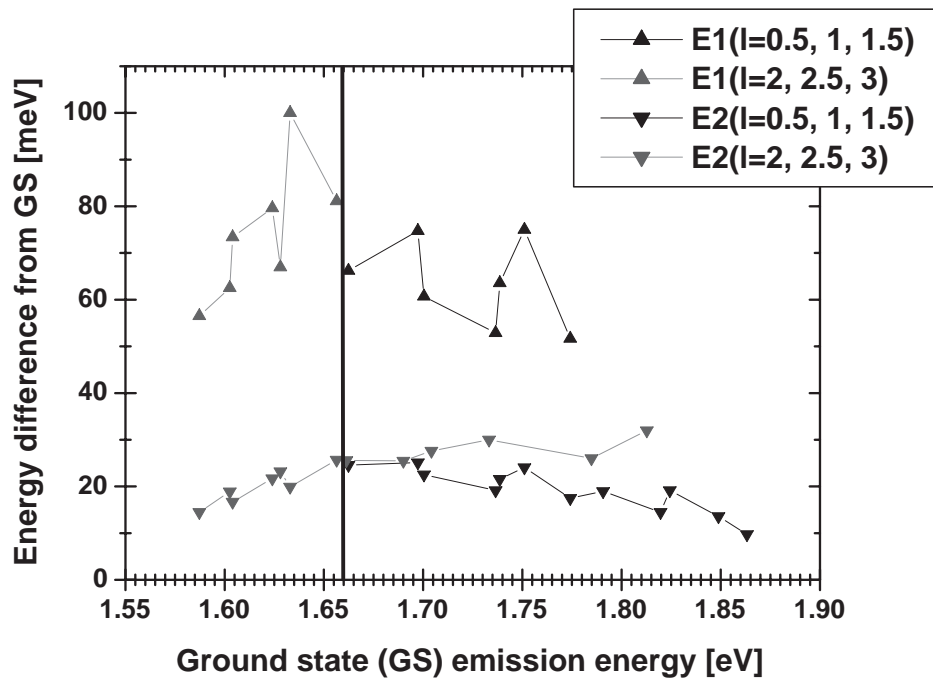


Figure 5.22: Calculated values of E1 and E2 for different values of l

values using larger values of l .

The effects of interdiffusion on the QD energy levels can be seen here, as the line drawn at a ground state emission of 1.660eV shows. At 1.660eV, the values of E2 are much the same for values of l around 1.0nm and 2.5nm. However, the values of E1 at 1.660eV are slightly different, with a difference of approximately 14.9meV.

From this difference in transition energies for different l values, albeit a small difference, the calculation results must be compared to the actual experimental data, and this is done in figure 5.23. From high pressure macroscopic PL spectra studies, the value of E2 is determined to be near the value of 24meV; thus the peaks spaced by nearly 24meV from the ground state emission energy are assigned here as the E2 transitions. These peaks are the group B peaks. From several single QD micro-PL spectra taken at high excitation intensity, the energy separations between the main peak (the ground state emission) and the peaks in group B are measured and plotted for the ground state emission. For the same ground state emission region, the calculated values of E2 when $l=0.5, 1.0, \text{ and } 1.5\text{nm}$, and when $l=2.0, 2.5, \text{ and } 3.0\text{nm}$ are also plotted. As can be seen, the calculations reproduce the experimental results quite well when $l=2, 2.5, \text{ and } 3\text{nm}$.

From figure 5.23, it is found that the values of l are close to 2.5nm. Using the values 2.0, 2.5, and 3.0nm for l , E1 and E2 are calculated, and are plotted with the experimentally determined values of E1 and E2 from several single QD micro-PL spectra taken at high excitation intensities. These are shown in figure 5.24.

The E1 values are between 70 and 80meV, and are in agreement with the expected value range of E1 as stated in chapter 4. It can be seen that both E1 and E2 are reproduced by calculations using values 2.0, 2.5, and 3.0nm for l . Thus, most QDs of this sample are expected to have an interdiffusion length l within this range. In chapter 2, the interdiffusion length l was set to $\sqrt{Dt} = l(T)$, where the interdiffusion length is dependent on annealing temperature. So far, all samples were post-annealed at the same temperature of 680°C for one hour. The value for $l(680^\circ\text{C})$ is in close agreement with that determined by Sanguinetti, et. al.[18], which is 2nm. Most importantly, it can be seen that a QD modeled by a cone with interdiffusion at the QD/barrier interface is a valid model for GaAs/AlGaAs QDs made by MDE. Conversely, it can be said that the actual shape of the buried GaAs QD is indeed close to that of a sphere with the interfaces blurred by interdiffusion, the length of which is determined to be distributed around 2.5nm.

The barrier line in figure 5.24 is the plot of the distance from the ground state emission to the AlGaAs barrier PL peak. It can also be seen that, although the value of E2 stays relatively constant, the value of E1 decreases

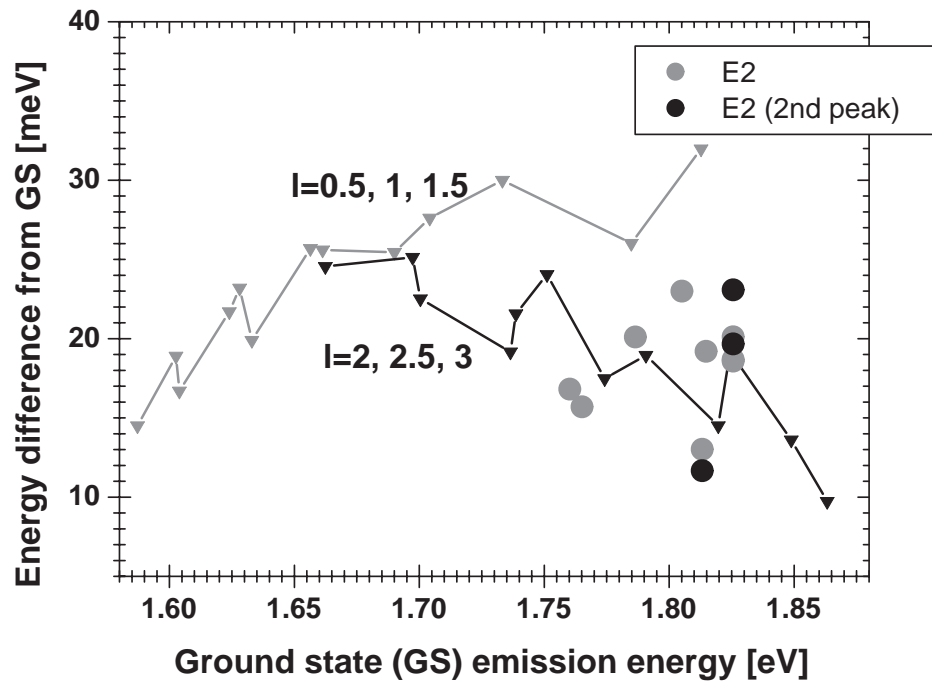


Figure 5.23: Experimental and calculated values of E2

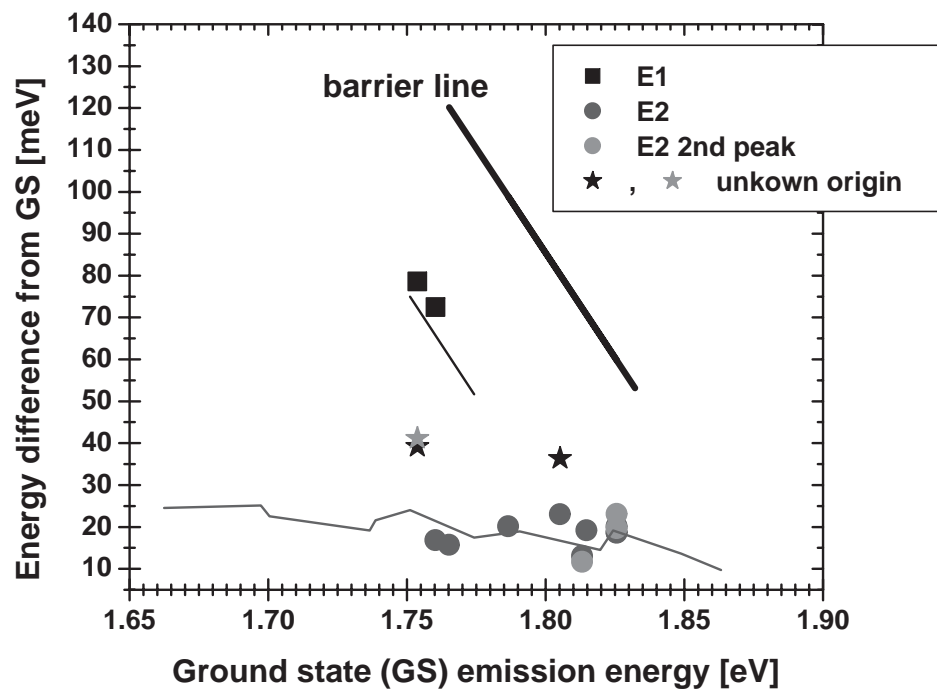


Figure 5.24: Experimental and calculated values of E1 and E2

as the ground state emission approaches the barrier. In fact, no E1 emission is observed for QD PL with a ground state emission higher than 1.77eV.

Physically, this is readily understood. As the ground state of the confined electron approaches the AlGaAs barrier, the first excited state of the confined electron is “pushed out” of the potential well. Thus, it may seem that there is no localized confinement of the first excited state electron when the ground state is close to the barrier. It will be shown later that this is not necessarily so. The hole does not experience the effect of the approaching of the barrier so strongly due to their heavier masses, and thus E2 does not change much as the ground state emission approaches the barrier energy.

Dipole forbidden recombination emission

So far, the E2 emission has been taken for granted, but in fact this emission is rather remarkable. This peak is of interest because an inter-band transition between carriers with different quantum numbers n , l , and m would normally be dipole forbidden. Thus, different recombination processes must exist. The emission from the recombination of a $n=1, l=0$ electron with an $n=2, l=0$ heavy hole has been reported to be theoretically possible due to the coupling between optically allowed and forbidden transitions induced by Coulomb interaction between electrons and holes[20, 21]. The reason why such an emission can be observed is considered in detail in the next subsection, where the theory of many-carrier correlations is discussed.

5.4.2 Many-carrier correlations in a GaAs QD

Here, in the theory of many-carrier correlations, the interaction between carriers in a QD are treated as perturbations to the single-carrier confinement energy levels. The arguments are restricted to uncharged QDs only, i.e. the number of electrons and holes in each QD are assumed to be equal. The energy levels of a QD can be calculated by solving Schrödinger’s equation $H\phi = E\phi$, where ϕ is the total wavefunction that describes all electrons and holes within the QD. The Hamiltonian for a multi-carrier system in a QD is given as

$$H = - \sum_{i \in [e]} \frac{\hbar^2}{2m_e} \nabla_i^2 - \sum_{i \in [h]} \frac{\hbar^2}{2m_h} \nabla_i^2 + \sum_{i \in [e]} V_e(\vec{r}_i) + \sum_{i \in [h]} V_h(\vec{r}_i) + \sum_{i,j \in [e,h]} \frac{q_i q_j}{4\pi\epsilon_0\epsilon_\infty |\vec{r}_i - \vec{r}_j|}, \quad (5.1)$$

where q_i and q_j are the carrier electrical charges, m_e and m_h are the electron and hole masses, respectively, $V_e(\vec{r}_i)$ and $V_h(\vec{r}_i)$ are the lattice potentials of the electrons and holes, respectively, \vec{r}_i and \vec{r}_j represent the carrier positions, ϵ_0 is the permittivity of vacuum, and ϵ_∞ is the dielectric constant of the material. This many-body problem is solved by using the Hartree-Fock approximation, where the total wavefunction ϕ is constructed by the linear combination of the single carrier wavefunctions. Electrons and holes are Fermions, thus their antisymmetry upon exchanging two electrons or holes must be maintained by writing ϕ as products of Slater determinants

$$\begin{aligned} \phi = & \frac{1}{\sqrt{N_e!}} \begin{vmatrix} \varphi_{e1\uparrow}(\vec{r}_1) & \cdots & \varphi_{eN_e\uparrow}(\vec{r}_1) \\ \vdots & \ddots & \vdots \\ \varphi_{e1\uparrow}(\vec{r}_{N_e}) & \cdots & \varphi_{eN_e\uparrow}(\vec{r}_{N_e}) \end{vmatrix} \times \frac{1}{\sqrt{N_e!}} \begin{vmatrix} \varphi_{e1\downarrow}(\vec{r}_1) & \cdots & \varphi_{eN_e\downarrow}(\vec{r}_1) \\ \vdots & \ddots & \vdots \\ \varphi_{e1\downarrow}(\vec{r}_{N_e}) & \cdots & \varphi_{eN_e\downarrow}(\vec{r}_{N_e}) \end{vmatrix} \\ & \times \frac{1}{\sqrt{N_h!}} \begin{vmatrix} \varphi_{h1\uparrow}(\vec{r}_1) & \cdots & \varphi_{hN_h\uparrow}(\vec{r}_1) \\ \vdots & \ddots & \vdots \\ \varphi_{h1\uparrow}(\vec{r}_{N_h}) & \cdots & \varphi_{hN_h\uparrow}(\vec{r}_{N_h}) \end{vmatrix} \times \frac{1}{\sqrt{N_h!}} \begin{vmatrix} \varphi_{h1\downarrow}(\vec{r}_1) & \cdots & \varphi_{hN_h\downarrow}(\vec{r}_1) \\ \vdots & \ddots & \vdots \\ \varphi_{h1\downarrow}(\vec{r}_{N_h}) & \cdots & \varphi_{hN_h\downarrow}(\vec{r}_{N_h}) \end{vmatrix}, \end{aligned} \quad (5.2)$$

where the determinants are separated into the spin-up (\uparrow) and spin-down (\downarrow) parts, N_e and N_h are the number of electrons and holes, respectively, and the single-carrier wavefunctions φ_i are chosen to be orthogonal, so that $\langle \varphi_i | \varphi_j \rangle = \delta_{ij}$.

In order to determine the various many-carrier interaction energies, the last term in equation 5.1 must be solved for the electron-electron (e-e), hole-hole (h-h), and electron-hole (e-h) interactions. The last term is treated as a first-order perturbation to the single-carrier energy levels. Due to the orthogonality of φ_i , the two-body operator $1/|\vec{r}_i - \vec{r}_j|$ takes a simple form when evaluated with the Hartree-Fock wavefunction defined in equation 5.2. The expectation value of the last term in equation 5.1 is

$$\begin{aligned} \langle \phi | \frac{1}{|\vec{r}_i - \vec{r}_j|} | \phi \rangle = & \int \int \varphi_{i,\sigma_i}^*(\vec{r}_{i,\sigma_i}) \varphi_{j,\sigma_j}^*(\vec{r}_{j,\sigma_j}) \frac{1}{|\vec{r}_{i,\sigma_i} - \vec{r}_{j,\sigma_j}|} \varphi_{i,\sigma_i}(\vec{r}_{i,\sigma_i}) \varphi_{j,\sigma_j}(\vec{r}_{j,\sigma_j}) d\vec{r}_{i,\sigma_i} d\vec{r}_{j,\sigma_j} \\ & - \int \int \varphi_{i,\sigma_i}^*(\vec{r}_{i,\sigma_i}) \varphi_{j,\sigma_j}^*(\vec{r}_{j,\sigma_j}) \frac{1}{|\vec{r}_{i,\sigma_i} - \vec{r}_{j,\sigma_j}|} \varphi_{i,\sigma_i}(\vec{r}_{j,\sigma_j}) \varphi_{j,\sigma_j}(\vec{r}_{i,\sigma_i}) d\vec{r}_{i,\sigma_i} d\vec{r}_{j,\sigma_j}. \end{aligned} \quad (5.3)$$

σ_i and σ_j represent the spin of the carriers. The first term in the right-hand side of equation 5.3 is the Coulomb interaction, and the second term is the

exchange interaction. The magnitude of these two interaction terms depend on the overlap of the carrier wavefunctions and their spins, and are calculated with the two-body operator V_{ij} in the last term of equation 5.1 expressed as

$$V_{ij} = \frac{q_i q_j}{4\pi\epsilon_0\epsilon_\infty |\vec{r}_i - \vec{r}_j|} \equiv g(\vec{r}_i, \sigma_i, \vec{r}_j, \sigma_j). \quad (5.4)$$

Coulomb and exchange terms apply to e-e, h-h, and e-h interactions, and for exchange terms, spin must also be taken into account.

For practical reasons, the following analyses are limited to a non-degenerate QD with two confinement levels and an occupation of up to four excitons. The possible recombinations of ground-state, anti-parallel electron-hole pairs with the various “spectator”, or non-recombining carriers in the same QD and their spins are listed in figure 5.25.

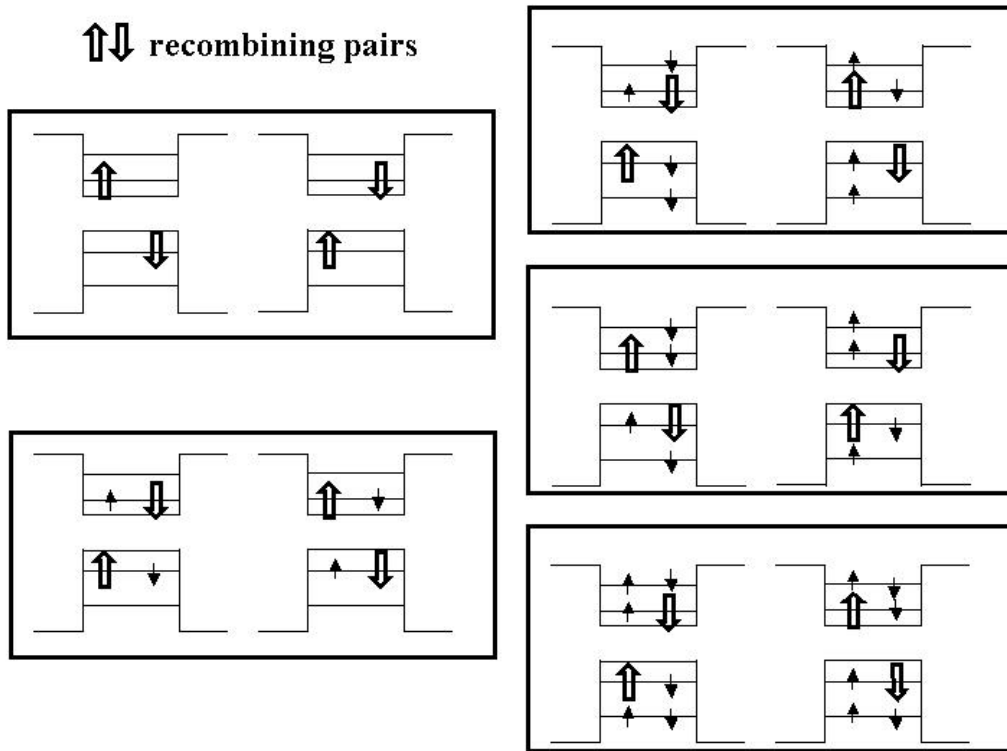


Figure 5.25: The possible recombinations of ground-state carriers with various “spectator” carriers in the same QD

Here, we consider the wavefunctions of the single carriers which construct the Slater determinant of equation 5.2. Despite the detailed model of the QD which was chosen for the energy level calculations, here a cubic QD with im-

penetrable walls is chosen. This simple model is used to establish the electron and hole interaction energies relationship to QD size. Indeed, it has been reported that the exchange interaction energy does not depend sensitively on the assumed shape of the QD[22]. The cube dimensions are taken to be (s,s,s) , and the quantum numbers in the x -, y -, and z -directions are indicated with n_x , n_y , and n_z (1,2,3,...). The corresponding electron and hole wavefunctions are described as

$$\varphi_i = u_{i,b,\vec{k}=0}(\vec{r})\varphi_i^{n_x n_y n_z}(\vec{r}) = u_{i,b,\vec{k}=0}(\vec{r})\sqrt{\frac{8}{s^3}}\sin\left(\frac{n_x\pi}{s}x\right)\sin\left(\frac{n_y\pi}{s}y\right)\sin\left(\frac{n_z\pi}{s}z\right), \quad (5.5)$$

with $\vec{r} = x, y, z \in [0\dots s]$. $u_{i,b,\vec{k}=0}(\vec{r})$ is the part of the Bloch function with the same periodicity as that of the lattice, and i denotes the carrier, b denotes the band (C is the conduction band, and V is the valence band), and the wavevector \vec{k} is taken to be 0 in the effective mass approximation. Here, in the idealized QD with impenetrable walls, the envelope wavefunctions are independent of the electron and hole effective masses, and both the electron and the hole with the same quantum numbers $(n_x n_y n_z)$ are described by the same envelope wavefunction.

Coulomb interaction energy

The Coulomb interaction energy does not depend on the spin of the carriers, and will not be included in the arguments in this subsection. The recombination energies that can be observed in a PL experiment are determined by subtracting the calculated final state energy from the calculated initial state energy. Here, the e-h Coulomb interaction energy can be written as

$$\langle \varphi_e^{111} \varphi_h^{111} | g | \varphi_e^{111} \varphi_h^{111} \rangle \equiv -\Delta, \quad (5.6)$$

where the Bloch terms have taken out of the integral and integrated separately by the slowly varying envelope approximation (SVEA)[23]. Due to the fact that $\varphi_e^{n_x n_y n_z} = \varphi_h^{n_x n_y n_z}$, the following relations for the e-e, h-h and e-h Coulomb interaction energy hold:

$$\begin{aligned} \langle \varphi_e^{111} \varphi_e^{111} | g | \varphi_e^{111} \varphi_e^{111} \rangle &= \langle \varphi_h^{111} \varphi_h^{111} | g | \varphi_h^{111} \varphi_h^{111} \rangle = -\langle \varphi_e^{111} \varphi_h^{111} | g | \varphi_e^{111} \varphi_h^{111} \rangle \\ & \quad (5.7) \\ \langle \varphi_e^{111} \varphi_e^{211} | g | \varphi_e^{111} \varphi_e^{211} \rangle &= \langle \varphi_h^{111} \varphi_h^{211} | g | \varphi_h^{111} \varphi_h^{211} \rangle = -\langle \varphi_e^{111} \varphi_h^{211} | g | \varphi_e^{111} \varphi_h^{211} \rangle \\ &= -\langle \varphi_e^{211} \varphi_h^{111} | g | \varphi_e^{211} \varphi_h^{111} \rangle \end{aligned}$$

$$\equiv -\Delta' \quad (5.8)$$

$$\begin{aligned} \langle \varphi_e^{211} \varphi_e^{211} | g | \varphi_e^{211} \varphi_e^{211} \rangle &= \langle \varphi_h^{211} \varphi_h^{211} | g | \varphi_h^{211} \varphi_h^{211} \rangle = -\langle \varphi_e^{211} \varphi_h^{211} | g | \varphi_e^{211} \varphi_h^{211} \rangle \\ &\equiv -\Delta''. \end{aligned} \quad (5.9)$$

By calculating the Coulomb interaction energy using the above equations for all the carriers in the QD before and after the recombining pairs annihilate and emit a photon, the Coulomb interaction contribution to the total recombination energies can be determined. This is done for all the possible cases listed in figure 5.25. Surprisingly, the result is that, regardless of the number and arrangement of the “spectator” carriers, the net Coulomb interaction contribution to all the possible recombination energies is always $-\Delta$. Although the actual value of Δ will not be calculated here, the conclusion is that the observed single QD recombination energies are shifted due only to the e-e, h-h, and e-h exchange interaction energies, which are all offset by $-\Delta$. Since the ground state excitonic recombination emission is also offset by $-\Delta$, the effects of Coulombic interaction do not appear in the ground state recombination spectra. The e-e, h-h, and e-h exchange interaction energies will be calculated and compared to the experimental data later in this chapter.

Dipole forbidden emission and Coulombic interactions

The origin of the E2 emission is determined from the effective mass calculations in the previous subsection. The E2 emission is normally a dipole forbidden emission in bulk crystals. The reason why such a forbidden emission is so clearly visible in QDs is due to the level coupling induced by Coulomb interactions resulting in a transfer of oscillator strength to the lower energy excitations. Specifically, the electron-hole Coulomb coupling occurs between the optically allowed exciton transition (GS) and the optically forbidden one (E2)[24], making the optical dipole matrix element for the E2 exciton nonzero, i.e. the Bloch terms contribute to the optical dipole integration, while the envelope wavefunctions are integrated separately, and due to the coupling-induced modifications to the (E2 exciton) envelope wavefunctions, this factor is nonzero. Thus, such an emission is observable.

Exchange interaction energy

The exchange interaction energy applies to the e-e, h-h, and e-h pairs with parallel spins. The exchange interaction energy is always zero for carrier pairs with anti-parallel spin.

Here, the e-e pair exchange interaction energy is equal to a , the h-h pair exchange interaction energy is equal to b , and exchange interaction energy for the electron-hole pair with same n -numbers is equal to c . This is shown in the upper-left hand side inset in figure 5.26. In this case, a is always less than b , due to the fact that the confinement energies of the electron and hole are different; the confined electron envelope wavefunction is more spread out in space compared to that of the hole, thus their exchange interaction energies are different. The more tightly confined holes have a stronger exchange interaction energy than the electrons.

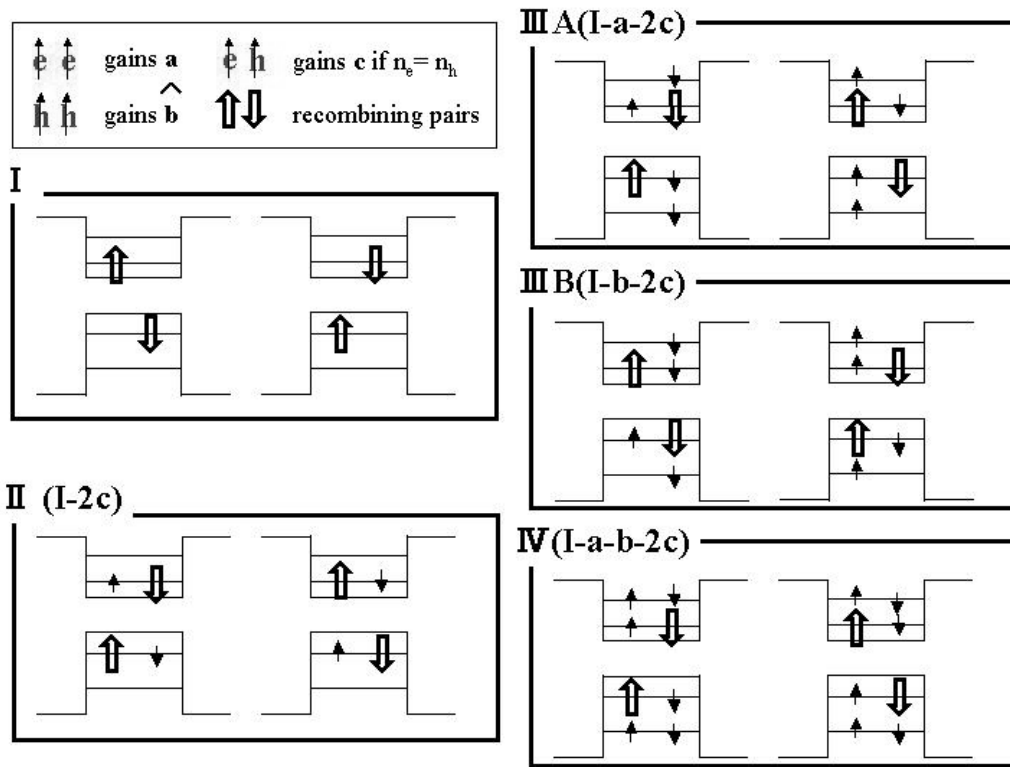


Figure 5.26: The possible recombinations of ground-state carriers with various “spectator” carriers in the same QD

By calculating the exchange interaction energy using the above values (a, b, c) for all the carriers in the QD before and after the recombining pairs

annihilate and emit a photon, the exchange interaction contribution to the total recombination energies can be determined. This is done for all the possible cases listed in figure 5.26, and are written for each of the five cases in the upper-left corner of each box.

At this point, it is necessary to compare these calculations to the actual experimental results. As pointed out earlier, the numbering of the peaks in figure 5.17 are so chosen to correspond to the possible recombination schemes of figure 5.26; the peak assignment corresponds to the recombination process, and differ in energy by the amount written in each of the boxes in figure 5.26. Also, as pointed out in the study of figure 5.21, peak I is related to a single exciton recombination; peak II is biexcitonic in nature, and peak IIIB is triexcitonic in nature. This is in agreement with the possible recombinations listed in figure 5.26.

The establishment of the e-h exchange interaction energy's relationship to QD size will be done by considering only short-range interactions, and assuming that the exchange energy can be calculated by evaluating the probability of finding the carriers at the same site[25, 26, 27, 28, 30]. Here, a cubic QD is again assumed, and the QD size is determined directly from the ground state emission energy. The Coulomb interaction energy will be ignored in the following calculations.

The electron-hole exchange interaction energy c is given as

$$c = E_x \pi a_x^3 E_0 \quad (5.10)$$

from references [25, 29, 30]. Here, E_x is the exchange energy of the $1s$ bulk exciton, which is reported to be $20\mu\text{eV}$ for GaAs[22], and a_x is the Bohr radius of the bulk $1s$ exciton, which is reported to be 11.2nm for GaAs[31]. E_0 is given as

$$E_0 = \int \int \int |\varphi_e \varphi_h|^2 dx dy dz = \frac{27}{64} \frac{1}{(s/2)^3}. \quad (5.11)$$

The Bloch terms are not included in equation 5.11, but they are included in the exchange integral; thus the orthogonal Bloch terms belonging to different bands give non-zero contributions. The Bloch term exchange integral is the bulk e-h exchange interaction energy. It is possible to establish the relationship between QD size and e-h exchange interaction energy. As stated above, the value of s , or the size of the cubic QD, is determined directly from the ground state emission. In a cubic QD, the electron ground state confinement energy is given from equation 1.1 as

$$\Delta E_e^{111}(s) = \frac{3\pi^2 \hbar^2}{2m_e^* s^2} \quad (5.12)$$

and the hole ground state confinement energy is given likewise as

$$\Delta E_h^{111}(s) = \frac{3\pi^2\hbar^2}{2m_h^*s^2}. \quad (5.13)$$

Thus, the ground state emission energy E_{PL} can be written as a function of the size of the cubic QD s as

$$E_{PL} = E_{GaAs} + \Delta E_e^{111}(s) + \Delta E_h^{111}(s) \quad (5.14)$$

where E_{GaAs} is the bandgap of bulk GaAs with a value of 1.51eV. From equation 5.10, the ground state emission energy E_{PL} can be related to c via s . The relationship of c to E_{PL} is $c \propto E_{PL}^{3/2}$. Thus, an increase in c with E_{PL} can be expected.

The theoretical calculations of c based on the QD ground state emission energy is plotted, along with the actual values of c determined from the I-II peak spacing of single QD PL spectra using the relation written in figure 5.26. The results are shown in figure 5.27.

A good fit to the data is seen. Both data and theory point out that as the size s of the QD decreases, the e-h exchange interaction energy increases. This shows the strong enhancement of the e-h exchange interaction by the increased three dimensional confinement in the QD's as the size of the QD is decreased and the e-h envelope wavefunctions' spatial overlap is increased. The error bar is determined from the resolution of the spectrometer, but is expected to be larger than $132\mu\text{eV}$, due to errors in the peak fitting process, etc.

Next, the e-e and h-h exchange interaction energies will be considered. Due to Pauli's principle, only two carriers of same charge and opposite spin can occupy any energy level. Since a two confinement level QD is considered here, the same-spin e-e and h-h pairs are always in different energy levels. This is not necessarily so for e-h pairs, however. Thus, in the cubic QD model, the e-e and h-h exchange interaction energy will always take the following form (assuming φ_e and φ_h have the same envelope wavefunction):

$$a = b = \langle \varphi_e^{211} \varphi_e^{111} | g | \varphi_e^{111} \varphi_e^{211} \rangle. \quad (5.15)$$

The e-e pair exchange interaction energy is equal to the h-h pair exchange interaction energy due to the fact that the electron and hole have the same envelope wavefunctions here. This is due to the impenetrable QD walls adopted in this case, and do not precisely reflect the actual situation. However, the experimental value of a is almost equal to b , as can be seen in the next figure which shows the experimental values of a and b determined from the I-IIIA and I-IIIB peak spacings of single QD PL spectra using the

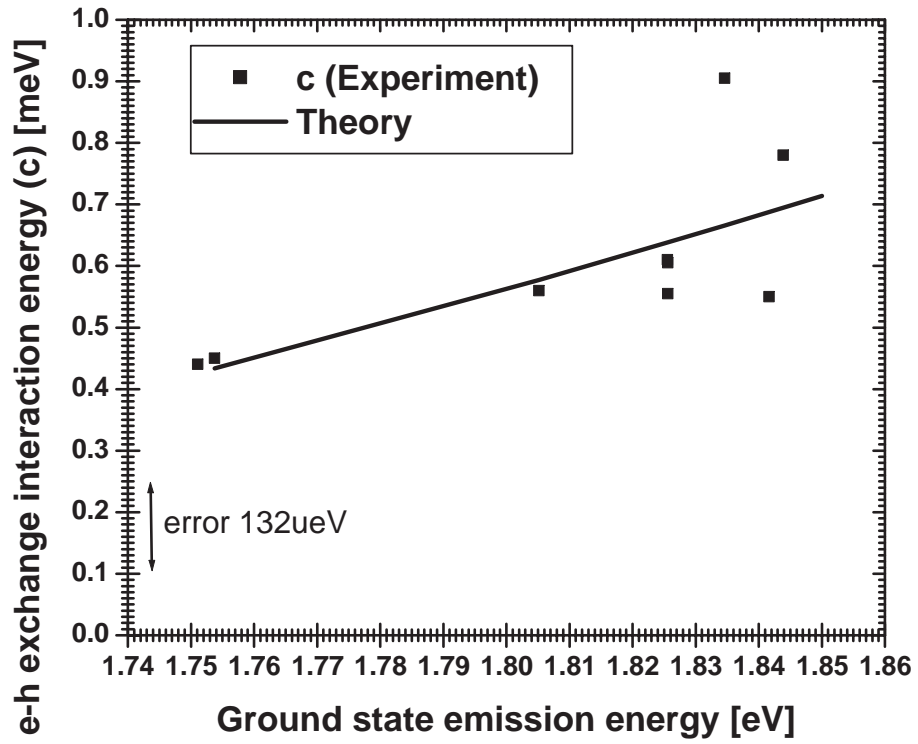


Figure 5.27: Experimental plot of e-h exchange interaction energy (c)

relation written in figure 5.26. The results are shown in figure 5.28. The use

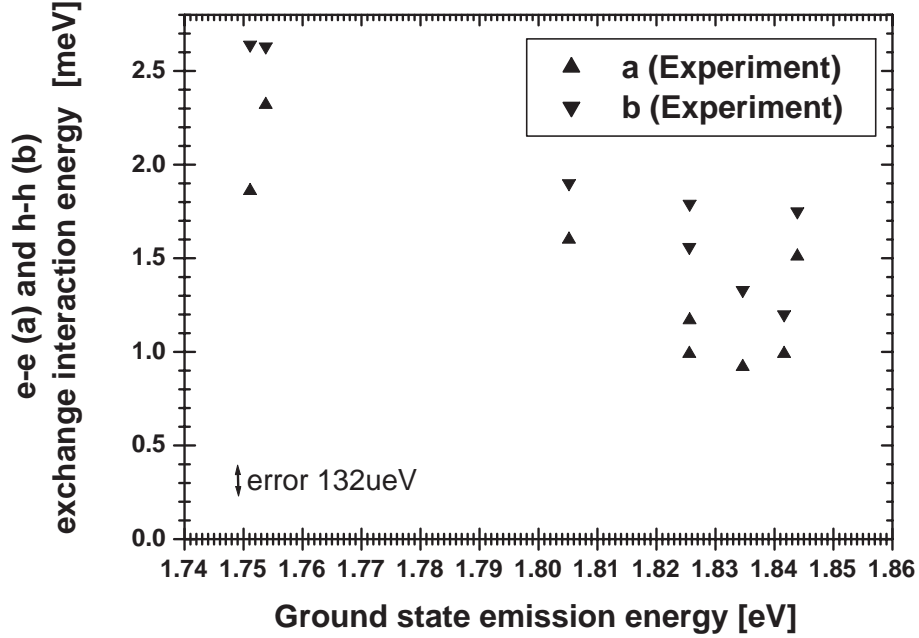


Figure 5.28: Plot of the experimentally determined e-e (a) and h-h (b) exchange interaction energies

of the same envelope wavefunction to describe both the electron and the hole is thus justified, as the values of a and b are almost equivalent for all QDs studied here. At the same time, the supposition that $a < b$ is also seen to be correct. From figure 5.28, it can be seen that the e-e and h-h exchange interaction energies tend to decrease with decreasing s . This can be understood physically as the same carrier envelope wavefunctions having lesser spatial overlap as the same spin electrons/holes tend to push each other away in smaller QDs.

The validity of the relationships between the various carrier exchange interaction energies to the peak spacings, shown in figure 5.26, is evaluated by comparing the $a, b,$ and c values to the actual I-IV peak spacing. As is noted in figure 5.26, the I-IV peak spacing is equal to $a+b+2 \times c$. This is calculated using the experimentally obtained values of $a, b,$ and c , and are compared to the I-IV peak spacing in figure 5.29. Here, only single QD PL spectra in which peaks I to IV are all visible are taken into consideration.

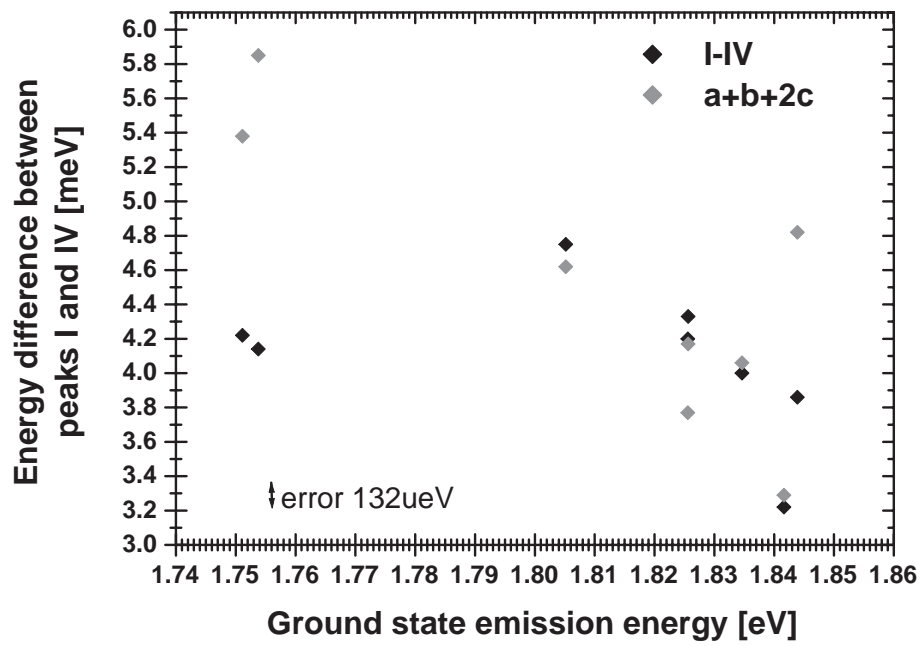


Figure 5.29: Plot of the I-IV peak energy difference and $a+b+4 \times c$

Single QD PL spectra in which peak IV is not observed have been obtained, but are not considered in the current theoretical picture. Extra effects of unknown origin are considered to take place in these QDs.

The good match between the I-IV peak energy difference and $a+b+2\times c$ reflects the validity of the relationships described in figure 5.26. Thus, although the a , b , and c values have not been determined numerically here, their values as shown in figures 5.27 and 5.28 must probably be correct.

The deviation of the I-IV peak energy difference from the $a+b+2\times c$ value at lower ground state emission energies is most probably due to the existence of a third confinement level with an occupation of up to six excitons; the introduction of a third confinement level provides an “escape route” for the same spin carriers, i.e. it allows the same spin electrons/holes to exist in the same QD with less spatial overlap. Thus, a decrease in the actual exchange interaction is seen.

Conclusions

The broadband spectra of a single GaAs/AlGaAs QD made by MDE is observed for the first time, and the sharp spectral lines from a single QD spectra are resolved.

Initially, a mask combined with a diffraction-limited microscope is used to verify the spectral characteristics of the single QD spectrum. From this, it is found that single QD spectroscopy is possible using the micro-PL method with or without a mask, and so single QD spectra taken without a mask are studied in detail.

From the excitation intensity dependence of the broadband spectra of a single QD, the various spectral lines in the single QD spectra are assigned to the energy levels and multi-carrier correlations within the QD. These results are compared to the effective mass approximation calculations of the previous chapter, and good agreement between data and theory is seen.

Dipole forbidden recombinations are seen in the broadband spectra of a single QD, which occur due to many-body Coulomb interactions in the QD.

From the fine structure near the ground state energy level, multi-carrier energy renormalizations of the ground state energy level are observed. Coulomb interactions do not make themselves apparent in the renormalized spectra, but the e-e, h-h, and e-h interaction correlations can be determined from the renormalized spectra. This is possible due to the fact that the electron and hole envelope wavefunctions keep the symmetry of the crystal due to the lack of strain in the QD, and are easily analyzed because there are no wetting layer-confined carriers, making the carrier interactions picture much simpler. Thus, GaAs/AlGaAs QDs made by MDE are, in this sense, ideal

QDs.

Furthermore, a study of the transient PL spectra shows a similar spectral structure for a GaAs QD made by MDE [32], and their origin is explained by the interactions of multiple carriers in the QD. Thus, it is safe to consider that the multiple-carrier interactions are responsible for the fine structures.

e-e and h-h exchange interaction energies are determined to decrease with the decrease in QD size, while the e-h exchange interaction energy is determined to increase with the decrease in QD size.

Earlier in this section, it has been stated that no E1 emission has been observed for QDs with ground state emission energies above 1.77eV. This does not mean, however, that there are no $n=1, l=1$ states for QDs with ground state energies near the AlGaAs barrier bandgap; from the validity of the two confinement level, multi-excitonic line analysis in this section, it can be seen that the $n=1, l=1$ state (or the (211) state for cubic QDs) does exist for QDs with ground state emissions close to the barrier bandgap.

The cylindrical symmetry of the QD is assumed, and the agreement with theoretical calculations using cylindrical symmetry make the QD model adopted here legitimate. In the next chapter, the effects of QD shape anisotropy and the effects of exchange interactions as well as the reduction in symmetry on the QD carrier confinement will be studied using QWR-like QDs.

Bibliography

- [1] Kümmell, T., Weigand, R., Bacher, G., Forchel, A., Leonardi, K., Hommel, D., Selke, H., *Single zero-dimensional excitons in CdSe/ZnSe nanostructures*, Appl. Phys. Lett. **73**, 3105 (1998)
- [2] Marzin, J.-Y., Gérard, J.-M., Izraël, A., Barrier, D., Bastard, G., *Photoluminescence of single InAs quantum dots obtained by self-organized growth on GaAs*, Phys. Rev. Lett. **73**, 716 (1994)
- [3] Rambach, M., Seufert, J., Obert, M., Bacher, G., Forchel, A., Leonardi, K., Passow, T., Hommel, D., *Excitation spectroscopy on single quantum dots and single pairs of quantum dots*, Phys. Stat. Sol. **229**, 503 (2002)
- [4] Seufert, J., Obert, M., Bacher, G., Forchel, A., Passow, T., Leonardi, K., Hommel, D., *Tunneling of zero-dimensional excitons in a single pair of correlated quantum dots*, Phys. Rev. B **64**, 121303 (2001)
- [5] Gammon, D., Snow, E. S., Katzer, D. S., *Excited state spectroscopy of excitons in single quantum dots*, Appl. Phys. Lett. **67**, 2391 (1995)
- [6] Gammon, D., Snow, E. S., Shanabrook, B. V., Katzer, D. S., Park, D., *Fine structure splitting in the optical spectra of single GaAs quantum dots*, Phys. Rev. Lett. **76**, 3005 (1996)
- [7] Hessman, D., Castrillo, P., Pistol, M.-E., Pryor, C., Samuelson, L., *Excited states of individual quantum dots studied by photoluminescence spectroscopy*, Appl. Phys. Lett. **69**, 749 (1996)
- [8] Nikitin, V., Crowell, P. A., Gupta, J. A., Awschalom, D. D., Flack, F., Samarth, N., *Zero-dimensional excitonic confinement in locally strained $Zn_{1-x}Cd_xSe$ quantum wells*, Appl. Phys. Lett. **71**, 1213 (1997)
- [9] Zrenner, A., Butov, L. V., Hagn, M., Abstreiter, G., Böhm, G., Weimann, G., *Quantum dots formed by interface fluctuations in AlAs/GaAs coupled quantum well structures*, Phys. Rev. Lett. **72**, 3382 (1994)

- [10] Hess, H. F., Betzig, E., Harris, T. D., Pfeiffer, L. N., West, K. W., *Near-field spectroscopy of the quantum constituents of a luminescent system*, Science **264**, 1740 (1994)
- [11] Robinson, L. M., Rho, H., Kim, J. C., Jackson, H. E., Smith, L. M., Lee, S., Dobrowolska, M., Furdyna, J. K., *Quantum dot exciton dynamics through a nanoaperture: Evidence for two confined states*, Phys. Rev. Lett. **83**, 2797 (1999)
- [12] Yoshita, M., Sasaki, T., Baba, M., Akiyama, H., *Application of solid immersion lens to high-spatial resolution photoluminescence imaging of GaAs quantum wells at low temperatures*, Appl. Phys. Lett. **73**, 635 (1998)
- [13] Zwiller, V., Blom, H., Jonsson, P., Panev, N., Jeppesen, S., Tsegaye, T., Goobar, E., Pistol, M.-E., Samuelson, L., Björk, G., *Single quantum dots emit single photons at a time: Antibunching experiments*, Appl. Phys. Lett. **78**, 2476 (2001)
- [14] Lewis, A., Isaacson, M., Harootunian, A., Muray, A., *Development of a 500Å spatial resolution microscope*, Ultramicroscopy **13**, 227 (1984)
- [15] Park, D., Marrian, C. R. K., Gammon, D., Bass, R., Isaacson, P., Snow, E., *Small aperture fabrication for single quantum dot spectroscopy*, J. Vac. Sci. Technol. B **16**, 3891 (1998)
- [16] Kann, J. L., Milster, T. D., Froehlich, F., Ziolkowski, W., Judkins, J., *Numerical analysis of a two-dimensional near-field probe*, Ultramicroscopy **57**, 251 (1995)
- [17] Rossi, D., *FDTD2D*, SAL (Scientific Applications on Linux) <http://sal.duth.gr/Z/1/FDTD2D.html>
- [18] Sanguinetti, S., Watanabe, K., Kuroda, T., Minami, F., Gotoh, Y., Koguchi, N., *Effects of post-growth annealing on the optical properties of self-assembled GaAs/AlGaAs quantum dots*, J. Cryst. Growth **242**, 321 (2002)
- [19] Ioffe Physico-Technical Institute, *NSM Archive - Aluminium Gallium Arsenide (AlGaAs) - Basic Parameters*, Ioffe Physico-Technical Institute Electronic Archive <http://www.ioffe.rssi.ru/SVA/NSM/Semicond/AlGaAs/basic.html>

- [20] Hohenester, U., Di Felice, R., Molinari, E., Rossi, F., *Optical spectra of nitride quantum dots: Quantum confinement and electron-hole coupling*, Appl. Phys. Lett. **75**, 3449 (1999)
- [21] Hohenester, U., Molinari, E., *Role of coulomb correlations in the optical spectra of semiconductor quantum dots*, Phys. Stat. Sol. (b) **221**, 19 (2000)
- [22] Bayer, M., Forchel, A., Gorbunov, A., Timofeev, V. B., Schäfer, Reithmaier, J. P., *Electron and hole g factors and exchange interaction from studies of the exciton fine structure in $In_{0.60}Ga_{0.40}As$ quantum dots*, Phys. Rev. Lett. **82**, 1748 (1999)
- [23] Barenco, A., Dupertuis, M. A., *Quantum many-body states of excitons in a small quantum dot*, Phys. Rev. B **52**, 2766 (1995)
- [24] Hohenester, U., Molinari, E., *Excitonic and biexcitonic states in semiconductor quantum dots*, Phys. Stat. Sol. (a) **178**, 277 (2000)
- [25] Romestain, R., Fishman, G., *Excitonic wave function, correlation energy, exchange energy, and oscillator strength in a cubic quantum dot*, Phys. Rev. B **49**, 1774 (1994)
- [26] Takagahara, T., *Effects of dielectric confinement and electron-hole exchange interaction on excitonic states in semiconductor quantum dots*, Phys. Rev. B **47**, 4569 (1993)
- [27] Chen, Y., Gil, B., Lefebvre, P., Mathieu, H., *Exchange effects on excitons in quantum wells*, Phys. Rev. B **37**, 6429 (1988)
- [28] Thomas, D. G., Hopfield, J. J., *Optical properties of bound exciton complexes in cadmium sulfide*, Phys. Rev. **128**, 2135 (1962)
- [29] Elliott, R. J. (edited by Kuper, C. G., and Whitfield, G. D.), *Polarons and Excitons*, Oliver and Boyd Edinburgh (1963)
- [30] Henry, C. H., Faulkner, R. A., Nassau, K., *Donor-acceptor pair lines in cadmium sulfide*, Phys. Rev. **183**, 798 (1969)
- [31] Yu, P. Y., Cardona, M., *Fundamentals of Semiconductors 3rd Edition*, Springer Berlin (2001)
- [32] Kuroda, T., Sanguinetti, S., Gurioli, M., Watanabe, K., Minami, F., Koguchi, N., *Picosecond nonlinear relaxation of photoinjected carriers in a single $GaAs/Al_{0.3}Ga_{0.7}As$ quantum dot*, Phys. Rev. B **66**, 121302(R)1 (2002)

Chapter 6

QWR-like GaAs QDs

6.1 Introduction

Single GaAs/AlGaAs QDs with highly anisotropic shapes are studied using micro-PL. Here, the shape of the QD under investigation departs from that of the QDs studied in the previous chapter to that of a QWR-like shape. The difference in shape is expected to give a different confinement potential and different carrier correlation effects from those of the QD in the previous chapter.

The shift of very sharp luminescence lines in GaAs/AlGaAs QWR-like QDs at increasing excitation density is seen. These sharp lines correspond to the recombination of one dimensional excitons localized in a highly anisotropic-shaped QD. The evolution of the fine-structured photoluminescence spectra with increasing exciton density is interpreted in terms of many-body effects which lead to an increase of the exciton self-energy and to the formation of excitonic complexes.

6.2 Experimental setup

6.2.1 GaAs/Al_{0.405}Ga_{0.595}As sample

The sample used here has a higher Al content in the barrier than the GaAs/Al_{0.256}Ga_{0.744}As QD sample used in the previous chapter. Although the Ga droplet formation conditions are the same as those of the sample used in the GaAs/Al_{0.256}Ga_{0.744}As QD sample, a QWR-like QD was formed instead of a pyramidal QD, judging from the sample's shift of the luminescence lines with excitation intensity, as well as the high anisotropy of the PL spectrum. The effects of the barrier's Al content on the QD shape is unknown, however the

slight difference in the time between droplet formation and crystallization most probably played an important role in the definition of the QD shape. This is an issue which requires further inspection.

6.2.2 micro-PL

In the micro-PL measurements, essentially the same setup as that in chapter 5 is used (see figure 5.2). Additional features include a superconducting magnet with the center of its field at the sample, and a quarter-wave plate and a linear polarizer which are placed in front of the monochromator slit. The magnetic field can be increased up to 5T, making it possible to study the magneto-micro-PL spectra. Standard excitation intensity dependence is also studied at zero magnetic field and the quarter-wave plate and the linear polarizer removed. Finally, the polarization of the PL is also studied with a linear polarizer placed in front of the monochromator slit.

The same method used in chapter 5 is employed to check if the observed spectra is from a single QD or not. Thus, all the following results are from single QWR-like QD spectra.

6.3 Results

6.3.1 Zeeman splitting

The Zeeman splitting of the exciton confined in the QWR-like QD, deduced from the σ^+ - and σ^- -polarized, single QWR-like QD micro-PL peaks' positions at 5T, was negligible, and it can be said that the confinement effects of the anisotropic confinement potential is stronger than the confinement induced by the magnetic field. This reflects the strong anisotropy of the QD.

6.3.2 Excitation intensity dependence

An example of the single QWR-like QD micro-PL spectrum-excitation intensity dependence is shown in figure 6.1. The intensity is shown in the logarithmic scale, in order to emphasize the peaks with small intensities. The spectra are vertically offset for clarity. These spectra are taken at 10K, with 0.1meV monochromator resolution.

Fine structured PL spectra evolution with increasing excitation intensity is seen, similar to that of the QD's studied in chapter 5. A distinct difference is seen in the peak positions with increasing excitation intensity, a phenomenon not seen in the QDs studied in chapter 5. In the QDs studied

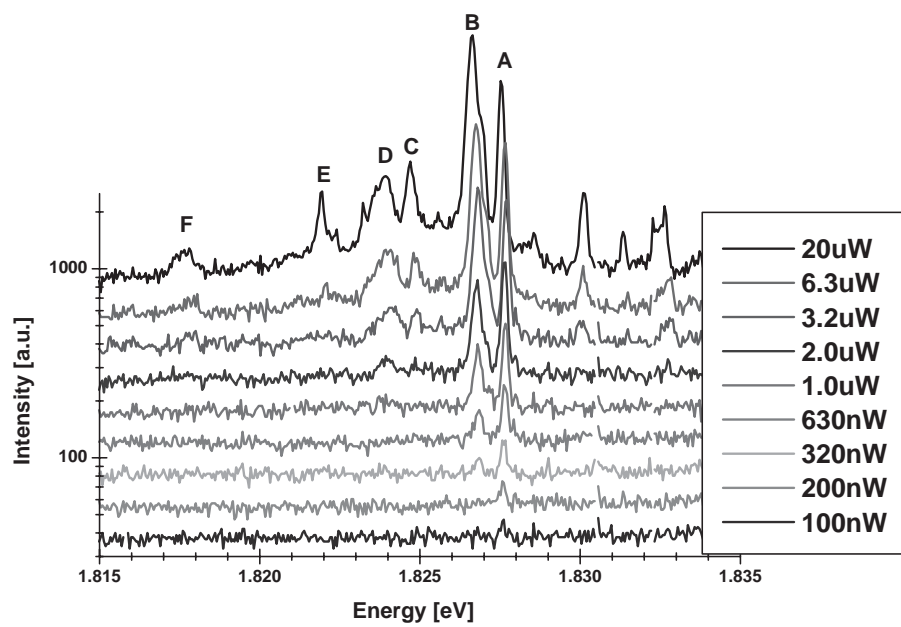


Figure 6.1: Single QWR-like QD micro-PL spectrum excitation intensity dependence

in chapter 5, no shift of the spectral lines are seen with increasing excitation intensity; in the QWR-like QDs, however, a clear shift of the spectral lines are seen with increasing excitation intensity. To clarify this shift, the amount of shift relative to the peak position as it initially appears is plotted against the excitation intensity in figure 6.2. The separate peaks are labeled in figure 6.1.

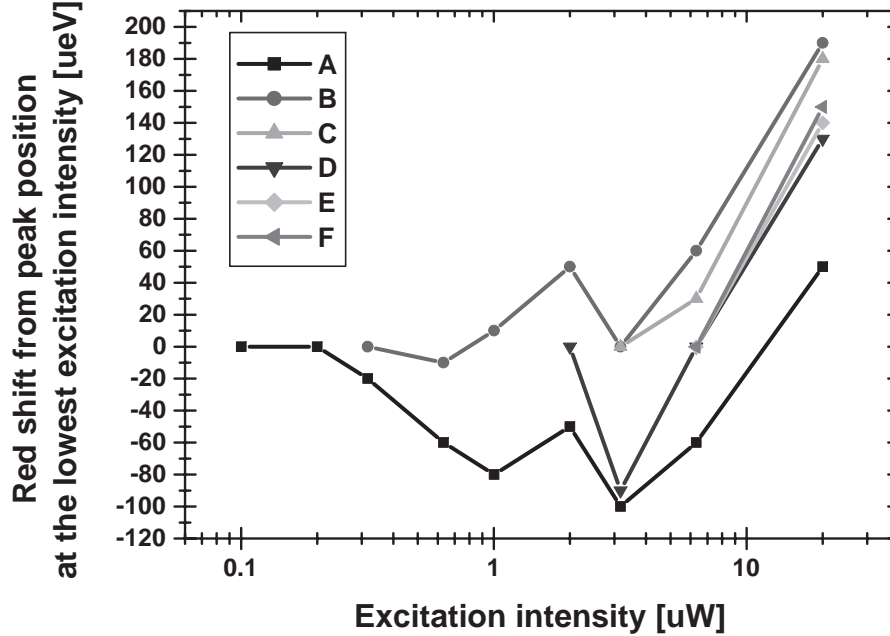


Figure 6.2: Energy shift relative to the peak position as it initially appears (a positive value indicates a red shift)

An initial blue shift of approximately $100\mu\text{eV}$ is seen for the main peak, and with higher increasing excitation intensity, an overall red shift of approximately $100\mu\text{eV}$ is seen. The initial blue shift most probably results from the mutual exciton-exciton interactions in the dense limit, leading to a renormalization of the exciton self-energy[1, 2]. Here, the sample is still in an electronically highly excited state, but with the electron-hole pairs in the form of a dense gas of excitons. However, this long-range direct Coulomb correlations of a given exciton with other neutral bound pairs, which correspond to the usual van der Waals attraction in an exciton gas, are very small effects that even in three dimensions are dominated by the short-range

exchange effects. These short range exchange effects, or the repulsion due to Pauli's exclusion principle, dominates the "screening" which is responsible for the red shift[3]. In bulk semiconductors, these two effects cancel each other out exactly, and a constant exciton recombination energy at increasing exciton density is expected[4]. In this case, the initial blue shift is a manifestation of the one dimensional nature of the linearly-aligned excitons in these QWR-like QDs[2, 5]. The existence of a permanent dipole between an electron and a hole in their ground state, which is caused by the asymmetric confinement potential inherent to the shape of the QWR-like QD, cannot be ignored. To summarize, these shifts are ascribed to a lack of balance between van der Waals attractive forces and repulsion due to Pauli's exclusion principle in an exciton gas, caused by the asymmetric shape of the confinement potential.

6.3.3 PL polarization

The polarization of the PL is studied using a linear polarizer placed in front of the monochromator slit. This simple setup is used, because the polarization of the excitation light is not selected. The spectral dependence on the observed linear polarization is shown in figure 6.3. The angle of the linear polarizer is determined by rotating the polarizer and taking the angle which produces the largest observable change as 90° , and then taking the spectra while rotating the polarizer by 30° .

From figure 6.3, it can be seen that the shift originate from a combination of two perpendicularly polarized PL directions. Thus, the PL spectra from this QWR-like QD consists of two perpendicular spectral components which most likely correspond in direction to the $\langle 110 \rangle$ and $\langle 1\bar{1}0 \rangle$ directions of the sample surface.

Figure 6.4 shows the spectral peak intensity dependence on the observed linear polarization. From this it is clear that the peak labeled "B" consists of two discrete peaks, which are mostly overlapped by a component of stronger intensity, resulting in a broader peak.

These results show the anisotropy of the confinement potential, which gives a different spectra for different confinement directions. This is a result of the lifting of the degeneracy in the confinement directions.

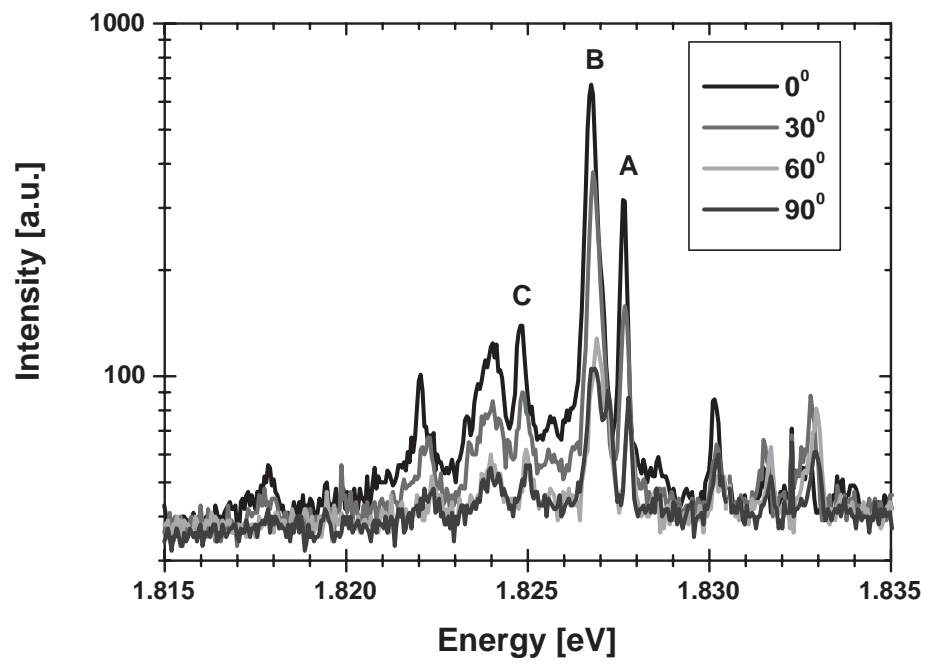


Figure 6.3: The spectral dependence on the observed linear polarization

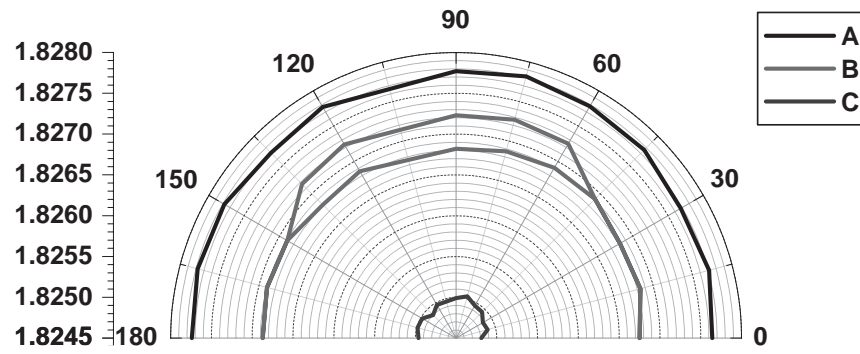


Figure 6.4: The spectral peak intensity dependence on the observed linear polarization

6.4 Conclusions

The anisotropic shape of the QD is probed by single QWR-like QD micro-PL. It is found that the asymmetric confinement potential is responsible for a lack of balance between van der Waals attractive forces and repulsion due to Pauli's exclusion principle in an exciton gas. Furthermore, it can be said that the degeneracy of the confinement directions are lifted, and its effects are apparent in the difference in the degree of the polarization of the PL.

It has been reported that, for similarly shaped CdSe/ZnS nanorods, the one-dimensional exciton ground state which changes from the optically forbidden ("dark") state to the optically active state as the size is reduced[6]. Thus, future work includes the determination of the degree of linear polarization of the PL, as well as the size dependence of the PL decay times.

Bibliography

- [1] Peyghambarian, N., Gibbs, H. M., Jewell, J. L., Antonetti, A., Migus, A., Hulin, D., Mysyrowicz, A., *Blue shift of the exciton resonance due to exciton-exciton interactions in a multiple-quantum-well structure*, Phys. Rev. Lett. **53**, 2433 (1984)
- [2] Vouilloz, F., Oberli, D. Y., Wiesendanger, S., Dwir, B., Reinhardt, F., *Density dependence of localized excitonic recombination in quantum wires*, Phys. Stat. Sol. (a) **164**, 259 (1997)
- [3] Schmitt-Rink, S., Chemla, D. S., Miller, D. A. B., *Theory of transient excitonic optical nonlinearities in semiconductor quantum-well structures*, Phys. Rev. B **32**, 6601 (1985)
- [4] Vouilloz, F., Oberli, D. Y., Lelarge, F., Dwir, B., Kapon, E., *Observation of many-body effects in the excitonic spectra of semiconductor quantum wires*, Solid State. Commun. **108**, 945 (1998)
- [5] Vouilloz, F., Wiesendanger, S., Oberli, D. Y., Dwir, B., Reinhardt, F., Kapon, E., *Direct observation of localized excitons in quantum wires by spatially resolved photoluminescence*, Physica E **2**, 862 (1998)
- [6] Le Thomas, N., Herz, E., Schöps, O., Woggon, U., Artemyev, M. V., *Exciton fine structure in single CdSe nanorods*, Phys. Rev. Lett. **94**, 016803 (2005)

Chapter 7

Conclusion

As QDs become important optical and electronic components in future devices, it is imperative that the studies of the energy levels of these QDs be made now, and such an investigation has been conducted in detail in this thesis. From a purely scientific standpoint, the multi-particle interactions within a single QD are also of great interest. These multi-particle interactions may also have applications in the engineering of novel devices using QDs.

The novel devices expected to appear in the near future will utilize single QD operations. A distribution in QD material composition, size, and shape will be, to some extent, inevitable; thus it is important to know what optoelectronic properties are to be expected from various single QDs with different material compositions, sizes, and shapes. Such studies were pursued in this thesis.

QDs made by droplet epitaxy have no dislocations, strain, nor wetting layer, and are considered to be the ideal QD embedded in a crystal matrix. In this thesis, QDs made by droplet epitaxy were studied.

In this thesis, the following crystal growth and optical studies have been performed.

Quantum dot growth and sample evaluation

Modified droplet epitaxy was used to grow low density GaAs/AlGaAs QD samples. Along with a relatively low density, a bimodal growth of small and large QDs was observed, thus reduced the “confining” QD density to nearly $3 \times 10^8 \text{cm}^{-2}$. From this sample, for the first time, broadband PL spectra of single GaAs/AlGaAs QDs made by modified droplet epitaxy have been observed and analyzed. InGaAs/GaAs QDs samples made by heterogeneous droplet epitaxy have also been the subject of study.

Resonant Raman spectroscopy of InGaAs QDs

InGaAs/GaAs QDs samples made by heterogeneous droplet epitaxy, which have well defined shapes, no wetting layer, and a barrier that is transparent to the QD PL line, were annealed at different temperatures and studied by resonant Raman spectroscopy. The TO, LO, and SO phonon-exciton interactions have been observed by resonant Raman spectroscopy. The appearance of TO lines indicate the existence of deformation potential interactions between the QD confined exciton and the TO phonon, while the appearance of LO and SO lines indicate the existence of Frölich interactions between the QD confined exciton and the LO and SO phonons.

As intermixing at the QD-barrier interface is increased with increasing annealing temperature, it was seen that both Frölich and deformation potential interactions are enhanced, judging from the intensities of these peaks in the resonant Raman spectra of samples with different annealing temperatures. The effect of annealing is more prominently seen in the Frölich interaction. Thus it can be said that interdiffusion enhances the exciton-LO phonon coupling in the QD. The observation of SO phonon-exciton interactions suggest that the annealed QDs are not perfect spheres; this coupling between the charge distribution and the surface modes is observed due to the lower symmetry of the shape of the QD, and give rise to issues such as the non-adiabaticity of the exciton-phonon systems. These issues require further investigations.

Pressure dependence of GaAs QD PL

PL from high density GaAs/AlGaAs QD samples made by modified droplet epitaxy were studied under high hydrostatic pressure to determine the band offset and, consequently, the QD/barrier band lineups. The results were used in effective mass approximation calculations using the cylindrical symmetry of the QD, to determine the ground-to-excited state transition energy separation (E1), as well as the ground-to-excited hole state transition energy separation (E2) of the QD. The effects of interdiffusion on the QD potential were introduced into these calculations; this validates the cylindrical symmetry of the originally pyramidal QD shape. The ground state and first-excited state hole energy levels were resolved from the QD PL spectra taken at high pressures, and from the value of the spacing of these energy levels, E2 was determined, thus giving an estimate of the E1 value from the effective mass approximation calculations.

Single GaAs QD micro-PL spectroscopy

The broadband spectra of a single GaAs/AlGaAs QD made by MDE was observed for the first time, and the sharp spectral lines from a single QD spectra were resolved. Furthermore, from the excitation intensity dependence of the broadband spectra of a single QD, the various spectral lines in the single QD spectra were assigned to the energy levels and multi-carrier correlations within the QD. These results were compared to theoretical calculations, and good agreement between data and theory was seen.

An interesting point in these single QD spectra was that a normally dipole forbidden recombination emission was observed, due to many-body Coulomb interactions in the QD.

From the fine structure near the ground state energy level, multi-carrier energy renormalizations of the ground state energy level are observed. Coulomb interactions do not make themselves apparent in the renormalized spectra, but the e-e, h-h, and e-h interaction correlations can be determined from the renormalized spectra. The e-e and h-h interaction correlations were found to decrease with decreasing QD size, which can be understood as the same carrier wavefunctions having lesser spatial overlap as the same spin electron/holes tend to push each other away in smaller QDs. On the other hand, it was found that the e-h interaction correlations were found to increase with decreasing QD size, which can be understood as the electron-hole wavefunction spatial overlap increasing in smaller QDs. This observation was possible due to the fact that the electron and hole envelope wavefunctions keep the symmetry of the crystal due to the lack of strain in the QD, and were easily analyzed because there are no wetting layer-confined carriers, making the carrier interactions picture much simpler. Thus, GaAs/AlGaAs QDs made by MDE are, in this sense, ideal QDs.

Quantum wire(QWR)-like GaAs QDs

Using the same micro-PL setup as used in chapter 5, highly anisotropically shaped QD was studied, and their many-carrier correlations were studied. The anisotropic shape of the QD was probed by single QWR-like QD micro-PL. It was found that the asymmetric confinement potential is responsible for a lack of balance between van der Waals attractive forces and repulsion due to Pauli's exclusion principle. Furthermore, it can be said that the degeneracy of the confinement directions were lifted, and its effects were apparent in the difference in the degree of the polarization of the PL.

Curriculum Vitae

Education

- 2002-2005 Tokyo Institute of Technology, Tokyo, Japan
Doctor of Philosophy (Physics)
- 2000-2002 Tokyo Institute of Technology, Tokyo, Japan
Masters of Engineering (Electronic Engineering)
- 1996-2000 Keio University, Tokyo, Japan
Bachelor of Science (Physics)
- 1995- Columbia University, New York, New York
currently on indefinite leave to pursue studies in Japan

Other

- 2003-2005 Research Assistant,
The 21st Century Center of Excellence, Department of Physics,
Tokyo Institute of Technology, Nanometer Scale Quantum Physics

Publication List

Yamagiwa, M., Sumita, N., Minami, F., Koguchi, N., *Confined electronic structure in GaAs quantum dots*, J. Lumin. **108**, 379 (2004)

Yamagiwa, M., Ikeda, K., Minami, F., Koguchi, N., *Electronic and multi-electronic structures in GaAs quantum dots*, to be published in Microelectronics Journal

Yamagiwa, M., Minami, F., Koguchi, N., *Electronic and Multi-Electronic Structures in GaAs Quantum Dots*, to be published in the Proceedings of the 27th International Conference on the Physics of Semiconductors